Simulations of Droplet Interactions with Lattice Boltzmann Methods

by

Orest Shardt

A thesis submitted in partial fulfillment of the requirements for the degree of

Doctor of Philosophy

in

Chemical Engineering

Department of Chemical and Materials Engineering
University of Alberta

Abstract

Interactions between droplets were studied using two lattice Boltzmann methods (LBMs). The Shan-Chen LBM, in which repulsive forces between fluids maintain phase separation, was used to simulate systems with three immiscible components. The simulations demonstrated the three equilibrium configurations of two droplets in a third fluid: adhering, separated, and engulfed. Simulations of adhering droplet pairs, called Janus droplets due to their two-sided structure, in shear flow revealed the structure of the internal flow and the dependence of the rotation rate on the orientation of the droplet. A second type of interaction between droplets was simulated with the free-energy binary-liquid LBM: binary droplet collisions in confined simple shear flow. The conditions for coalescence were quantified and the effects of geometry and the parameters of this Cahn-Hilliard-type phase field model on the critical conditions were examined. Two parameters of the phase field model, the thickness of the diffuse interface and the mobility of the phase field, are important. Simulations with highly-resolved droplets, with radii spanning 200 lattice nodes, were used to determine the minimum film thickness before coalescence, its relationship to the interface thickness, and the effect of the mobility on the evolution of the minimum distance between the droplet interfaces during collisions. The critical conditions for coalescence in these simulations were compared with published experiments with polymers. Unlike the experimental polymer system, the interfaces of interacting droplets are often charged, as in the case of oil-water emulsions. To simulate such liquid systems, the free-energy binary-liquid LBM was coupled with an iterative finite difference solver for the linearized Poisson-Boltzmann equation that describes the electrostatic potential near a charged surface in an electrolyte solution. Simulations of collisions between charged droplets with constant zeta potentials

in a sheared electrolyte showed the effects of surface charge on the critical conditions for coalescence.

Preface

Chapter 2 of this thesis has been published as Orest Shardt, J.J. Derksen, Sushanta K. Mitra, "Simulations of Janus droplets at equilibrium and in shear," *Physics of Fluids*, 26:012104 (2014). Chapter 3 of this thesis has been published as Orest Shardt, J.J. Derksen, Sushanta K. Mitra, "Simulations of droplet coalescence in simple shear flow," *Langmuir*, 29:6201–6212 (2013). For both papers, I wrote the simulation software, analyzed the results, and wrote the manuscripts. J.J. Derksen and Sushanta K. Mitra were supervisory authors, involved in the interpretation of the results and composition of the manuscripts. Chapters 4 and 5 will be submitted to journals for consideration for publication. The authors and their contributions to these chapters are the same as for the published chapters.

To my family

Acknowledgments

I would like to thank my supervisor Dr. Jos Derksen for insightful discussions about simulations and the physics of many flow phenomena, and I thank my co-supervisor Dr. Sushanta K. Mitra for introducing me to the field of microfluidics. I am very grateful for both of their guidance, enthusiasm, and support of my research and academic and professional development.

I would like to thank all the undergraduate students, graduate students, and postdoctoral fellows with whom I had the pleasure of collaborating on many endeavours, both academic and extracurricular, during my doctoral studies.

Contents

List of Figures

List of Tables

List of Symbols

A, B, κ_φ Parameters in free energy functional

A_1, A_2 Cross-sectional areas of droplets 1 and 2 in Janus droplet

A_i, B_i, C_i, D_i, G_i Parameters in equilibrium distribution f_i^{eq}

α Proportionality factor in scaling law

A_{mn}, a_n, α_n, β_m, γ_n, λ_{mn} Factors in series solution

$\vec{b}$ Body force

Ca   Capillary number

Ca_c Critical capillary number

$\vec{c}_i$ Lattice velocity

d Separation distance

ΔP Pressure difference

ΔP_φ, ΔP_ψ Phase field and electric contributions to pressure difference

Δx Lattice spacing

ΔX, ΔY Initial distances in x and y directions between droplet centres of mass

e Elementary charge

E_{L2} L2 norm of error

ε Dielectric permittivity

η_i Number density of component i

$\eta_{i\infty}$ Number density of component i in bulk

η_∞ Number density in bulk

$\vec{E}$ Electric field

E_x External electric field component in x direction

f_i, g_i Density distributions in lattice Boltzmann method

f_i^{eq}, g_i^{eq} Equilibrium density distributions in lattice Boltzmann method

f_n Function in series solution

f_p Force on charged flat plates

$F[\varphi]$ Free energy functional

Γ Parameter in lattice Boltzmann method for phase field

$\dot{\gamma}$ Shear rate

g_{ij} Interaction strength between fluids i and j in Shan-Chen LBM

h Film thickness (minimum distance between droplet interfaces)

h_c Critical film thickness

h_J Distance between drops in Janus droplet

$h_{\min}$ Minimum film thickness

i, j, k Node indices in each coordinate direction

κ Inverse Debye length

k_B Boltzmann constant

L, W, H Domain length, width, and height

l_c Characteristic length

ℓ_φ Characteristic length of phase field interface thickness

M Phase field mobility

μ Fluid dynamic viscosity

μ_φ Chemical potential

n Scaling law exponent

n, m Term indices in series

$\hat{n}$ Outward unit normal on droplet interface

ν Fluid kinematic viscosity

N_x, N_y, N_z Number of grid/lattice nodes in each coordinate direction

Ω Vorticity

ω Rotation rate

$\bar{\omega}$ Average rotation rate

P Pressure

P_0, P_1, P_2 Pressures inside and outside a Janus droplet

P_{ref} Reference pressure

Pe   Péclet number

$\hat{\text{Pe}}$ Modified Péclet number

ϕ Janus droplet orientation angle

φ Phase field order parameter

φ_0 Bulk value of phase field

ψ Electrostatic potential

ψ_{ref} Reference potential

q_{s} Surface charge density

R Droplet radius

r Radial distance from centre of droplet

R_1, R_2 Radii of droplets 1 and 2 in Janus droplet geometry

R_b Bridge radius

R_c Radius of curvature of internal interface in Janus droplet

Re   Reynolds number

Re_b Bridge growth Reynolds number

ρ Fluid density

ρ_e Free charge density

ρ_k Density of fluid k

σ Interfacial tension

σ_{ij} Interfacial tension between fluids i and j

Su   Suratman number

T Temperature

t Time

τ Period of rotation

τ_f, τ_g Relaxation rates in lattice Boltzmann method

τ_i Inertial time scale

τ_s Shear time scale

θ_1, θ_2, θ_c Angles in Janus droplet geometry

θ_f Film orientation angle

$\tilde{t}$ Normalized time

u_0 Shear speed

$\tilde{u}$ Normalized speed

$\tilde{u}_{e0}$ Normalized electroosmotic steady flow speed

$\vec{u}$ Flow velocity

$\vec{u}_{rot}$ Velocity due to rigid rotation

V_1, V_2 Volumes of droplets 1 and 2 in Janus droplet

$\bar{x}$, $\bar{y}$ Position of droplet centre of mass

ξ Dimensionality constant in Young-Laplace law

x_i, y_j, z_k Position of node with indices i, j, k

$\vec{x}$ Position vector

ζ Interface (zeta) potential

z_i Ion valence

Introduction

1.1 Motivation

In flows of droplet dispersions, the droplets are distorted by the flow and collide with other droplets. With sufficient distortion, the droplets break apart, and some collisions lead to coalescence. A common natural example of interacting droplets is rain, in which coalescence and breakup contribute to the distribution of droplet sizes[1–4]. The collective behaviour of large numbers of droplets in flow is also relevant to many industrial applications. Interactions between droplets during turbulent agitation of liquid-liquid mixtures[5–9] and pipe flows[10–12] determine the drop size distribution (DSD). The DSDs produced in such flows depend on the intensity of the turbulence, the physical properties of the fluids, and the nature of any surface active agents (surfactants) that are present[13–16]. DSDs and their changes due to flow are significant to industrial applications because they affect, for example, the quality of food products[17], the rates of mass transfer between the fluids[18, 19], and the effective viscosity of the dispersion[20].

Relatively recent progress in the fabrication of devices with microscale functional components has provided motivation and methods for studying the fundamental physical and chemical phenomena that determine the behaviour of droplets[21]. In such microfluidic devices, droplets can be created[22] and used as reactors[23]. Controlling the coalescence of adjacent droplets in a chain flowing through a microchannel is a common topic, and various techniques have been developed to promote and suppress coalescence[24]. For example, a pair of droplets coalesces while separating as one droplet enters a narrower channel[25]. To prevent coalescence of adjacent droplets, drops of a third fluid that is immiscible with the other two have been inserted between them[26]. The precise control of flow and droplets that is possible in microfluidics has allowed the production of emulsions with controlled DSDs, such as highly monodisperse emulsions[27, 28]. Complex multiple emulsions[29–31], which are emulsions with several droplets encapulated inside another droplet, have also been created. Another type of complex emulsion is a Janus emulsion[31–33] that consists

of droplets with two adhering lobes of different fluids.

Simulations supplement experimental investigations of droplets in several valuable ways. One advantage of simulations is that they can provide information about an evolving system that is impossible to obtain from experiments, especially without disturbing the quantities that are being measured. For example, accurate measurements of droplet sizes in a stirred vessel are difficult[34]. In comparison, information about the size of every simulated drop in a flow is in principle available for every time increment of the simulation (though the time needed to store and process this data limits how much of it can be used). Details about droplet flows, such as the thicknesses of the films between drops are even more difficult to measure but would be available from a sufficiently well-resolved simulation that models the relevant physical phenomena of interacting interfaces. Simulations also allow precise control over initial conditions in ways that are experimentally impossible. As an example, simulations of droplet flows starting from various initial DSDs could be used to study the rates of coalescence and breakage as they evolve to a steady DSD. This information could contribute to population balance models that describe the evolution of DSDs as a function of flow conditions[35–37]. Finally, simulations, unlike experiments, allow different physical phenomena to be turned on and off at will to assess their relative importance in determining observed outcomes. Simulations are therefore appealing for studying interactions between droplets, however to simulate coalescence they must model and resolve phenomena at length scales much smaller than the droplets, i.e. the length scale of the films between droplets. Consequently such simulations require significant computing power and appropriate computational frameworks.

Computing hardware has advanced at a rapid pace in recent years, resulting in systems that can perform more calculations every second and have faster access to larger amounts of memory. An example of such an advance is the use of graphics processing units (GPUs) for scientific computing. Originally designed to render images of digital scenes at high frame rates for computer games, GPUs have hundreds to thousands of arithmetic units instead of the 1 to 16 found on current central processing units (CPUs). The effective use of systems with multiple computing cores that can operate simultaneously depends on the implementation of algorithms that access memory efficiently and minimize the need to share data between cores. Consequently, numerical methods that can compute the flow in a portion of the whole simulation domain with minimal information from adjacent portions are ideal for GPUs (and also clusters of interconnected CPUs). While their high performance could be used to simulate larger systems with more droplets at resolutions that are typical of existing studies (with radii on the order of 10 nodes[38, 39]), GPUs are applied in this thesis to highly-resolved simulations of the interactions between interfaces.

1.2 Simulation methods for multiphase flow

The different methods for simulating multiphase flows are briefly introduced here. The main chapters of the thesis provide greater detail about the advantages and disadvantages of the methods that are relevant to the systems simulated in each chapter.

Conventional computational fluid dynamics (CFD) methods in general convert the partial differential governing equations for flow into a set of algebraic equations that are then solved numerically. Three methods are popular: the finite difference, finite volume, and finite element methods[40]. In the finite difference method, finite differences replace derivatives in the governing equations. Fluxes across the faces of a discretizing mesh are computed in the finite volume method, which ensures that transported quantities are conserved. An optimization approach is used in finite element methods to determine a solution that minimizes the residual between an interpolating function (often a polynomial) and the governing equation in every element of the domain[41]. The Navier-Stokes governing equations do not include an evolution equation for the pressure, and instead a Poisson-type equation is solved. This step is computationally expensive, accounting for up to 60% of the time needed for each step of a simulation[42].

Multiphase flow simulations combine one of the previously mentioned solvers for the Navier-Stokes equations with a method for tracking the locations of regions with different fluid properties. They also impose interfacial tension on the boundaries between fluids. Several methods are used to describe the motion and deformation of the fluid regions. The volume-of-fluid method advects a scalar that specifies the volume fraction of one phase throughout the domain[43], and the level set method advects a scalar that is initialized to be the distance to the nearest interface[44]. In these methods, interfaces connect when the thickness of the film between them cannot be resolved by the discretizing mesh. Another approach uses a scalar that specifies the composition of the fluid and models the thermodynamics of phase separation. These are called phase-field methods, an example of which is the Cahn-Hilliard approach[45, 46]. Instead of tracking a scalar that specifies the locations of different fluid domains, other methods use moving meshes located at the interfaces between fluid domains. Examples are boundary integral[47], arbitrary Lagrangian-Eulerian (ALE)[48], and front-tracking[49] methods. In these mesh-based methods, the computational expenses of evolving the mesh and maintaining its quality can be significant. Topological changes occur when the width of a thread or the thickness of a film falls below a user-specified threshold.

1.2.1 Lattice Boltzmann methods

Lattice Boltzmann methods (LBMs)[50, 51] do not directly discretize the governing equations for flow and instead imitate the behaviour of gas molecules. While gas molecules may move freely in any direction and their velocities satisfy the Maxwell-Boltzmann distribution, the fictitious molecules in LBMs may only move between the nodes of a lattice along a finite set of directions that connect the nodes. LBMs track the amount of molecules moving in each direction and thus compute the evolution of the velocity distribution at each node of the lattice. Collisions between molecules are handled through a relaxation process that brings the velocity distribution at each node towards a discrete version of the Maxwell-Boltzmann distribution. Many variations of the collision process are available, and the BGK method (Bhatnagar et al. [52]) remains popular. As the kinetics of gas molecules may be linked to the Navier-Stokes equations at a macroscopic level, the particle densities that propagate along a lattice can be shown to also satisfy the macroscopic flow equations, making LBMs suitable for CFD. The rate of relaxation towards the equilibrium distribution determines the viscosity of the fluid. LBMs are typically implemented in a two-step process. In one step, densities propagate to adjacent nodes along the lattice directions; in the next step, the velocity distribution at each node relaxes towards the equilibrium distribution. This process is highly amenable to parallelization, a key advantage over other CFD methods, because no communication is required during the collision step, and communication with only the adjacent nodes is required for the propagation step.

Several LBMs that are suitable for simulating mixtures of liquids have been proposed in the academic literature. The multicomponent Shan-Chen method[53, 54] consists of a coupled set of single-phase LBMs, one for each component in the flow. The separation of components and interfacial tensions between them are implemented through a repulsive interaction potential that acts between each pair of fluids. This method is used in Chapter 2 to simulate Janus droplets. Though advantageous for its simplicity and ability to simulate an arbitrary number of components, this method was found to be unsuitable for studies of droplet collisions and the conditions for coalescence. In a system with two fluids, only one parameter specifies the strength of the repulsive interaction between them. As this parameter is decreased to simulate lower interfacial tensions, the transition in composition across the interfaces between fluids spreads over a longer distance, called the interface thickness. When droplets collide, they coalescence unless shear forces exceed interfacial tension forces sufficiently (i.e. the capillary number, the ratio of viscous and interfacial forces, exceeds a critical value). In early exploratory simulations with the Shan-Chen LBM, interfaces became excessively thick as the interfacial tension was lowered to find non-

coalescing conditions.

The free-energy LBM[55, 56] is used to study binary droplet collisions. This method, which is effectively a Cahn-Hilliard phase field method, has a scalar that specifies the composition of the fluid. Both the fluid flow and evolution of the scalar are solved with LBMs. This scalar advects with the flow and also diffuses towards minimization of a free-energy functional. The functional has two terms: a double-well potential that causes separation into two phases and an energy penalty against composition gradients that endows interfaces with tension. Two parameters of the model together specify the thickness of the interface and its interfacial tension, which can therefore be specified independently, an important advantage over the Shan-Chen LBM. This method has been used to simulate, for example, droplet deformation and breakup[57, 58], droplet spreading on patterned substrates[59], and droplet formation in a microfluidic T-junction[60]. In addition to its practical advantages, this method is preferred for its thermodynamic description of interfaces. For example, the presence of a disjoining pressure in thin films[61] suggests suitability for studying coalescence. In physical systems, van der Waals forces across liquid films lead to the rupture of the film between two droplets and coalescence.

A third LBM, the colour model LBM [62, 63], has also been used to simulate mixtures of liquids. In this method, each component, or fluid colour, has its own particle distribution as in the Shan-Chen LBM. An additional collision step is applied to the nodes at the interface between the fluids. This collision step redistributes the fluid densities among the discrete directions so that they move towards regions with the same composition[50]. Due to the non-thermodynamic treatment of interfacial interactions, this method is not used in this thesis. Colour model simulations of droplet collisions and systems with three or more components are possible areas for future study.

1.3 Thesis objectives

This thesis presents studies of interactions between droplet interfaces through simulations with the Shan-Chen and free-energy LBMs. The thesis focuses on two types of interactions: adhesion in three-component systems and coalescence in two-component systems first without then with interfacial charge. The goals of the studies are to assess the ability of the simulation methods to reproduce the expected physical behaviour of the systems (based on past theory and experiments) and to use the simulations to provide insight about the physical systems they model. As a whole, the work described in this thesis advances knowledge about and progresses towards realistic simulations of interfacial interactions in multiphase flow.

1.4 Thesis outline

Chapter 2 presents a study of the equilibrium configurations of two adjacent droplets in a three-fluid mixture. The simulations in this chapter are performed using the multicomponent Shan-Chen LBM, and this chapter evaluates the ability of this LBM to model a system with three components and the interfacial tensions between them. The simulations show that the three possible configurations of two droplets are achieved and have the expected geometry as determined by the interfacial tensions. Simulations of a compound droplet with two adhering parts, a Janus droplet, in shear are then described. The internal interface of a Janus droplet disrupts the internal circulation patterns, making them differ from those in a usual single-phase droplet. These differences provide insight into the rheology of Janus droplet emulsions.

The outcomes of collisions between droplets of the same fluid in shear are studied in Chapter 3. Since the Shan-Chen LBM was found to be unsuitable to study the critical conditions for coalescence, this chapter and the subsequent chapters use the free-energy binary-liquid LBM. The parameters of this phase-field model, the flow conditions, and the geometry are systematically varied to determine the critical conditions for coalescence and their dependence on these variables. This chapter identifies the key role of the ratio of the droplet radius and interface thickness on the conditions for coalescence. The high capillary numbers at which droplet coalescence is observed indicate that the simulated droplets are smaller than those in typical experiments. Though the droplets and the film between them are sufficiently resolved that critical conditions can be found, the resolution is insufficient to draw precise conclusions about the effective physical size of the simulated droplets.

This study of the conditions for coalescence of droplets is then extended in two different directions, both of which require additional computational power. Chapter 4 reports simulations with twice the maximum resolution considered in Chapter 3. With this resolution, critical capillary numbers may now be found at a sufficiently small initial separation between the droplets that a comparison with published experiments is meaningful. The evolution of the minimum distance between the droplet interfaces during collisions is computed, the dynamics of the thinning rate are examined, and a critical minimum thickness for cases without coalescence is determined. The effective physical size of the droplets is then estimated, and the effects of the phase field mobility on the conditions for coalescence are considered.

Chapter 5 reports simulations of collisions between charged droplets in electrolyte, which is the second extension of the work in Chapter 3. The flow solver from Chapter 3 was coupled with an iterative finite difference solver for the linearized Poisson-Boltzmann

equation governing electrostatic potential in an electrolyte near a charged surface. Attention is restricted to the case of droplets with fixed surface (zeta) potentials. The simulations are used to study the strength of electrostatic interactions that is needed to affect the critical capillary numbers for coalescence that were determined in Chapter 3.

The last chapter, Chapter 6, summarizes the results of the preceding chapters and offers perspectives on their implications and areas for future investigation.

References

[1] J.S. Marshall and W.McK. Palmer. The distribution of raindrops with size. *J. Meteor.*, 5:165–166, 1948.

[2] R.C. Srivastava. Size distribution of raindrops generated by their breakup and coalescence. *J. Atmos. Sci.*, 28:410–415, 1971.

[3] T.B. Low and R. List. Collision, coalescence and breakup of raindrops. Part I. Experimentally established coalescence efficiencies and fragment size distributions in breakup. *J. Atmos. Sci.*, 39:1591–1606, 1982.

[4] Z. Hu and R.C. Srivastava. Evolution of raindrop size distribution by coalescence, breakup, and evaporation: Theory and observations. *J. Atmos. Sci.*, 52:1761–1783, 1995.

[5] J.Y. Park and L.M. Blair. The effect of coalescence on drop size distribution in an agitated liquid-liquid dispersion. *Chem. Eng. Sci.*, 30:1057–1064, 1975.

[6] F.B. Sprow. Drop size distributions in strongly coalescing agitated liquid-liquid systems. *AIChE J.*, 13:995–998, 1967.

[7] C.A. Coulaloglou and L.L. Tavlarides. Drop size distributions and coalescence frequencies of liquid-liquid dispersions in flow vessels. *AIChE J.*, 22:289–297, 1976.

[8] M.A. Delichatsios and R.F. Probstein. The effect of coalescence on the average drop size in liquid-liquid dispersions. *Ind. Eng. Chem. Fundamen.*, 15:134–138, 1976.

[9] G. Zhou and S.M. Kresta. Evolution of drop size distribution in liquid–liquid dispersions for various impellers. *Chem. Eng. Sci.*, 53:2099–2113, 1998.

[10] S.B. Collins and J.G. Knudsen. Drop-size distributions produced by turbulent pipe flow of immiscible liquids. *AIChE J.*, 16:1072–1080, 1970.

[11] S. Middleman. Drop size distributions produced by turbulent pipe flow of immiscible fluids through a static mixer. *Ind. Eng. Chem. Process Des. Dev.*, 13:78–83, 1974.

[12] M.J.H. Simmons and B.J. Azzopardi. Drop size distributions in dispersed liquid–liquid pipe flow. *Int. J. Multiphase Flow*, 27:843–859, 2001.

[13] M. Kraume, A. Gäbler, and K. Schulze. Influence of physical properties on drop size distribution of stirred liquid-liquid dispersions. *Chem. Eng. Tech.*, 27:330–334, 2004.

[14] S. Tcholakova, N.D. Denkov, and T. Danner. Role of surfactant type and concentration for the mean drop size during emulsification in turbulent flow. *Langmuir*, 20:7444–7458, 2004.

[15] J.L. Salager, M. Perez-Sanchez, and Y. Garcia. Physicochemical parameters influencing the emulsion drop size. *Colloid Polym. Sci.*, 274:81–84, 1996.

[16] U. Sundararaj and C.W. Macosko. Drop breakup and coalescence in polymer blends: The effects of concentration and compatibilization. *Macromolecules*, 28:2647–2657, 1995.

[17] D.J. McClements. *Food emulsions: principles, practices and techniques*. CRC Press, 2nd edition, 2005.

[18] J.J.C. Cruz-Pinto and W.J. Korchinsky. Experimental confirmation of the influence of drop size distribution on liquid-liquid extraction column performance. *Chem. Eng. Sci.*, 35:2213–2219, 1980.

[19] M. Chakraborty, C. Bhattacharya, and S. Datta. Effect of drop size distribution on mass transfer analysis of the extraction of nickel(II) by emulsion liquid membrane. *Colloid Surface A*, 224:65–74, 2003.

[20] Y. Otsubo and R.K. Prud'homme. Effect of drop size distribution on the flow behaviour of oil-in-water emulsions. *Rheol. Acta*, 33:303–306, 1994.

[21] N. Bremond and J. Bibette. Exploring emulsion science with microfluidics. *Soft Matter*, 8:10549–10559, 2012.

[22] S.L. Anna, N. Bontoux, and H.A. Stone. Formation of dispersions using "flow focusing" in microchannels. *Appl. Phys. Lett.*, 82:364–366, 2003.

[23] S.-Y. Teh, R. Lin, L.-H. Hung, and A.P. Lee. Droplet microfluidics. *Lab Chip*, 8: 198–220, 2008.

[24] Y.-C. Tan, Y.L. Ho, and A.P. Lee. Droplet coalescence by geometrically mediated flow in microfluidic channels. *Microfluid. Nanofluid.*, 3:495–499, 2007.

[25] N. Bremond, A.R. Thiam, and J. Bibette. Decompressing emulsion droplets favors coalescence. *Phys. Rev. Lett.*, 100:024501, 2008.

[26] D. L. Chen, L. Li, S. Reyes, D.N. Adamson, and R.F. Ismagilov. Using three-phase flow of immiscible liquids to prevent coalescence of droplets in microfluidic channels: Criteria to identify the third liquid and validation with protein crystallization. *Langmuir*, 23:2255–2260, 2007.

[27] P.B. Umbanhowar, V. Prasad, and D.A. Weitz. Monodisperse emulsion generation via drop break off in a coflowing stream. *Langmuir*, 16:347–351, 2000.

[28] J.H. Xu, S.W. Li, J. Tan, Y.J. Wang, and G.S. Luo. Preparation of highly monodisperse droplet in a T-junction microfluidic device. *AIChE J.*, 52:3005–3010, 2006.

[29] A.S. Utada, E. Lorenceau, D.R. Link, P.D. Kaplan, H.A. Stone, and D.A. Weitz. Monodisperse double emulsions generated from a microcapillary device. *Science*, 308:537–541, 2005.

[30] L.-Y. Chu, A.S. Utada, R.K. Shah, J.-W. Kim, and D.A. Weitz. Controllable monodisperse multiple emulsions. *Angew. Chem. Int. Ed.*, 46:8970–8974, 2007.

[31] C.-H. Choi, D.A. Weitz, and C.-S. Lee. One step formation of controllable complex emulsions: From functional particles to simultaneous encapsulation of hydrophilic and hydrophobic agents into desired position. *Adv. Mater.*, 25:2536–2541, 2013.

[32] H. Hasinovic, S. E. Friberg, and Guo Rong. A one-step process to a Janus emulsion. *J. Colloid Interf. Sci.*, 354:424–426, 2011.

[33] H. Hasinovic and S. E. Friberg. One-step inversion process to a Janus emulsion with two mutually insoluble oils. *Langmuir*, 27:6584–6588, 2011.

[34] S. Maaß, S. Wollny, A. Voigt, and M. Kraume. Experimental comparison of measurement techniques for drop size distributions in liquid/liquid dispersions. *Exp. Fluids*, 50:259–269, 2011.

[35] C. Tsouris and L.L. Tavlarides. Breakage and coalescence models for drops in turbulent dispersions. *AIChE J.*, 40:395–406, 1994.

[36] D. Sathyagal, A.N. Ramkrishna and G. Narsimhan. Droplet breakage in stirred dispersions. breakage functions from experimental drop-size distributions. *Chem. Eng. Sci.*, 51:1377–1391, 1996.

[37] Z. Chen, J. Prüss, and H.-J. Warnecke. A population balance model for disperse systems: Drop size distribution in emulsion. *Chem. Eng. Sci.*, 53:1059–1066, 1998.

[38] X. Jia, J. B. McLaughlin, and K. Kontomaris. Lattice Boltzmann simulations of flows with fluid-fluid interfaces. *Asia-Pac. J. Chem. Eng.*, 3:124–143, 2008.

[39] P. Perlekar, L. Biferale, M. Sbragaglia, S. Srivastava, and F. Toschi. Droplet size distribution in homogeneous isotropic turbulence. *Phys. Fluids*, 24:065101, 2012.

[40] Pradip Niyogi, S.K. Chakrabartty, and M.K. Laha. *Introduction to Computational Fluid Dynamics*. Dorling Kindersley, 2006.

[41] Darrell W. Pepper and Juan C. Heinrich. *The Finite Element Method*. Taylor and Francis, 2nd edition, 2006.

[42] B.P. Van Poppel, O. Desjardins, and J.W. Daily. A ghost fluid, level set methodology for simulating multiphase electrohydrodynamic flows with application to liquid fuel injection. *J. Comput. Phys.*, 229(20):7977–7996, 2010.

[43] D. Gerlach, G. Tomar, G. Biswas, and F. Durst. Comparison of volume-of-fluid methods for surface tension-dominant two-phase flows. *Int. J. Heat and Mass Transfer*, 49:740–754, 2006.

[44] J.A. Sethian and P. Smereka. Level set methods for fluid interfaces. *Annu. Rev. Fluid Mech.*, 35:341–372, 2003.

[45] J.W. Cahn and J.E. Hilliard. Free energy of a nonuniform system. I. Interfacial free energy. *J. Chem. Phys.*, 28:258–267, 1958.

[46] D. Jacqmin. Calculation of two-phase Navier-Stokes flows using phase-field modeling. *J. Comput. Phys.*, 155(1):96–127, 1999.

[47] R.H. Davis and A.Z. Zinchenko. Motion of deformable drops through granular media and other confined geometries. *J. Colloid Interf. Sci.*, 334:113–123, 2009.

[48] J. Donea, A. Huerta, J.-Ph. Ponthot, and A. Rodríguez-Ferran. Arbitrary Lagrangian-Eulerian methods. In Erwin Stein, René de Borst, and Thomas J.R. Hughes, editors, *Encyclopedia of Computational Mechanics Volume 1: Fundamentals*, chapter 14, pages 223–233. Wiley, 2004.

[49] S.O. Unverdi and G. Tryggvason. A front-tracking method for viscous, incompressible, multi-fluid flows. *J. Comput. Phys.*, 100(1):25–37, 1992.

[50] S. Chen and G.D. Doolen. Lattice Boltzmann method for fluid flows. *Annu. Rev. Fluid Mech.*, 30:329–364, 1998.

[51] C.K. Aidun and J.R. Clausen. Lattice-Boltzmann method for complex flows. *Annu. Rev. Fluid Mech.*, 42:439–472, 2010.

[52] P.L. Bhatnagar, E.P. Gross, and M. Krook. A model for collision processes in gases. I: Small amplitude processes in charged and neutral one-component system. *Phys. Rev.*, 94:511–525, 1954.

[53] X. Shan and H. Chen. Lattice Boltzmann model for simulating flows with multiple phases and components. *Physical Review E*, 47(3):1815–1820, 1993.

[54] X. Shan and G. Doolen. Multicomponent lattice-Boltzmann model with interparticle interaction. *J. Stat. Phys.*, 81:379–393, 1995.

[55] M.R. Swift, S.E. Orlandini, W.R. Osborn, and J.M. Yeomans. Lattice Boltzmann simulations of liquid-gas and binary fluid systems. *Phys. Rev. E*, 54:5041–5052, 1996.

[56] A.J. Briant and J.M. Yeomans. Lattice Boltzmann simulations of contact line motion. II. Binary fluids. *Phys. Rev. E*, 69:031603, 2004.

[57] R.G.M. van der Sman and S. van der Graaf. Emulsion droplet deformation and breakup with lattice Boltzmann model. *Comput. Phys. Commun.*, 178:492–504, 2008.

[58] A.E. Komrakova, O. Shardt, D. Eskin, and J.J. Derksen. Lattice Boltzmann simulations of drop deformation and breakup in shear flow. *Int. J. Multiphase Flow*, 59: 24–43, 2014.

[59] H. Kusumaatmaja, J. Léopoldès, A. Dupuis, and J.M. Yeomans. Drop dynamics on chemically patterned surfaces. *Europhys. Lett.*, 73(5):740–746, 2006.

[60] S. van der Graaf, T. Nisisako, C.G.P.H. Schroën, R.G.M. van der Sman, and R.M. Boom. Lattice Boltzmann simulations of droplet formation in a T-shaped microchannel. *Langmuir*, 22:4144–4152, 2006.

[61] P. Yue, J.J. Feng, C. Liu, and J. Shen. Diffuse-interface simulations of drop coalescence and retraction in viscoelastic fluids. *J. Non-Newtonian Fluid Mech.*, 129: 163–176, 2005.

[62] A. Gunstensen, D. Rothman, S. Zaleski, and G. Zanetti. Lattice Boltzmann model of immiscible fluids. *Phys. Rev. A*, 43:4320–4327, 1991.

[63] M. Latva-Kokko and D.H. Rothman. Diffusion properties of gradient-based lattice Boltzmann models of immiscible fluids. *Phys. Rev. E*, 71:056702, 2005.

Simulations of Janus droplets at equilibrium and in shear[1]

2.1 Introduction

Simulation methods are available for studying the various industrial processes that involve flows of three fluids. While many applications involve a gas phase and two liquid phases, such as oil recovery from porous media (simulations of two-phase imbibition were described by Gunde et al. [1]) and bubbly flows relevant to nuclear safety[2], dispersions of two immiscible liquids in a third liquid have been studied only recently. These new examples of three-component systems motivate a detailed analysis of their behaviour and the evaluation of simulation methods specifically for their unique characteristics. Under certain conditions, droplets of the two dispersed liquids may adhere to form a compound droplet called a Janus droplet after the two-faced character in Roman mythology[3, 4].

Several interesting phenomena involving Janus droplets have been recently discussed in the literature. Hasinovic et al. described a method for generating bulk quantities of an emulsion with Janus droplets, called a Janus emulsion [5, 6]. Adhering, engulfed, and distinct droplets have been produced in microfluidic devices [7, 8]. Droplet adhesion was also considered by Chen et al. [9], who used a third immiscible liquid to separate droplets for microfluidic protein crystallization. Finally, Guzowski et al. [10] recently produced long Janus droplet chains in a microfluidic device. These chains are long sequences of adhering fluid drops of alternating compositions. Such chains can coil up without coalescing and could create a fluid with interesting rheology[10]. Considering the range of possible geometries for a Janus droplet, emulsions of Janus droplets and chains likely have complex rheologies that depend on the interfacial tensions between the liquids. Simulations provide a way to investigate the behaviour of Janus emulsions, starting with simulations of one

---

[1]A version of this chapter has been published as Orest Shardt, J.J. Derksen, Sushanta K. Mitra, "Simulations of Janus droplets at equilibrium and in shear," *Physics of Fluids*, 26:012104 (2014).

droplet.

Simulations of three-component systems have been previously performed using the Cahn-Hilliard model [2, 11] and the free-energy lattice Boltzmann method (LBM) [12]. However, these methods were evaluated for lenses at the interface between two stratified fluids and not adhering droplets. Lenses between two stratified fluids have also been studied by Leclaire et al. [13], who used the colour-model LBM. Another simulation method, the multicomponent LBM of Shan and Chen [14], has not been evaluated for lenses or adhering droplets. Hence, the focus of the present work is to evaluate the Shan-Chen method specifically for its ability to simulate Janus droplets. Though phase separation is automatic in the Shan-Chen LBM, a disadvantage of the method is that interfacial tensions are not input parameters and a theoretical equation that relates interfacial tensions to input parameters is not available [15]. Therefore interfacial tensions must be determined "empirically" from simulations by applying the Young-Laplace law to droplet interfaces and their pressure jumps. Since interfacial tensions specify the equilibrium geometry of adhering droplets, we derive equations for calculating interfacial tensions from the equilibrium geometry. We show that the Young-Laplace law and the equilibrium geometry provide consistent results for the interfacial tensions when using the Shan-Chen LBM to simulate Janus droplets. We then study the rotation of individual Janus droplets in shear flow, as observed experimentally by Torza and Mason [16], as a first step towards gaining insight into the rheology of Janus emulsions and chains[10].

2.2 Equilibrium droplet geometry

The equilibrium geometry of adhering droplets was analyzed by Torza and Mason in a paper published in 1970[16]. However, they did not use the nomenclature of "Janus droplet" or "Janus emulsion" and their work is rarely cited in the literature on these more recent topics. Due to the importance of the equilibrium geometry for analyzing simulations, we briefly review this topic. We also derive convenient explicit equations for measuring interfacial tensions from the equilibrium geometry and for the inverse problem of determining the geometry for known interfacial tensions. The equations could be used, for example, to measure changes in interfacial tensions over time due to diffusion of the three components and their non-zero solubilities in each other[9].

The geometry of a pair of adhering droplets is shown in Fig. 2.1. For the analysis that follows, we consider a cross sectional plane through the centres of the spherical droplets. The analysis is therefore two dimensional, but results are provided for the full three-dimensional geometry as well. The bulk fluid is denoted Fluid 0. The upper droplet consists of Fluid 1,

R_1 is the primary radius of curvature, and the angle between the centre line and the three fluid contact point is θ_1. The definitions are the same for the lower droplet of Fluid 2, but a subscript 2 replaces the 1. The radius of curvature of the interface between the droplets is R_c. Without loss of generality, the lower droplet is assumed to have a higher internal pressure P_2 than the upper droplet (with pressure P_1). The interfacial tension between fluids i and j is denoted σ_{ij}.
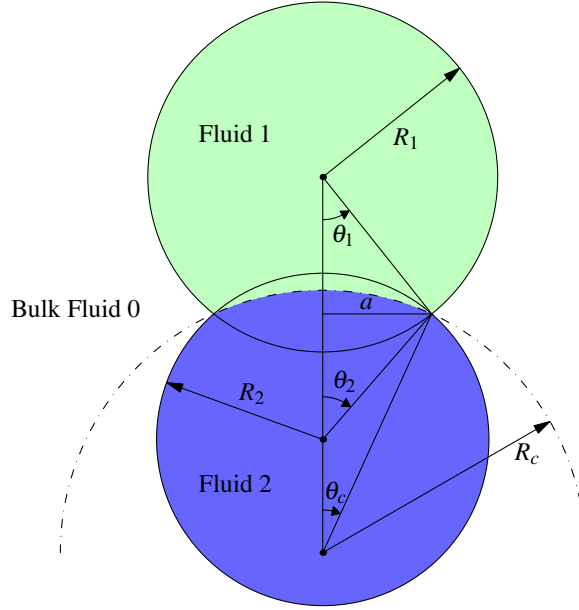
Figure 2.1: Geometry of a cross section through a pair of adhering droplets

As in Torza and Mason [16], a force balance between the interfacial tensions is used to study the equilibrium geometry. Figure 2.2 shows the geometry of the interfacial forces. The horizontal force balance is:

$$\sigma_{01}\cos(\theta_1) + \sigma_{02}\cos(\theta_2) = \sigma_{12}\cos(\theta_c) \tag{2.1}$$

The vertical force balance is:

$$\sigma_{01}\sin(\theta_1) + \sigma_{12}\sin(\theta_c) = \sigma_{02}\sin(\theta_2) \tag{2.2}$$

Since the co-linear circles defined by the radii R_1, R_2, and R_c all intersect at the three fluid contact point, we have the condition that

$$a \equiv R_1\sin(\theta_1) = R_2\sin(\theta_2) = R_c\sin(\theta_c) \tag{2.3}$$

Substitution of Eq. 2.3 into Eq. 2.2 provides

$$\frac{\sigma_{01}}{R_1} + \frac{\sigma_{12}}{R_c} = \frac{\sigma_{02}}{R_2} \tag{2.4}$$

The vertical force balance is therefore equivalent to the Young-Laplace law condition that the pressure jump across one droplet-bulk interface must be the sum of the pressure jumps across the other droplet-bulk interface and the droplet-droplet interface. That is:

$$P_2 - P_0 = (P_2 - P_1) + (P_1 - P_0) \Rightarrow \frac{2\sigma_{02}}{R_2} = \frac{2\sigma_{12}}{R_c} + \frac{2\sigma_{01}}{R_1} \tag{2.5}$$

Here we have used the Young-Laplace law for the pressure jump ΔP across a droplet interface with radius R and interfacial tension σ, which is

$$\Delta P = \xi \frac{\sigma}{R} \tag{2.6}$$

where $\xi = 1$ for a circle in 2D and $\xi = 2$ for a sphere in 3D.
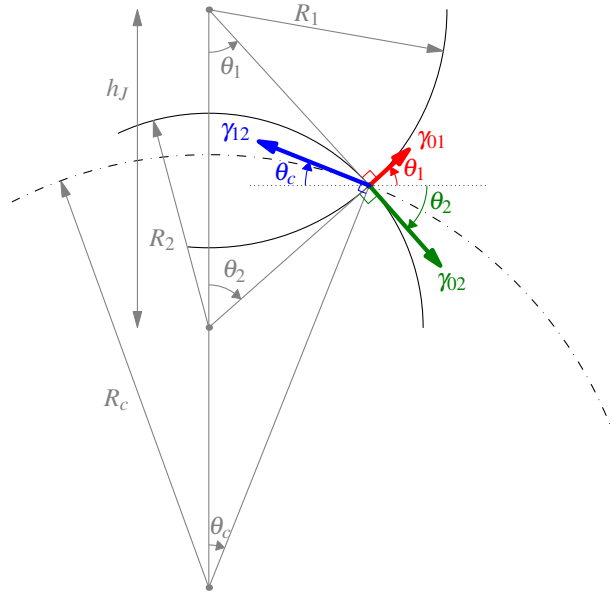
Figure 2.2: Force balance at the three fluid contact point between two adhering droplets

Interfacial tensions and droplet volumes can be determined from measurements of the equilibrium geometry. Using Eqs. 2.1 and 2.4, the ratios of the interfacial tensions as a

function of the angles and radii are:

$$\frac{\sigma_{01}}{\sigma_{12}} = \frac{R_1}{R_c}\left(\frac{R_c\cos(\theta_c) - R_2\cos(\theta_2)}{R_1\cos(\theta_1) + R_2\cos(\theta_2)}\right) \tag{2.7}$$

$$\frac{\sigma_{02}}{\sigma_{12}} = \frac{R_2}{R_c}\left(\frac{R_c\cos(\theta_c) + R_1\cos(\theta_1)}{R_1\cos(\theta_1) + R_2\cos(\theta_2)}\right) \tag{2.8}$$

Alternatively, using Eqs. 2.1 and 2.2, the ratios as a function of only the angles are:

$$\frac{\sigma_{01}}{\sigma_{12}} = \frac{\sin(\theta_2)\cos(\theta_c) - \cos(\theta_2)\sin(\theta_c)}{\cos(\theta_1)\sin(\theta_2) + \cos(\theta_2)\sin(\theta_1)} \tag{2.9}$$

$$\frac{\sigma_{02}}{\sigma_{12}} = \frac{\cos(\theta_1)\sin(\theta_c) + \sin(\theta_1)\cos(\theta_c)}{\cos(\theta_1)\sin(\theta_2) + \cos(\theta_2)\sin(\theta_1)} \tag{2.10}$$

The individual interfacial tensions cannot be determined because the force balance would be satisfied without a change in geometry if all interfacial tensions were to be scaled by the same factor.

For completeness, we provide equations for calculating the cross-sectional areas of the droplets and their volumes. The droplet cross-sectional areas for the geometry shown in Fig. 2.1 are:

$$A_1 = \pi R_1^2 - \frac{1}{2}R_1^2\left(2\theta_1 - \sin(2\theta_1)\right) - \frac{1}{2}R_c^2\left(2\theta_c - \sin(2\theta_c)\right) \tag{2.11}$$

$$A_2 = \pi R_2^2 - \frac{1}{2}R_2^2\left(2\theta_2 - \sin(2\theta_2)\right) + \frac{1}{2}R_c^2\left(2\theta_c - \sin(2\theta_c)\right) \tag{2.12}$$

The droplet volumes are:

$$V_1 = \frac{4}{3}\pi R_1^3 - \frac{\pi R_1^3}{3}\left(2 - 2\cos\theta_1 - \cos\theta_1\sin^2\theta_1\right) - \frac{\pi R_c^3}{3}\left(2 - 2\cos\theta_c - \cos\theta_c\sin^2\theta_c\right) \tag{2.13}$$

$$V_2 = \frac{4}{3}\pi R_2^3 - \frac{\pi R_2^3}{3}\left(2 - 2\cos\theta_2 - \cos\theta_2\sin^2\theta_2\right) + \frac{\pi R_c^3}{3}\left(2 - 2\cos\theta_c - \cos\theta_c\sin^2\theta_c\right) \tag{2.14}$$

Determining the equilibrium geometry explicitly for given interfacial tensions (σ_{01}, σ_{02}, and σ_{12}) and droplet sizes (R_1 and R_2) is more complex. The required angles, inter-

droplet distance, and internal interface curvature are:

$$\theta_1 + \theta_2 = \cos^{-1}\left[\frac{1}{2}\frac{1 - \left(\left(\frac{\sigma_{01}}{\sigma_{12}}\right)^2 + \left(\frac{\sigma_{02}}{\sigma_{12}}\right)^2\right)}{\left(\frac{\sigma_{01}}{\sigma_{12}}\right)\left(\frac{\sigma_{02}}{\sigma_{12}}\right)}\right] \tag{2.15}$$

$$h_J^2 = R_1^2 + R_2^2 + 2R_1R_2\cos(\theta_1 + \theta_2) \tag{2.16}$$

$$\theta_1 = \cos^{-1}\left[\frac{R_1^2 + h_J^2 - R_2^2}{2R_1 h_J}\right] = \cos^{-1}\left[\frac{R_1 + R_2\cos(\theta_1 + \theta_2)}{h_J}\right] \tag{2.17}$$

$$\theta_2 = \cos^{-1}\left[\frac{R_2^2 + h_J^2 - R_1^2}{2R_2 h_J}\right] = \cos^{-1}\left[\frac{R_2 + R_1\cos(\theta_1 + \theta_2)}{h_J}\right] \tag{2.18}$$

$$\theta_c = -\theta_1 + \cos^{-1}\left[\frac{1}{2}\frac{-1 + \left(\left(\frac{\sigma_{01}}{\sigma_{02}}\right)^2 + \left(\frac{\sigma_{12}}{\sigma_{02}}\right)^2\right)}{\left(\frac{\sigma_{01}}{\sigma_{02}}\right)\left(\frac{\sigma_{12}}{\sigma_{02}}\right)}\right] \tag{2.19}$$

$$\frac{1}{R_c} = \frac{1}{R_2}\frac{\sigma_{02}}{\sigma_{12}} - \frac{1}{R_1}\frac{\sigma_{01}}{\sigma_{12}} \tag{2.20}$$

The radii can be related to the areas using Eqs. 2.11 and 2.12; the volumes are specified by Eqs. 2.13 and 2.14.

When ensuring that the arguments of $\cos^{-1}$ are bounded between ± 1, we obtain the same conditions as Chen et al. [9] for equilibrium adhesion of droplets:

$$\sigma_{01} \leq \sigma_{02} + \sigma_{12} \tag{2.21}$$

$$\sigma_{02} \leq \sigma_{01} + \sigma_{12} \tag{2.22}$$

$$\sigma_{12} \leq \sigma_{01} + \sigma_{02} \tag{2.23}$$

If these conditions are not satisfied, the interfacial tensions cannot balance and the droplets will remain separated (when $\sigma_{12} > \sigma_{01} + \sigma_{02}$) or one will engulf the other (when $\sigma_{01} > \sigma_{02} + \sigma_{12}$ or $\sigma_{02} > \sigma_{01} + \sigma_{12}$). An interesting observation is that the conditions for adhesion depend only on the interfacial tensions; the relative sizes of the droplets do not affect the outcome of droplet interactions. This explains why adhering droplets with a wide range of diameters were produced by the bulk emulsification method of Hasinovic et al. [5]. Another consequence of the adhesion conditions is that for a given set of three fluids, changing which phase is the continuous phase can turn a system with engulfing droplets into one with distinct droplets or vice versa. If droplets adhere for one choice of dispersed and continuous phases, the dispersed phase droplets will adhere for all choices.

The special case of a flat interface between adhering droplets must be considered sepa-

rately. The condition for a flat interface is

$$\frac{\sigma_{01}}{R_1} = \frac{\sigma_{02}}{R_2} \tag{2.24}$$

When this condition is satisfied, $R_c \to \infty$ and the pressures in the droplets are equal.

We now apply the results of the geometric analysis to determine interfacial tensions in three-component Shan-Chen LBM simulations. We verify that the correct equilibrium geometry is obtained.

2.3 Simulation method

Systems with multiple immiscible fluids can be simulated using the multicomponent lattice Boltzmann method of Shan and Chen [14]. In this model, multiple fluids are coupled through a repulsive interaction potential that maintains phase separation and provides interfacial tension. For simplicity, two-dimensional simulations were used to study droplet interactions. A regular lattice with nine discrete directions was used (a D2Q9 lattice). For brevity, the details of the lattice Boltzmann method and Shan-Chen multicomponent model are omitted here. Chen and Doolen [17] and Aidun and Clausen [18] provide a review of lattice Boltzmann methods, the multicomponent model is described by Shan and Chen [14] and Shan and Doolen [19], and examples of applications are provided by Yang et al. [20] and Kang et al. [15]. We used a single-relaxation-time BGK collision operator with equal relaxation times for each component of the multicomponent Shan-Chen model. Since separation of the components into liquid and vapour phases is undesirable, each component was treated as ideal. The interaction forces between components were implemented by shifting the velocity used in the calculation of the equilibrium density distribution.

The magnitudes of the repulsive interactions between each pair of fluids are inputs into the Shan-Chen model. The effect of the interaction potential strength on interfacial tension must be determined empirically [15, 20]. This is performed by measuring the interfacial curvature and the pressure difference from simulation data and applying the Young-Laplace law. Pressures in LBM simulations are obtained using an equation of state. For the multicomponent model, the equation of state for the pressure P at each lattice node is [15, 19, 20]

$$P = \frac{1}{3}\sum_k \rho_k + \frac{3}{2}\sum_{k,\bar{k}} g_{k\bar{k}}\rho_k\rho_{\bar{k}} \tag{2.25}$$

where g_{ij} is the interaction potential strength between fluids i and j, k counts over the number of components, and ρ_k is the density of the kth component. The notation $\bar{k}$ denotes the

values of the index that differ from k. The factor of $\frac{3}{2}$ arises from the projection of a four dimensional face-centred hypercubic (FCHC) lattice to two dimensions. Due to this projection, the interaction strengths along the directions of the lattice have different weights. Like the weighting used by Kang et al. [15] for a three-dimensional simulation, we use g_{ij} for the directions with length 1 and $\frac{1}{4}g_{ij}$ for the directions with length $\sqrt{2}$. The values of g_{ij} used in this work are between 0.15 and 0.4 (Table 2.1), ensuring that the components remain separated and the simulations are stable.

2.4 Results and discussion

2.4.1 Equilibrium configurations

Table 2.1 lists the parameters for the six runs that were used to study equilibrium configurations. In all cases, the domain was fully periodic with 256×256 nodes, chosen to ensure adequate resolution of the droplets. For each case, the domain was initialized with two circular droplets of Fluids 1 and 2 in Fluid 0. To ensure slight overlap and therefore interaction between the droplets, the distance between the centres of the circles was 98% of the sum of their radii. The density of each fluid was initialized as 1 where that fluid is present and 0.01 in the remainder of the domain. The relaxation times of all three fluids were one, corresponding to a kinematic viscosity of $\frac{1}{6}$. These values are given in lattice units, with the lattice spacing (length scale), time step (time scale), and reference mass (density scale) all being one.

Table 2.1: Input parameters for the six simulations

Case	g_{01}	g_{02}	g_{12}	R_1	R_2
1	0.30	0.25	0.20	45	45
2	0.23	0.33	0.27	45	45
3	0.30	0.30	0.15	45	45
4	0.26	0.24	0.31	45	27
5	0.17	0.17	0.40	45	30
6	0.15	0.38	0.15	45	30

Figure 2.3 shows the simulation state for each case after 500000 time steps, which was found to be sufficient to achieve steady state in all cases. The circles shown in Fig. 2.3 were determined by fitting circles to points on the interface between each pair of fluids. The interface between fluids i and j was considered to be located where the densities of the two fluids were equal as determined using linear interpolation between nodal values. The centres and radii of the circles were obtained using the least-squares fitting method of Pratt

[21]. This method was chosen due to its robustness when fitting circles with a large radius to data from a small arc such as the interface between two droplets. While the droplets adhere in Cases 1 to 4, they remain separate in Case 5, and one engulfs the other in Case 6.
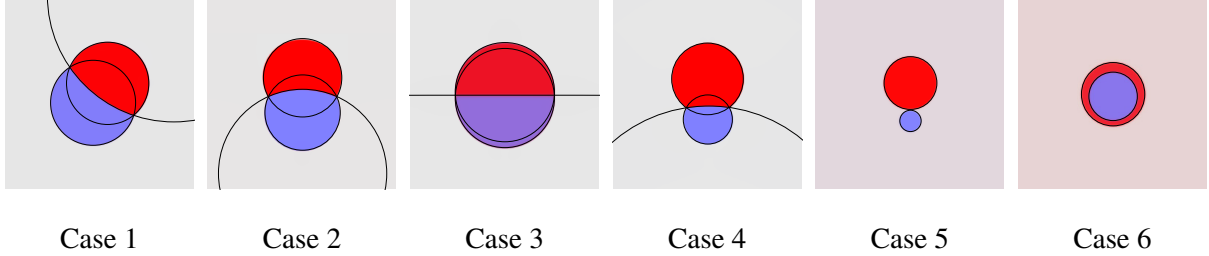
Figure 2.3: Equilibrium droplet shapes for Cases 1 to 6 with circles fitted to the interfaces

Figure 2.4 shows the evolution of the Case 2 simulation from the initial condition towards equilibrium. After the upper fluid spreads over the lower droplet, it retracts slightly before reaching the equilibrium shape.
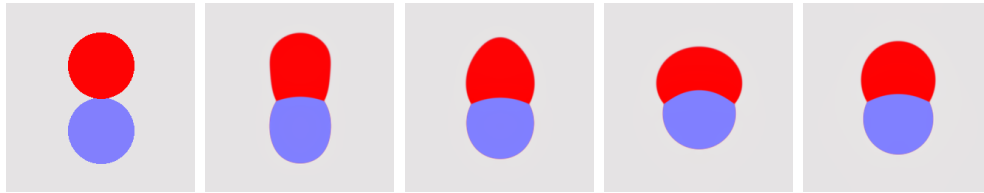
Figure 2.4: Initial droplet shapes followed by the shapes after 1000, 2000, 5000, and 10000 time steps (left to right) for Case 2.

We can obtain the interfacial tensions from the Young-Laplace law by using the radii of the fitted circles and the pressures in each fluid phase. The dependence of the interfacial tension, which was measured in this way, on the strength of the interaction potential is shown in Fig. 2.5. Since the fluid interface is absent for one fluid pair in Cases 5 and 6, the interfacial tensions between those pairs of fluids cannot be obtained by applying the Young-Laplace law. The Young-Laplace law also cannot be used for Case 3 because the interface between the two droplet phases is flat and the pressure difference vanishes. The interfacial tensions can, however, be estimated using a linear least-squares fit to the data in Fig. 2.5. We note that the horizontal axis intercept at $g_{ij} = 0.085$ reflects the fact that the interaction potential strength must exceed a threshold for phase separation to occur. For Case 5, the tension of the interface that is absent at equilibrium is estimated as 0.14; in Case 6, it is 0.13. In both of these cases, the tension of the absent interface exceeds the sum of the tensions of the present interfaces, preventing adhesion of the droplets. In the other cases (1 to 4), the maximum tension is less than the sum of the others, and we obtain adhering droplets. In Case 3, the tension of the flat interface σ_{12} is estimated to be 0.03,

which is about one third of the other two interfacial tensions (0.08), creating the nearly semicircular shape of both droplet phases. The simulation results are therefore consistent with the adhesion conditions, Eqs. 2.21 to 2.23.
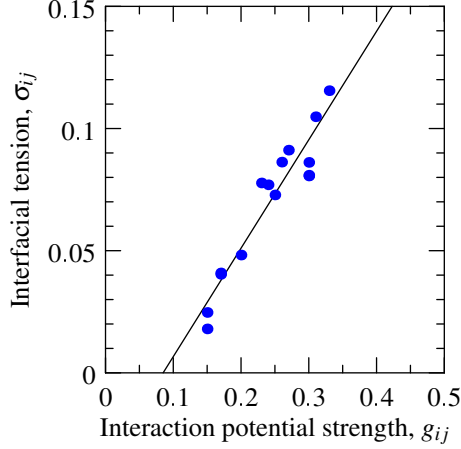
Figure 2.5: Interfacial tension (in lattice units) as a function of interaction potential strength for all cases (dots) together with the least-squares linear fit (line), $\sigma_{ij} = 0.444 g_{ij} - 0.0377$

The interfacial tension ratios determined from the equilibrium geometry are compared with the ratios of the Young-Laplace interfacial tensions in Fig. 2.6. Only the cases in which all three tensions could be determined from the Young-Laplace law are considered, i.e. 1, 2, and 4. The excellent agreement throughout the range of tested ratios indicates that the Shan-Chen LBM for simulating ternary mixtures of immiscible fluids reproduces the expected interfacial force behaviour. The relative differences between the ratios computed using Eqs. 2.7 and 2.8 (shown in Fig. 2.6) versus 2.9 and 2.10 were below 0.2%. The equivalence of the two sets of equations for the tension ratios depends on the geometry satisfying the mutual contact constraint given by Eq. 2.3. The close agreement between the results for the two sets of equations therefore indicates that the three fitted circles all intersect at the same points.

2.4.2 Janus droplets in shear flow

The behaviour of a Janus droplet in shear, and therefore the rheology of Janus emulsions, depends on the shape of the compound drop. Torza and Mason [16] studied the rotation of Janus droplets in shear experimentally, and we now consider analogous simulations. In the simulations of droplets at equilibrium, all four boundaries are periodic. In the simulations of sheared droplets that follow, the left and right boundaries remain periodic while the upper and lower boundaries are replaced with solid walls moving at a constant horizontal
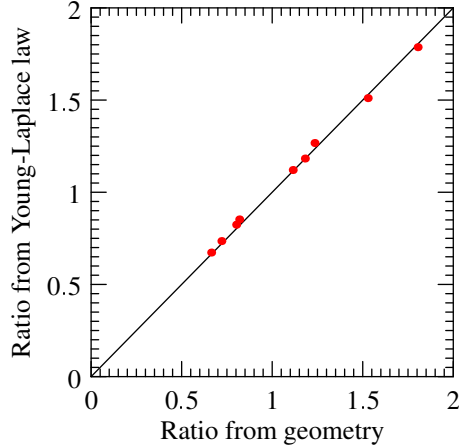
Figure 2.6: Parity plot of the tension ratios obtained from the equilibrium geometry (Eqs. 2.7 and 2.8) and the Young-Laplace law

speed (in opposite directions). These velocity boundary conditions were applied using the method of Ladd [22] to each of the three fluids. This method conserves the mass of each component. In contrast, the boundary condition of Zou and He [23] does not ensure mass conservation, causing problems with the low-concentration components along the boundaries. In simulations with the Zou and He [23] boundary condition, layers with fluid of one of the droplet components formed at the sheared walls.

While the steady-state flow field around a stationary droplet should be zero, spurious currents are present near interfaces in many multiphase fluid simulation methods due to discretization errors. In the Shan-Chen method, spurious currents are the result of discretization in density gradient calculations and a consequent lack of isotropy[24]. Figure 2.7 shows the steady-state spurious currents for Cases 2 and 3 (in Table 2.1). The maximum spurious current magnitudes occur at the nodes along the interfaces and are of order 10^{-2}. As shown in Fig. 2.7, the spurious currents then rapidly decrease by an order of magnitude as the distance from the interface increases. Spurious currents are typically of order 10^{-3} at nodes that are at least three nodes away from an interface. The magnitude of the spurious currents imposes a lower bound on the shear speeds that can be considered for simulations of droplets in shear. The characteristic speed $\dot{\gamma}R$, where $\dot{\gamma}$ is the shear rate and R is a characteristic radius of the compound drop, and therefore the wall shear speed must be higher than the speed of the spurious currents. Otherwise, spurious currents dominate, and unphysical results are expected. High shear rates are therefore desirable, but arbitrarily large shear rates cannot be used because flow speeds must be lower than the speed of sound in the LBM simulations $\left(\frac{1}{\sqrt{3}}\right)$ to ensure that incompressible flow is simulated. Due to these constraints on the shear speed, we consider shear speeds u_0 between 0.005 and 0.05 at the

23

walls.
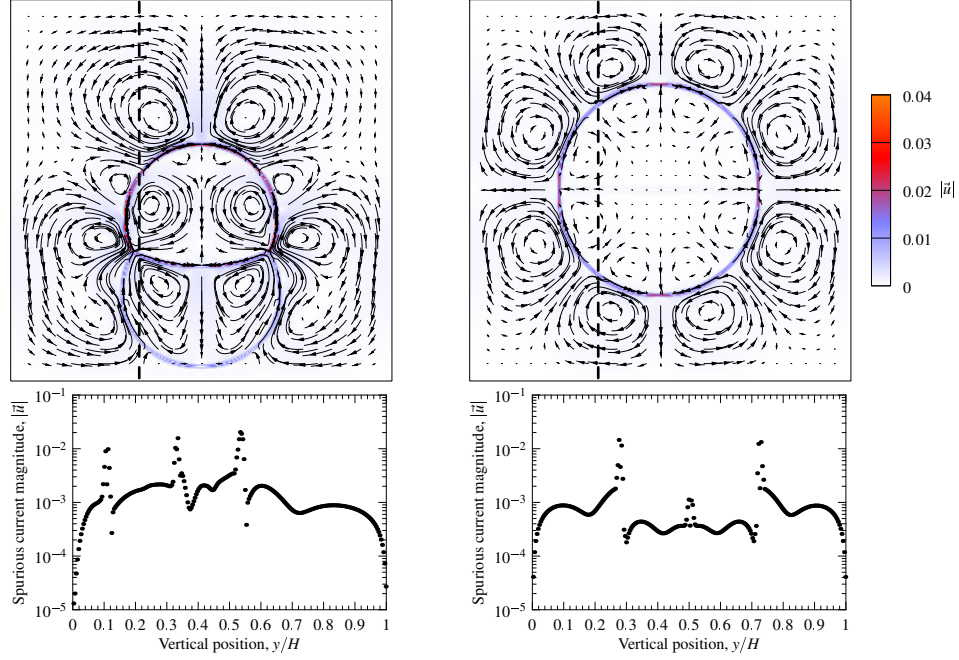
Figure 2.7: Spurious currents at steady state in Cases 2 (left) and 3 (right). The maximum speed is 0.034 in Case 2 and 0.020 in Case 3. The bottom figures show the spurious current magnitudes along the dashed vertical lines in the upper figures.

The behaviour of two types of Janus droplets (Case 2 and 3) in shear was studied to show the effect of the surface tension ratios on the behaviour of one droplet in shear. Figure 2.8 illustrates the behaviour of a Case 2 droplet. For all the simulations of shear flow, the two initial drop radii were 45 lattice nodes. The shear flow was started instantaneously after 100000 time steps of equilibration. The domain size was $W \times H = 256 \times 256$. For droplets in shear flow, we can define a Reynolds number $\mathrm{Re} = \frac{\dot{\gamma} l_c^2}{\nu}$, where $\dot{\gamma} = \frac{2u_0}{H}$ is the shear rate, l_c is a characteristic length, and ν is a kinematic viscosity (all three fluids have $\nu = \frac{1}{6}$). The ratio of viscous and capillary forces is described by a capillary number $\mathrm{Ca} = \frac{\mu \dot{\gamma} l_c}{\sigma}$, where μ is a dynamic viscosity and σ is an interfacial tension. In a system with three fluids and three fluid-fluid interfaces, there are many choices for specifying the capillary number. For the simulations with fixed fluid properties and varying shear rates, it is convenient to define another dimensionless parameter: the ratio of the Reynolds and capillary numbers $\frac{\mathrm{Re}}{\mathrm{Ca}} = \frac{\sigma l_c}{\rho \nu^2}$. This parameter does not depend on the shear rate and contains only geometric and fluid parameters. Using the initial droplet radius (45) as the characteristic length, a fluid density of one, and a typical droplet-bulk interfacial tension of 0.1 (density and tension are in lattice units), we obtain $\frac{\mathrm{Re}}{\mathrm{Ca}} = 162$. With the initial radius of the droplets (45) as the characteristic length and shear speeds between 0.005 and 0.05, the range of Reynolds

numbers is 0.47 and 4.7. For such Reynolds numbers of order 1, capillary numbers are of order 10^{-2}, which indicates that little deformation from a circular interface shape should be expected due to the dominance of interfacial forces over viscous stresses. The absence of noticeable deformation from the equilibrium shape is confirmed in Fig. 2.8.
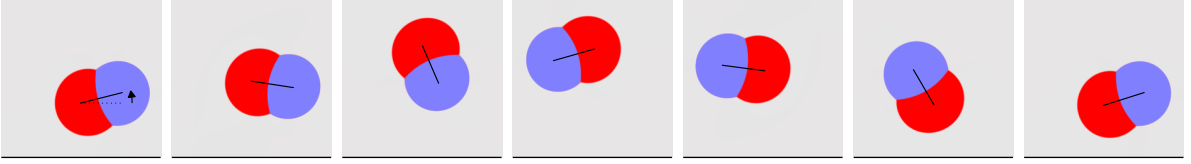
Figure 2.8: Janus droplet in shear at Re $= 0.95$. A solid line connects the centres of mass of the two adhering droplets. The view shifts horizontally with the centre of mass of the red drop. The definition of the orientation angle ϕ is shown in the first frame. Time proceeds from left to right, and the dimensionless time interval between each frame is $\dot{\gamma}t = 3.9$.

The rotation rate of a Janus droplet and the vertical component of its centre of mass at two shear rates (Reynolds numbers) are shown in Fig. 2.9 for one rotation cycle. For Re $\ll 1$, rigid spherical droplets[25] and cylinders in shear[26] rotate at an average angular rate $\omega = \frac{1}{2}\dot{\gamma}$. The speed of a point on the interface of a droplet depends on its position along the interface[25, 27], and the rotation rate of a pair of spheres depends on its angle relative to the flow[28]. We therefore show the dimensionless rotation rate $\frac{2\omega}{\dot{\gamma}}$ as a function of the orientation angle ϕ. The orientation of the Janus droplets was determined by finding the centres of mass of the two constituent droplets. The angle ϕ is the angle between the horizontal axis and the line connecting the centres of mass (this line segment is shown in Fig. 2.8). Rotation rates were obtained using central finite differences. In the two cases, the rotation rates vary around an average of about $\bar{\omega} = 0.35\dot{\gamma}$ with an amplitude of $0.25\dot{\gamma}$. The rotation rates are lowest when the droplet is horizontal, i.e. $\phi \approx 0$; rotation is fastest when $\phi \approx \pi/2$ and the droplet is oriented vertically. The rotation rates are nearly the same for the two Reynolds numbers. Despite the subtle asymmetry in the shape of the Janus droplet, the rotation rate exhibits a periodicity with a period of π with respect to the orientation angle. The vertical motion, however, repeats over a period of 2π. At both Reynolds numbers, the Janus droplet is closest to either wall when the larger-radius (red) portion of the droplet is closer to the wall and the droplet is oriented with the shear flow (i.e. $0 < \phi < \pi/2$ or $-\pi < \phi < -\pi/2$). The amplitude of the vertical motion decreases slightly with increasing Reynolds number. This trend of decreasing amplitude in the vertical motion continues to higher Reynolds numbers; in a simulation with Re $= 4.7$, the droplet did not rotate or move vertically, but instead adopted a steady orientation and vertical position. The changes in behaviour may be due to the increasing effects of confinement and the finite size of the periodic domain with increasing Reynolds numbers. Simulations with larger domains are

25

needed to assess these effects. However, such studies are not currently possible due to the restricted range of parameters in which simulations are feasible. Maintaining the same Re and droplet radius while increasing the domain size by a factor of two (while keeping the relaxation time equal to one for low spurious currents) requires increasing the shear speed by the same factor, making it approach the speed of sound in the LBM.
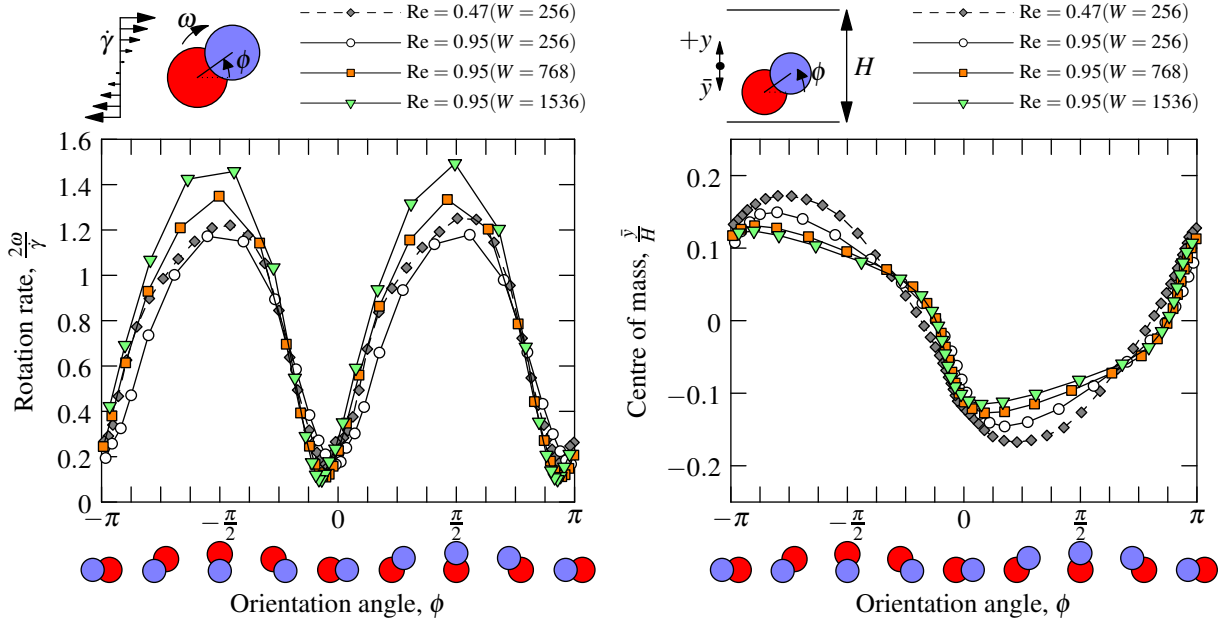
Figure 2.9: Non-dimensional rotation rate (left) of a Case 2 Janus droplet and the vertical component of the centre of mass (right) as a function of the orientation angle at two Reynolds numbers and several domain widths at Re $= 0.95$. Due to the definition of ϕ, time proceeds from right to left (π to $-\pi$).

Simulations in wider domains are possible, and Fig. 2.9 shows the effects of increasing the width of the domain on the motion of a Case 2 Janus droplet sheared at Re $= 0.95$. The size of droplets in these simulations with the Shan-Chen method is the result of an equilibrium between the droplet and bulk concentrations, and therefore the initial concentrations of the droplet components in the bulk (see Section 2.4.1) must be changed as the domain size is increased to ensure that the equilibrium droplet size remains constant. Several simulations were performed to find the required initial concentrations of the two phases in the larger domains that would provide the same drop size as in the smallest domain. Though varying one concentration affects the size of both adhering drops, the effect on the drop of the phase that is not varied is significantly smaller than the effect on the drop of the phase that is varied. Consequently, the two unknown initial concentrations may be determined by independently varying them until the sizes of both drops are correct. In the widest domain, the required drop sizes could not be achieved only by varying the bulk concentration of

the drop phases, and therefore the initial concentration in the drop phase was also varied. Keeping all other parameters constant, increasing the width of the domain alters the rotation and translation of the droplets. The effect of the domain width on the vertical motion is small: the amplitude of the vertical oscillation decreases 19% as the width of the domain increases by a factor of six. Over this six-fold increase in width, the orientations for minimum and maximum rotation rate remain effectively constant, the minimum rotation rate decreases slightly, and the maximum rotation rate increases. The result is a net increase in the average rotation rate from $\bar{\omega} = 0.35\dot{\gamma}$ to $0.4\dot{\gamma}$. The amplitude of the variation in the rotation rate increases from $0.25\dot{\gamma}$ to $0.35\dot{\gamma}$.

For comparison with the Case 2 simulations, the experimental rotation rates obtained for a similar Janus droplet geometry by Torza and Mason [16] are shown in Fig. 2.10. The data for the two shear rates collapse to a single curve with an average rotation rate $\bar{\omega} = 0.5\dot{\gamma}$ and an amplitude of $0.2\dot{\gamma}$. Torza and Mason [16] also measured the periods τ of the rotation, obtaining values of $\dot{\gamma}\tau/4\pi$ between 1.09 and 1.26. In the simulations (Fig. 2.9), the periods are $\dot{\gamma}\tau/4\pi \approx 1.8$ for both Reynolds numbers and independent of the domain width. The periods of rotation in the experiments and simulations may be compared with the period of a rigid ellipsoid with a similar aspect ratio. For a rigid ellipsoid with an axis ratio of 1.3 (a typical aspect ratio of the experimental and simulated Janus droplets), the period of a Jeffery [29] orbit is $\dot{\gamma}\tau/4\pi = 1.03$. The experimental droplets therefore rotate slightly slower than rigid ellipsoids and faster than the simulated droplets. In the experiments, the droplet liquids are 830 (castor oil) and 6400 (silicone oil) times more viscous (dynamic viscosity) than the external liquid (water with surfactant). All three components had similar densities. In the simulations, both the densities and viscosities of the three liquids were nearly the same. Since the rotation rate of fluid spheres increases towards the rate of rigid particles as the viscosity of the internal fluid increases[25], the difference in rotation rates between the experiments and simulations is tentatively attributed to the higher viscosity of the experimental droplets relative to the external fluid. The viscosity ratio between the two droplet fluids is also expected to affect the dynamics of Janus droplets, but the effect may be small when both droplet fluids are significantly more viscous than the external fluid and the capillary number is low, making the Janus droplet move as a rigid body through the external fluid. It should be noted that the simulations are two-dimensional and the effect of this difference between the simulations and experiments has not been evaluated. Since both rigid spheres[25] and cylinders[26] rotate at half the shear rate, the effect of dimensionality on the rotation rate might not be significant, but remains to be verified with three-dimensional simulations. Analyses of the effects of the vertical confinement are also left for future work with three-dimensional simulations.
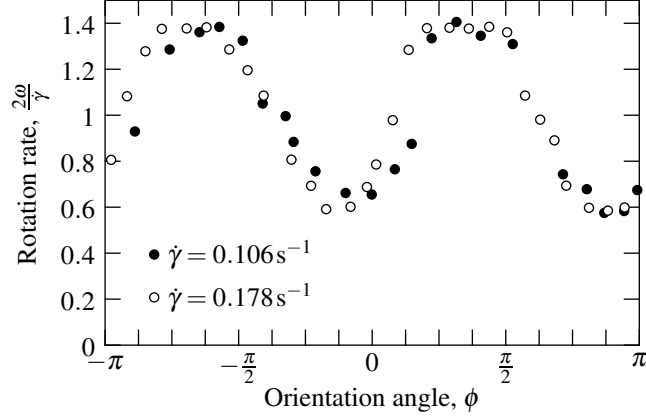
Figure 2.10: Non-dimensional rotation rates of the Janus droplets studied experimentally by Torza and Mason [16] at two shear rates

In simulations with Re < 0.2, the Case 2 Janus droplet did not rotate. At these low shear rates, spurious currents become comparable in magnitude to the imposed shear flow, and the absence of rotation (unlike the low-Re experiments of Torza and Mason [16]) is considered an unphysical effect of the spurious currents. Results at $0.2 < \text{Re} < 0.47$ are not presented because it is unclear if the behaviour is unphysical due to the role of spurious currents.

Case 3 Janus droplets, in which the shape of the adhering droplets is nearly semicircular, behave very differently from Case 2 droplets. One significant difference is the absence of vertical motion: fluctuations in the vertical position of the centre of mass are less than half the lattice spacing. Another difference is in the dependence of the angular velocity on the orientation angle, as shown in Figure 2.11. Results are shown only for Re = 4.7, at which spurious currents do not appear to have a significant effect. With lower Reynolds numbers (0.47, 0.95 and 1.9) the internal flow field relative to rigid rotation (as will be described in the following paragraph) resembled the eight-pole structure of the spurious currents shown in Fig. 2.7. At Re = 4.7, the rotation rate ω fluctuates around a mean of $\bar{\omega} = 0.35\dot{\gamma}$ with an amplitude of $0.1\dot{\gamma}$. Case 3 droplets therefore rotate at about the same average rate as Case 2 droplets, but the amplitude of the fluctuations is significantly lower for Case 3. Furthermore, the maximum and minimum rotation rates no longer occur when the two halves of the Janus droplet are oriented vertically or horizontally. The differences between the two cases are related to the more even distribution of mass around the centre of mass in Case 3. Unlike Case 2, the area exposed perpendicular to the flow does not change significantly as the Case 3 Janus droplet rotates, creating a weaker dependence of the rotation rate on the orientation. A better understanding of the rotation behaviour of Case 3 droplets can be obtained by studying the flow inside them.

28

As for the Case 2 droplets, we examine the effects of increasing the width of the domain on the behaviour of Case 3 Janus droplets. Simulations in a larger horizontal domain assist future comparison of the (two-dimensional) simulations with experiments, which have not been reported for sheared semi-circular droplets. Experiments with (homogeneous) droplets sheared in a narrow gap (only slightly larger than the diameter of the drop) have been performed [30], and therefore experiments are possible with the same ratio $2R/H \approx 0.5$ as in the simulations, where R is the radius of the undeformed, semi-circular Janus droplet. Replicating a periodic domain (with a series of equally-spaced drops) is not practical, but simulations in successively larger domains can be used to evaluate the effect of horizontal periodicity. Maintaining constant drop size while increasing the domain size is easier with Case 3 droplets than with Case 2 droplets because the two drop phases interact identically with the bulk phase. Only one initial concentration therefore needs to be found to keep the sizes of both drops constant. As shown in Fig. 2.11, the change in the rotation rate when doubling the domain size from $W = 768$ to $W = 1536$ is small, indicating that these simulations describe droplets that are not confined horizontally. Comparing the horizontally confined ($W = 256$) and unconfined ($W \geq 768$) cases, the orientations for minimum and maximum rotation speed remain the same, while the rotation speeds are different. For horizontally unconfined droplets, the maximum rotation rate increases to $0.5\dot{\gamma}$ and the minimum rate decreases from $0.25\dot{\gamma}$ to $0.14\dot{\gamma}$. The amplitude of the fluctuation in the rotation rate of unconfined droplets is therefore nearly double the amplitude of confined droplets. The period of the rotation increases from $\dot{\gamma}\tau/4\pi = 1.6$ (confined) to 2.1 (unconfined).

To gain insight into the dependence of the rotation rate on the orientation angle and the difference between the rotation of a Case 3 Janus droplet and a rigid body, we consider the motion of the fluid in the Janus droplet relative to the motion of an equivalently-shaped rigid body that rotates with the same angular velocity. For each orientation ϕ shown in Fig. 2.12, the velocity due to rigid rotation ($\vec{u}_{rot}$) at a rate $\omega(\phi)$ about the centre of mass of the compound droplet was subtracted from the fluid velocity ($\vec{u}$). The streamlines of the resulting velocity field are shown in Fig. 2.12. For reference, the relative velocity field for a cross-section of an undeformed, spherical, homogeneous drop in creeping flow[25, 27, 31] is shown in Fig. 2.13. While simulations at lower Reynolds numbers showed a pattern with eight rotation centres, the streamlines at Re $= 4.7$ clearly differ from the eight-pole spurious current structure (Fig. 2.7). A four-pole vortex structure can be seen in the even-numbered frames. The structure and magnitude of the relative flow are similar to those of the exact solution (Fig. 2.13), supporting the conclusion that the flow is not spurious. Compared to the exact solution, the structure in the deformed drop is only slightly rotated
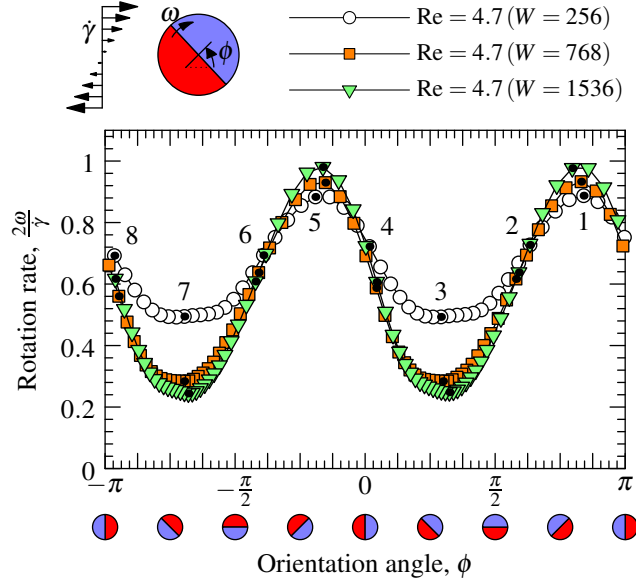
Figure 2.11: Non-dimensional rotation rate of a Case 3 Janus droplet at Re $= 4.7$. Due to the definition of ϕ, time proceeds from right to left (π to $-\pi$). The time interval between consecutive symbols is constant. The filled circles and numbers indicate the positions of the frames shown in Fig. 2.12.

in the direction of the applied shear. The centres of the four vortices remain constant in a stationary reference frame; they do not rotate with the droplet. The upper (right of centre) and lower (left of centre) vortices circulate in the direction of the applied shear, while the left (above centre) and right (below centre) vortices rotate in the opposite direction. When the internal interface passes near two of the vortex centres, the corresponding vortices are not present. Thus, all four vortices are present in frames 2, 4, 6, and 8, while only two are clearly visible in the other orientations. The periodicity with period π in Fig. 2.11 indicates that the simulation results are symmetric with respect to an exchange of the two droplet fluids.

Figure 2.12 also shows the relative velocities in positions 5 to 8 for three horizontal domain sizes. Again, the differences between the simulations with $W = 768$ and $W = 1536$ are small, indicating that the results with these domain sizes represent the behaviour of a droplet that is not confined horizontally. In the two larger domains, the droplets deform more from a circular shape. Horizontal confinement reduces the amplitude of the oscillation in the rotation rate (Fig. 2.11) and the magnitude of the flow relative to rigid rotation, but the structure of the vortices remains generally unchanged.

The rotation rate and vortex structure depend on the orientation of the droplet in the following manner:

30
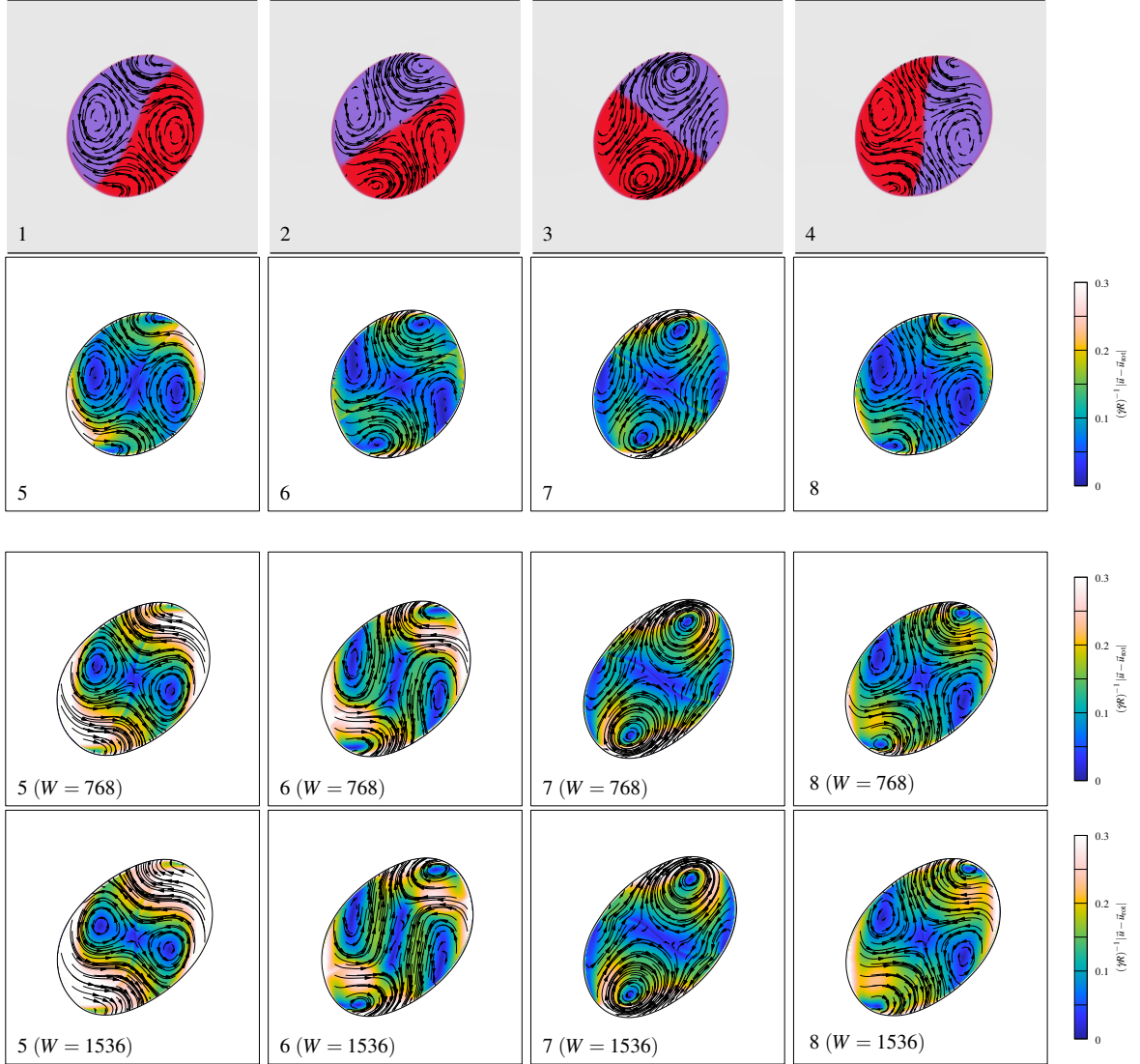
Figure 2.12: Streamlines of the internal flow relative to pure rotation $(\vec{u} - \vec{u}_{\text{rot}})$ at the instantaneous rate $\omega(\phi)$ and different droplet orientation angles ϕ. The numbers shown match the labels in Fig. 2.11. The colour in the upper row identifies the fluid composition; in the lower rows, the colour shows the magnitude of the relative velocity $(\dot{\gamma}R)^{-1}|\vec{u} - \vec{u}_{\text{rot}}|$. The radius R used to scale the velocity magnitude is the radius of the undeformed Janus droplet.

- *Position 1* The droplet rotates fastest in this position. The internal interface is inclined with the applied shear direction. Two vortices are present and both rotate against the applied shear. The (absolute not relative) fluid flow in the vortex near the outer interface therefore moves slower than rigid rotation, while the flow near the centre of the Janus droplet moves faster. As the droplet rotates past position 1, the two vortices decrease in size and the rotation slows.

- *Position 2* All four vortices are present and the rotation rate is halfway between the

31
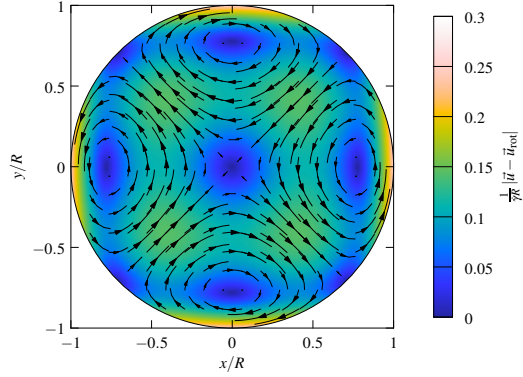
Figure 2.13: Streamlines and velocity magnitude (colour) of the internal flow relative to pure rotation $(\vec{u} - \vec{u}_{\text{rot}})$ at the average rate $\omega = \frac{1}{2}\dot{\gamma}$ for an undeformed drop in Stokes flow[25, 27, 31].

minimum and maximum rates. After position 2, the two vortices that rotate against the shear direction are no longer present, and the two vortices that rotate with the shear flow grow. The growth continues until position 3.

- *Position 3* The rotation rate is slowest, and the vortices are largest. In this position, the internal interface is aligned against the applied shear. Fluid in the vortices moves faster than the local speed due to rigid-body rotation in the region near the outer interface and slower near the centre of the droplet. After position 3, the two vortices shrink and the other two form.

- *Position 4* The two vortices that started forming after position 3 are present, and they rotate against the applied shear. These vortices then grow and the cycle repeats.

Due to symmetry, positions 5–8 are equivalent to positions 1–4. To summarize, the rotation rate is in the upper half of its range when two vortices that rotate against the shear flow are present; the rate is in the lower half when vortices that rotate with the shear flow are present.

2.5 Conclusions

The equilibrium states of Janus droplets in stationary fluid and the rotation of Janus droplets in shear flow were simulated. A force balance model was used to obtain equations for calculating interfacial tension ratios from the equilibrium geometry of a Janus droplet. The inverse problem of determining the equilibrium geometry for known interfacial tensions was also solved. These equations were used to evaluate the use of the two-dimensional Shan-Chen lattice Boltzmann method for simulations of Janus droplets. Excellent agreement was found between the interfacial tensions obtained from the equilibrium geometry and from the Young-Laplace law. Systems with adhering, separated, and engulfed droplets were shown.

Adhering droplets with two different geometries in shear flow were studied in two dimensional simulations. When the geometry of the Janus droplet is two slightly overlapping circles, the Janus droplet rotates fastest when oriented vertically and slowest when horizontal. While the droplet rotates, its centre of mass oscillates between the shear planes. This first type of Janus droplet rotates at an average rate of 70% the rate of solid cylinders in unconfined shear flow. The average rotation rate increases to 80% as the aspect ratio of the domain increases from 1:1 (width:height) to 6:1. In the second type of Janus droplet, the two portions of the droplet had a nearly semicircular shape. These droplets do not oscillate between the shear planes and rotate at the same average rate as the first type. The amplitude of the fluctuation in the rotation rate is smaller for the second type of droplet, and the orientations for maximum and minimum rotation are also different. The internal flow in the second type of Janus droplet was analyzed by subtracting the rotation of an identically-shaped rigid body from the flow field. A four-pole vortex structure was found, and its structure and magnitude are similar to those of the flow in a sheared homogeneous drop. The vortices are present in nearly constant locations (in a stationary frame of reference; the vortex positions do not rotate with the droplets) provided that the inter-droplet interface does not pass through them. The maximum and minimum rotation rates occur when the internal interface passes through two of the vortex positions, leaving only two co-rotating vortices. These simulations of semicircular Janus droplets were performed in square domains with twice the width and height of the droplet's diameter. In simulations with domains that are sufficiently large to approximate horizontally unconfined droplets, the structure of the vortices remains the same, the average rate of rotation decreases to 60% of the rate of a solid cylinder, and the amplitude of the fluctuation in the rotation rate doubles.

Surface tension ratios determine the geometry and consequently the behaviour of Janus

droplets in shear. Though spurious currents restrict the parameter range in which physically-correct results can be obtained, simulation results with the Shan-Chen method provide insight into the ways that Janus droplets with different geometries behave in shear flow. To determine the feasible parameter range for Shan-Chen simulations of droplets and emulsions in shear, it is recommended to first perform simulations with high shear speeds (0.1 lattice units, near the upper limit for incompressible flow) and well-resolved droplets ($R > 20$ lattice units). The shear speed may then be decreased until unphysical behaviour occurs when spurious currents and the imposed shear flow have comparable magnitudes. The streamlines of the flow with shear should be compared with the streamlines of the spurious currents in the absence of shear to assess whether the effects of spurious currents are small. Based on the results for single droplets, Janus emulsions are expected to exhibit a rich and complex range of behaviours and therefore rheologies. Further work is needed to study droplets in three-dimensional simulations, reduce spurious currents and thus expand the range of feasible parameters, and eventually simulate emulsions of Janus droplets and chains.

References

[1] A. Gunde, T. Babadagli, S.S. Roy, and S.K. Mitra. Pore-scale interfacial dynamics and oil-water relative permeabilities of capillary driven counter-current flow in fractured porous media. *J. Petrol. Sci. Eng.*, 2013.

[2] F. Boyer, C. Lapuerta, S. Minjeaud, B. Piar, and M. Quintard. Cahn-Hilliard/Navier-Stokes model for the simulation of three-phase flows. *Transport Porous Med.*, 82: 463–483, 2010.

[3] Ovid. *Fasti*, volume 1. 8 AD.

[4] P. Hardie. The Janus episode in Ovid's Fasti. *Materiali e discussioni per l'analisi dei testi classici*, 26:46–64, 1991.

[5] H. Hasinovic, S. E. Friberg, and Guo Rong. A one-step process to a Janus emulsion. *J. Colloid Interf. Sci.*, 354:424–426, 2011.

[6] H. Hasinovic and S. E. Friberg. One-step inversion process to a Janus emulsion with two mutually insoluble oils. *Langmuir*, 27:6584–6588, 2011.

[7] N. Pannacci, H. Bruus, D. Bartolo, I. Etchart, T. Lockhart, Y. Hennequin, H. Willaime, and P. Tabeling. Equilibrium and nonequilibrium states in microfluidic double emulsions. *Phys. Rev. Lett.*, 101:164502, 2008.

[8] A.S. Utada, E. Lorenceau, D.R. Link, P.D. Kaplan, H.A. Stone, and D.A. Weitz. Monodisperse double emulsions generated from a microcapillary device. *Science*, 308:537–541, 2005.

[9] D. L. Chen, L. Li, S. Reyes, D.N. Adamson, and R.F. Ismagilov. Using three-phase flow of immiscible liquids to prevent coalescence of droplets in microfluidic channels: Criteria to identify the third liquid and validation with protein crystallization. *Langmuir*, 23:2255–2260, 2007.

[10] J. Guzowski, P.M. Morczyk, S. Jakiela, and P. Garstecki. The structure and stability of multiple micro-droplets. *Soft Matter*, 8:7269–7278, 2012.

[11] J. Kim and J. Lowengrub. Phase field modelling and simulation of three-phase flows. *Interface Free Bound.*, 7:435–466, 2005.

[12] J. Zhang and D.Y. Kwok. A mean-field free energy lattice Boltzmann model for multicomponent fluids. *Eur. Phys. J. Special Topics*, 171:45–53, 2009.

[13] S. Leclaire, M. Reggio, and J.-Y. Trépanier. Progress and investigation on lattice Boltzmann modeling of multiple immiscible fluids or components with variable density and viscosity ratios. *J. Comput. Phys.*, 2013.

[14] X. Shan and H. Chen. Lattice Boltzmann model for simulating flows with multiple phases and components. *Phys. Rev. E*, 47(3):1815–1820, 1993.

[15] Q. Kang, D. Zhang, and S. Chen. Displacement of a three-dimensional immiscible droplet in a duct. *J. Fluid Mech.*, 545:41–66, 2005.

[16] S. Torza and S.G. Mason. Three-phase interactions in shear and electrical fields. *J. Colloid Interf. Sci.*, 33:67–83, 1970.

[17] S. Chen and G.D. Doolen. Lattice Boltzmann method for fluid flows. *Annu. Rev. Fluid Mech.*, 30:329–364, 1998.

[18] C.K. Aidun and J.R. Clausen. Lattice-Boltzmann method for complex flows. *Annu. Rev. Fluid Mech.*, 42:439–472, 2010.

[19] X. Shan and G. Doolen. Multicomponent lattice-Boltzmann model with interparticle interaction. *J. Stat. Phys.*, 81:379–393, 1995.

[20] Z.L. Yang, T.N. Dinh, R.R. Nourgaliev, and B.R. Sehgal. Numerical investigation of bubble coalescence characteristics under nucleate boiling condition by lattice-Boltzmann model. *Int. J. Therm. Sci.*, 39:1–17, 2000.

[21] V. Pratt. Direct least-squares fitting of algebraic surfaces. *SIGGRAPH Comput. Graph.*, 21:145–152, 1987.

[22] A.J.C. Ladd. Numerical simulations of particulate suspensions via a discretized Boltzmann equation. Part 1. Theoretical foundation. *J. Fluid Mech.*, 271:285–309, 1994.

[23] Q. Zou and X. He. On pressure and velocity boundary conditions for the lattice Boltzmann BGK model. *Phys. Fluids*, 9:1591–1598, 1997.

[24] X. Shan. Analysis and reduction of the spurious current in a class of multiphase lattice Boltzmann models. *Phys. Rev. E*, 73:047701, 2006.

[25] W. Bartok and S.G. Mason. Particle motions in sheared suspensions. VII. Internal circulation in fluid droplets (theoretical). *J. Coll. Sci.*, 13:293–307, 1958.

[26] F.P. Bretherton. Slow viscous motion round a cylinder in a simple shear. *J. Fluid Mech.*, 12:591–613, 1962.

[27] F.B. Rumscheidt and S.G. Mason. Particle motions in sheared suspensions. XI. Internal circulation in fluid droplets (experimental). *J. Coll. Sci.*, 16:210–237, 1961.

[28] A. Nir and A. Acrivos. On the creeping motion of two arbitrary-sized touching spheres in a linear shear field. *J. Fluid Mech.*, 59:209–223, 1973.

[29] G.B. Jeffery. The motion of ellipsoidal particles immersed in a viscous fluid. *Proc. R. Soc. Lond. A*, 102:161–179, 1922.

[30] A. Vananroye, P.J.A. Janssen, P.D. Anderson, P. Van Puyvelde, and P. Moldenaers. Microconfined equiviscous droplet deformation: Comparison of experimental and numerical results. *Phys. Fluids*, 20:013101, 2008.

[31] G.I. Taylor. The viscosity of a fluid containing small drops of another fluid. *Proc. R. Soc. Lond. A*, 138:41–48, 1932.

Simulations of droplet coalescence in simple shear flow[1]

3.1 Introduction

Predicting and understanding the conditions for droplet coalescence are important for many applications. At a large scale, emulsions, which consist of drops of one fluid dispersed in another, may be subjected to complex turbulent flows for example during mixing. In such a flow, droplets are sheared and collide, causing breakup and coalescence. The result of these interactions is a particular droplet size distribution[1–3]. Since macroscopic properties, such as the effective viscosity of an emulsion, and mass transfer rates between the fluids depend on the droplet size distribution, it is useful to predict how flow conditions change droplet sizes. To make such predictions, an understanding of when drops break up and coalesce is required. In addition to emulsion flows in large vessels and process equipment, droplet interactions are also important in microfluidic devices in which individual droplets can be formed and manipulated[4–6]. For example, droplets can be formed by injecting one liquid into another in a T-junction or the nozzle of a flow-focusing device[4, 5]. Microfluidic devices can be used to study coalescence directly, and Bremond et al. [7] found that droplets coalesce when separating rather than when they are compressed.

Droplet collisions in shear flow have been studied by several authors. Guido and Simeone [8] used optical microscopy to measure droplet trajectories during collisions in simple shear. They did not, however, determine the conditions for coalescence. Leal and co-workers[9–12] used a four-roll mill to determine the conditions for coalescence under varying system parameters. Their results are for predominantly extensional flows (flows with streamlines towards and away from a stagnation point), rather than simple shear flows. More recently, Chen et al. [13] studied the effect of confinement on droplet coalescence

---

[1]A version of this chapter has been published as Orest Shardt, J.J. Derksen, Sushanta K. Mitra, "Simulations of droplet coalescence in simple shear flow," *Langmuir*, 29:6201–6212 (2013).

in simple shear. The experimental results identify parameter ranges over which the transition from coalescence to non-coalescence occurs, and they are useful for comparisons with simulations. In general, there are two motivations for using simulations to study coalescence. The first reason is to gain an understanding of coalescence by obtaining data and using initial conditions that are experimentally impractical. The second reason is to verify the accuracy of the simulation method so that simulations of coalescence in more complex systems can be used to predict or optimize the performance of that system. For example, simulations of polydisperse emulsion flows must correctly model the dependence of the conditions for coalescence on the size of the droplets.

The outcome of a droplet collision is a macroscopic event that depends on phenomena at a much shorter length-scale[14]. As two droplets approach, the fluid between them drains. If this drainage continues long enough and the film between the droplets becomes sufficiently thin, attractive intermolecular forces across the film dominate and a bridge forms between the droplets. This bridge grows due to capillary forces, and the droplets coalesce. For a surfactant-free mixture of two polymers, such as the polydimethylsiloxane (PDMS) and polyisobutylene (PIB) studied by Chen et al. [13], van der Waals forces determine the minimum film thickness before a bridge forms. An order-of-magnitude estimate of this critical thickness is 27 nm [13]. In comparison, typical droplet diameters in emulsions and microfluidic devices range from 1 to 500μm, factors of 37 to 18500 times larger than this sample critical film thickness.

The range of length scales poses significant challenges for fully resolved simulations of droplet collisions and coalescence. When simulating such a system, one must use an exceedingly fine uniform mesh, a non-uniform mesh with significant refinement in the vicinity of interacting interfaces, or multi-scale modelling that incorporates the effects of phenomena at a small scale into larger more coarsely-resolved simulations. In general, simulations of droplets have been performed using interface-tracking or interface-capturing methods[15]. Interface-tracking methods use meshes or other computational elements that lie on the interface. In these methods, the interface is "sharp" because fluid properties vary discontinuously over the interface. Examples of interface-tracking methods include the boundary integral, finite element, and immersed-boundary methods [15]. Loewenberg and Hinch [16] used the boundary integral method to simulate binary drop collisions in shear flow. They did not, however, include attractive forces in the simulations and did not therefore simulate coalescence. The boundary integral method has also been used to study the flow of concentrated emulsions[17, 18] in periodic domains and model porous media[19]. Simulating topological changes, i.e. breakup and coalescence, in interface-tracking methods is computationally challenging due to the mesh transformation that must be performed.

The methods also require a somewhat arbitrary choice about the distance when two interfaces are close enough that they should merge or pinch-off. Such a critical distance may not actually be a constant; Leal [11] notes the critical film thickness may depend on the droplet radius. Because a length-scale must be provided as an input to the model, the use of these simulation methods requires prior knowledge of this length, making the methods non-predictive.

Unlike interface-tracking methods, interface-capturing methods do not explicitly describe the position of the interface. Instead, a scalar identifies regions of different composition and the interface is located where this scalar equals a constant value that is typically zero or one half. Fluid properties vary continuously over the diffuse interface between two fluids. Examples of such methods include lattice Boltzmann, level-set, volume-of-fluid (VoF), and phase field models[15]. Changes in interface topology are handled automatically by these methods. However, it is necessary to understand the conditions when these changes (breakup and coalescence) occur in simulations and if the conditions match experiments. In some interface-capturing methods, the critical distance between interfaces for coalescence and breakup is determined by the grid, in contrast to the arbitrary (but specified) critical distance for interface-tracking methods. In the VoF and level-set methods, two interfaces connect when the chosen grid cannot resolve the gap between them (see e.g. Tryggvason et al. [20]). For example, the VoF method aims at simulating non-interacting sharp interfaces. As Zaleski et al. [21] mention, a cutoff length-scale is introduced and interfacial physics below this length scale are ignored. The cells in the simulation domain have compositions of zero or one, except those cells that contain an interface. In these cells, the composition varies continuously between zero and one. The interfaces of colliding droplets connect when the chosen grid resolution can no longer resolve the two interfaces. Consequently, the conditions for coalescence are expected to depend on the cell size, though a detailed analysis, analogous to the present lattice Boltzmann method (LBM) work, is required to confirm the nature of the dependence. Grid-dependence is expected because the film between two droplets is resolved better as the mesh is refined, decreasing the critical thickness for rupture. As a result, a longer time is needed for the film to drain before rupturing. Coalescence would therefore occur later in higher-resolution simulations. In contrast, as we show in the "Interface resolution" section, we obtain grid-independent results with high-resolution free-energy LBM simulations. Similar results are expected with other phase-field methods, but LBMs are convenient to parallelize, making high-resolution simulations practical.

Lattice Boltzmann methods have seen much popularity for simulating microfluidic flows [22]. While several multiphase and multicomponent LBMs have been proposed, we

focus on the binary-liquid free-energy method[23] due to its thermodynamic treatment of fluid mixtures. Simulations of droplet formation have been successful[24] with this method, and the deformation and breakup of droplets has been studied in detail to determine the numerical parameters that are required for accurate simulations[25]. The conditions for coalescence, however, have not been studied in detail, though other researchers have noted that droplets coalesce too easily [26]. While droplet coalescence in microfluidic devices has been studied experimentally[6, 7, 27, 28], it is not currently possible to predict such coalescence phenomena with simulations. The need to study simulations of droplet coalescence in detail is underscored by the development of non-coalescing emulsion models by several researchers[29, 30]. Though these models can be used for flow conditions when coalescence does not occur, such models with suppressed coalescence cannot be used to study the transition to coalescence. Therefore, there is a need to characterize the coalescence behaviour of existing simulation models, investigate the previously-noted discrepancy between simulations and experiments, and determine whether conditions can be found in which droplets do not coalesce.

Due to the thermodynamic treatment of the diffuse interface, i.e. the use of a Cahn-Hilliard fluid model, the behaviour of fluid interfaces in the free-energy LBM can be related to van der Waals forces. This is an important advantage over other methods in which a specified length or the grid resolution determines the conditions for coalescence. The connection between the free-energy model and interfacial forces has been explained, for example, by Yue et al. [31], who studied coalescence after a head-on collision with a spectral phase-field method. Dupuy et al. [32] used an LBM with a Cahn-Hilliard free-energy model to study the coalescence of liquid droplet pairs in vapour. Premnath and Abraham [33, 34] also studied liquid droplets in vapour, but considered both head-on and off-centre collisions. They showed several cases of coalescence and splitting after temporary coalescence, but no cases where the interfaces never merged. The results agreed with experimental findings. Their work, however, is in the high Reynolds number regime ($\text{Re} \approx 50$), and the easy coalescence noted by Jia et al. [26] occurs at low Reynolds numbers ($\text{Re} < 1$). Different LBMs, i.e. other than the free-energy LBM, have also been used to study droplet collisions at high Reynolds numbers. Inamuro et al. [35], Lee and Lin [36], and Sun et al. [37] focused on achieving high density ratios between the liquid and vapour phases. Chiappini et al. [38] used a (two-dimensional) finite-difference lattice Boltzmann method[36] to study the Rayleigh-Taylor instability, droplet breakup, and droplet coalescence, while Lycett-Brown et al. [39] studied collisions with an improved Shan-Chen[40] LBM for liquid-vapour systems. To the authors' knowledge, studies of droplet collisions in liquid-liquid systems that are similar to those for liquid-vapour systems have not been

reported. Perlekar et al. [41] studied large numbers of droplets (approximately 10 to 50) in turbulence using the Shan-Chen method, but the behaviour of a colliding pair of droplets was not investigated. Interestingly, simulations of droplet collisions and coalescence using the colour-model LBM[42, 43], the third LBM model that is commonly used for multi-phase simulations, have not been reported. Simulations of deformation and breakup[44] and droplet formation in a microfluidic channel[45, 46] have been described. Due to this success, the colour-model LBM may be a good candidate for coalescence simulations, but a comparison of coalescence behaviour in the colour-model and free-energy LBMs is beyond the scope of the current work. It should be noted that a link between numerical interface parameters in the color-model LBM and intermolecular forces is not immediately evident, suggesting a disadvantage of this model in comparison to the free-energy method.

In this work, we quantify the conditions for coalescence in the free-energy LBM during collisions of two liquid droplets in a liquid matrix. The Reynolds number is fixed at one, a low value that is efficient to simulate with this explicit numerical method. We determine the effects of droplet size, diffuse interface thickness, interface diffusivity, vertical offset between the droplets, and droplet confinement. This information is important for knowing the conditions when simulations of multiphase microfluidic flows and fully-resolved simulations of emulsions in turbulence correctly model droplet coalescence.

3.2 Coalescence theory

A schematic of the coalescence problem that we simulate is shown in Fig. 3.1. Two initially spherical droplets of radius R are initialized with a horizontal distance ΔX and a vertical distance ΔY between their centres in a domain with a height H between the shear planes. A shear flow with a rate $\dot{\gamma} = \frac{2u_0}{H}$, where u_0 is the horizontal speed of the two shear planes, is started impulsively. The interfacial tension (or energy) between the droplet liquid and the surrounding liquid is σ. We do not currently study the effects of density or viscosity differences between the two liquids. Both liquids therefore have the same density ρ and kinematic viscosity ν. A domain with a finite length L and a finite depth W is used to represent a domain that is infinite in these dimensions. Thus the domain size is chosen to be large enough that the effects of the finite size can be neglected, and the adequacy of the choice is verified in the section "Domain size effect." To use available computational resources efficiently, we use symmetry boundary conditions and simulate only one quarter of the whole system as shown in Fig. 3.1.

The physical parameters give rise to several non-dimensional parameters. Hydrodynamic similarity is specified by the Reynolds number Re, which we define using the char-
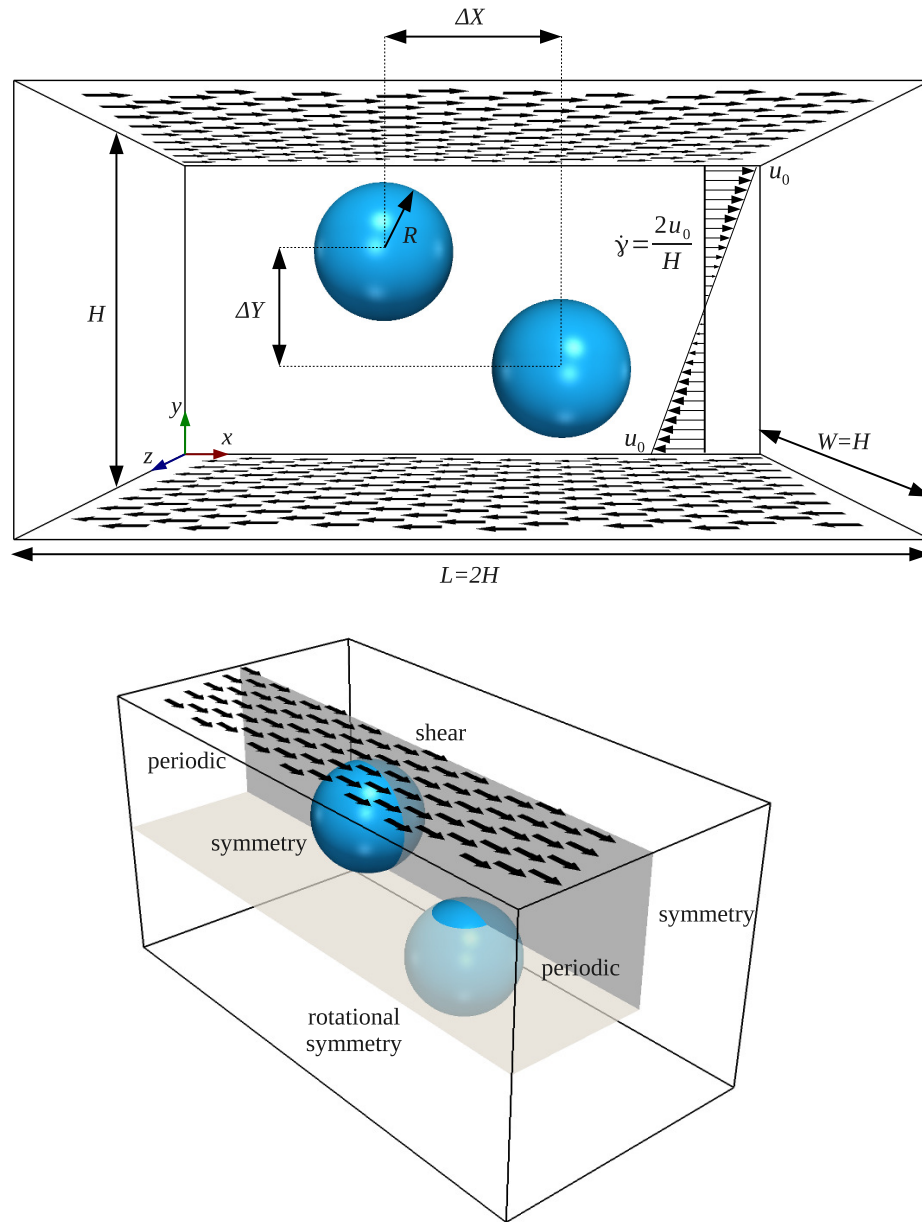
Figure 3.1: Schematics of the system geometry (top) and simulation domain (bottom). Two droplets with radii R are located between two shear planes that are a distance H apart and move at a speed u_0 in opposite directions. The horizontal (parallel to the shear planes) distance between the centres of the droplets is ΔX; the vertical distance is ΔY. The definitions of the coordinate axes and domain dimensions are also provided. Due to the symmetry of the full system (top), only one quarter is simulated (bottom). The boundary conditions on each face of the simulated domain are shown.

acteristic velocity $\dot{\gamma}R$ and the droplet radius R as the characteristic length:

$$\text{Re} \equiv \frac{\dot{\gamma}R^2}{\nu} \tag{3.1}$$

The effects of surface tension are captured by the capillary number Ca, which is the ratio of viscous ($\mu\dot{\gamma}R^2$) and interfacial (σR) forces:

$$\text{Ca} \equiv \frac{\mu\dot{\gamma}R}{\sigma} \tag{3.2}$$

where $\mu = \rho\nu$ is the dynamic viscosity of both fluids. The geometric parameters are the confinement $\frac{2R}{H}$, the horizontal separation $\frac{\Delta X}{2R}$, and the vertical offset $\frac{\Delta Y}{2R}$.

The outcome of a collision is determined by the capillary number. With increasing capillary number, the deformation of droplets increases as the interfacial forces that keep a drop spherical give way to the viscous forces that shear the droplet. When droplets are deformable, their interfaces flatten when they are pushed together in a shear flow. The fluid film that forms between the droplets must drain before the interfaces can come close enough that intermolecular forces dominate and the interfaces merge. If the film does not thin sufficiently over the time of a collision, the drops slide over each other; otherwise they coalesce. As the capillary number decreases, the reduced deformability of the droplets suppresses the formation of a flat film. In the limit of high surface tension (Ca $\ll$ 1), the drops would remain effectively spherical and a flat film could not form to delay coalescence. Thus, droplets cannot coalesce when the capillary number is sufficiently high and they coalesce when it is sufficiently low. There is therefore a critical capillary number Ca_c, and droplets coalesce when Ca $< \text{Ca}_c$; they slide when Ca $> \text{Ca}_c$.

The outcome of a collision is determined by hydrodynamic, capillary, and geometric effects, as well as a characteristic length scale l_c at which intermolecular forces become important and destabilize the thin film that separates colliding droplets. The dependence of these factors on the critical capillary number can be expressed as

$$\text{Ca}_c = \text{Ca}_c\left(\text{Re}, \frac{\Delta X}{2R}, \frac{\Delta Y}{2R}, \frac{2R}{H}, \frac{R}{l_c}\right) \tag{3.3}$$

3.3 Numerical method

We use the free-energy lattice Boltzmann method for binary liquid mixtures[23]. In this method, two discrete density distributions f_i and g_i model the hydrodynamics and the evolution of a phase field, respectively. A brief overview of the method is provided here to

establish the definitions that are required for this chapter; more details about the method and theory can be found elsewhere [22–24, 47–50]. In general, lattice Boltzmann methods solve advection-diffusion equations through a two-step process that mimics the behaviour of molecules in a gas. In the first step, the densities at each lattice node are propagated to adjacent nodes along a set of discrete directions $\vec{c}_i$, where i identifies the discrete direction. We use a three-dimensional lattice with 19 discrete directions, i.e. a D3Q19 lattice, for both density fields. The second step imitates the effect of collisions between molecules by relaxing the densities at each node towards an equilibrium distribution. Thus, the density distributions f_i and g_i evolve according to

$$f_i(\vec{x}+\vec{c}_i\Delta t, t+\Delta t) = \left(1 - \frac{1}{\tau_f}\right) f_i(\vec{x},t) + \frac{1}{\tau_f} f_i^{eq}(\vec{x},t) \tag{3.4}$$

$$g_i(\vec{x}+\vec{c}_i\Delta t, t+\Delta t) = \left(1 - \frac{1}{\tau_g}\right) g_i(\vec{x},t) + \frac{1}{\tau_g} g_i^{eq}(\vec{x},t) \tag{3.5}$$

where τ_f and τ_g specify the relaxation rates. By relating macroscopic values to the density distributions and appropriately choosing the equilibrium distributions f_i^{eq} and g_i^{eq}, the simulations model the required continuum equations. For the f_i field, the macroscopic density and momentum are

$$\rho = \sum_i f_i \tag{3.6}$$

$$\rho\vec{u} = \sum_i f_i\vec{c}_i \tag{3.7}$$

and the equilibrium distribution is

$$f_i^{eq} = A_i + B_i\vec{u}\cdot\vec{c}_i + C_i\vec{u}\cdot\vec{u} + D_i(\vec{u}\cdot\vec{c}_i)^2 + G_{i,\alpha\beta}c_{i,\alpha}c_{i,\beta} \tag{3.8}$$

where index notation has been used for the last term and summation over repeated Greek indices is implied. The coefficients A_i, B_i, C_i, D_i and G_i must satisfy conservation constraints, but these constraints do not determine the coefficients uniquely. We use coefficients that minimize spurious currents[51]. With these definitions of the macroscopic variables and equilibrium function, the f_i field simulates the mass conservation (continuity) equation

$$\frac{\partial \rho}{\partial t} + \nabla \cdot (\rho\vec{u}) = 0 \tag{3.9}$$

and the incompressible Navier-Stokes equation

$$\frac{\partial \vec{u}}{\partial t} + (\vec{u}\cdot\nabla)\vec{u} = -\frac{1}{\rho}\nabla P + v\nabla^2\vec{u} \tag{3.10}$$

where the pressure is determined with the equation of state $P = \frac{1}{3}\rho$ and the kinematic viscosity is related to the relaxation rate by $v = \frac{1}{3}\left(\tau_f - \frac{1}{2}\right)$. In the limit of incompressible flow, Eq. 3.9 simplifies to

$$\nabla \cdot \vec{u} = 0 \tag{3.11}$$

To simulate incompressible flow, flow speeds must be kept low, and we achieve this by limiting the shear speed to approximately 0.02 lattice units per time step.

For the phase field, the scalar φ specifies the composition of the fluid, and it varies between -1 (continuous phase) and 1 (droplet phase). It is determined from the density distribution g_i by

$$\varphi = \sum_i g_i \tag{3.12}$$

The continuum equation for φ is

$$\frac{\partial \varphi}{\partial t} + \nabla \cdot (\varphi \vec{u}) = M \nabla^2 \mu_\varphi \tag{3.13}$$

In this advection-diffusion equation for φ, M is the diffusivity of the chemical potential μ_φ. This diffusivity is determined by the relaxation time τ_g and a free parameter Γ according to $M = \Gamma\left(\tau_g - \frac{1}{2}\right)$, while the chemical potential is determined by the free-energy of the system. The free-energy functional $F[\varphi(\vec{x})]$ is [23]

$$F = \int_V \left[\frac{1}{3}\rho \ln \rho + \frac{1}{2}\varphi^2\left(-A + \frac{B}{2}\varphi^2\right) + \frac{\kappa_\varphi}{2}(\nabla\varphi \cdot \nabla\varphi)\right] \mathrm{d}V \tag{3.14}$$

The first term provides an ideal gas equation of state, the second term is a double-well potential that causes phase separation at minima with compositions of $\varphi_0 = \pm\sqrt{\frac{A}{B}}$, and the third term creates interfacial energy by associating energy with changes in φ. The parameters A and B specify the shape of the double-well potential. To have two phases with $\varphi_0 = \pm 1$, we use $A = B$. The magnitude of the energy due to concentration gradients is determined by the parameter κ_φ. The chemical potential for this free energy is

$$\mu_\varphi = \frac{\delta F}{\delta \varphi} = -A\varphi + B\varphi^3 - \kappa_\varphi \nabla^2 \varphi \tag{3.15}$$

The one-dimensional steady-state solution for φ between two infinite domains provides important information about the interface, specifically its characteristic thickness and excess energy. The solution is[23]

$$\varphi(x) = \varphi_0 \tanh \frac{x}{\ell_\varphi} \tag{3.16}$$

The length scale $\ell_\varphi = \sqrt{\frac{2\kappa_\varphi}{A}}$ characterizes the thickness of this diffuse interface. Though 96.4% of the total change in φ across an interface occurs over a distance $4\ell_\varphi$, the length ℓ_φ is often called the interface thickness. The excess interfacial energy of this interface profile is

$$\sigma = \frac{2\sqrt{2}}{3}\sqrt{\kappa_\varphi A} \tag{3.17}$$

For the large droplet sizes that are used in this work ($R > 20$ lattice nodes), the interfacial energy for a planar interface provides a good estimate of the energy of a spherical interface[26].

In this first detailed characterization of the coalescence of droplets in LBM simulations, we keep several parameters constant and leave studying their effects as future work. To minimize spurious currents and enhance stability, we keep the two relaxation rates fixed ($\tau_f = \tau_g = 1$). Consequently, $\nu = \frac{1}{6}$ and $M = \frac{\Gamma}{2}$. The Reynolds number is fixed at one, and we consider pairs of fluids with equal densities and viscosities. In earlier work[52], the critical capillary number for film rupture was found to be independent of the Reynolds number over the range $0.2 < \text{Re} < 1.4$ in simulations with $R = 25$.

To maximize the droplet size that can be simulated with available computational resources, we take advantage of the symmetry in the full domain and simulate only one quarter of it. As shown in Fig. 3.1, the quarter-domain has two periodic boundaries, two symmetry boundaries, a rotational symmetry condition at the bottom ($y = \frac{1}{2}H$), and a shear plane on top ($y = H$). The shear velocity condition $\vec{u}|_{y=H} = (u_0, 0, 0)$ on this plane was implemented using the method of Ladd [53]. This method was chosen because it ensures mass conservation (unlike e.g. the method of Zou and He [54]), an important feature for the long simulation times that are used to study droplet collisions.

The central results of this chapter are the effects of the parameters in the free-energy model on the outcome of a simulated droplet collision. The model provides a convenient choice for the characteristic length l_c: the characteristic length ℓ_φ of the diffuse interface thickness. The Péclet number

$$\text{Pe} = \frac{\dot{\gamma} R \ell_\varphi}{MA} \tag{3.18}$$

is the ratio of the time scales of advection and chemical potential diffusion over a length scale given by ℓ_φ[24]. Using $l_c = \ell_\varphi$ and including the Péclet number, we write

$$\text{Ca}_c = \text{Ca}_c \left(\text{Re}, \frac{\Delta X}{2R}, \frac{\Delta Y}{2R}, \frac{2R}{H}, \frac{R}{\ell_\varphi}, \text{Pe} \right) \tag{3.19}$$

We study the effects of the droplet size relative to the interface thickness $\frac{R}{\ell_\varphi}$, the interface Péclet number Pe, the confinement $\frac{2R}{H}$, and the vertical offset $\frac{\Delta Y}{2R}$ on Ca_c at constant Re and

$\frac{\Delta X}{2R}$ to determine whether free-energy LBM simulations can be used to accurately model the physical problem. Other numerical factors that may affect the results, such as the relaxation rate, are kept constant. We study a parameter range in which the effects of the parameters on the critical capillary number can be determined with the computational resources that are currently available to us. We hypothesize that the model parameter ℓ_φ can be related to a physical l_c so that the simulations represent the physical situation when $\frac{R}{\ell_\varphi}$ and $\frac{R}{l_c}$ are matched. If this is correct, the effective physical size of the simulated droplets can be determined from the experimental size of a droplet system with the same Ca_c, Re, and geometry.

3.3.1 Implementation

A highly-parallel code was used to simulate the large domains that are required to discern the effects of the parameters on the outcome of a collision. The smallest ($R = 25$ lattice nodes) simulations were performed on a single graphics processing unit (GPU). The largest ($R = 100$ lattice nodes) simulations were parallelized over nine GPUs (NVIDIA Tesla M2070), with three GPUs per computational node. For these multi-GPU simulations, only one CPU core (Intel Xeon E5649) was used on each node for communication. This communication was implemented with a Message Passing Interface (MPI) library. Sample performance data for the simulations are listed in Table 3.1. All computations were performed with double (64 bit) precision. The memory bandwidth that is shown is an effective bandwidth that includes only memory transfers that are required by the LBM calculations; memory transfers for communication are excluded. The speed is measured in million lattice updates per second (Mlups). For the largest domain size, 232 Mlups is approximately 300000 time steps per day. The corresponding non-dimensional strain for 300000 time steps at Re $= 1$ and $R = 100$ is $\dot{\gamma}t = 5$.

Table 3.1: Performance of the simulation software with different domain sizes and types of parallelization

Nodes	GPUs	Domain Size (lattice nodes)	Drop Radius, R (lattice nodes)	GPU Memory (GB)	Bandwidth (GB/s)	Speed (Mlups)
1	1	$256 \times 64 \times 64$	25	0.5	75	40.8
1	3	$256 \times 64 \times 64$	25	0.5	132	72.8
3	9	$1024 \times 256 \times 256$	100	34	426	232

3.4 Results and discussion

Many parameters remain constant for all the simulations that are presented in this section, unless specified otherwise. These parameters are: $Re = 1$, $\ell_\varphi = 2$, $Pe = 10$, $\frac{\Delta X}{2R} = 1.26$, $\frac{\Delta Y}{2R} = 0.86$, and $\frac{2R}{H} = 0.39$.

3.4.1 Interface resolution

Before studying the conditions that determine when colliding droplets coalesce, we first examine whether the simulation results are sensitive to the resolution of the interface and the size of the periodic domain. To determine if the interface is adequately resolved with $\ell_\varphi = 2$, simulations with twice this resolution were also performed. As illustrated in the upper portion of Fig. 3.2, the transition from $\varphi = -1$ to $\varphi = 1$ occurs over a distance of about 8 nodes when the characteristic length ℓ_φ of the diffuse interface is 2. With $\ell_\varphi = 4$, the distance is 16 nodes. Since the higher-resolution interface profile is effectively identical to the lower-resolution profile, the interface is judged to be well-resolved at the lower resolution.

Three capillary numbers were considered to see the effect of the interface resolution on the outcome of a collision. All the simulations, shown in Fig. 3.2, were performed with the same geometry, Reynolds number (1), Péclet number (10), and $R/\ell_\varphi = 18.75$. The simulation at the lower resolution had a droplet radius of 37.5, a domain size of $384 \times 96 \times 96$, and an interface thickness of $\ell_\varphi = 2$; the simulation with $R = 75$ was in a $768 \times 192 \times 192$ domain and had $\ell_\varphi = 4$. At both resolutions, the transition from coalescence to sliding occurs over the range of capillary numbers from 0.08 to 0.1. At the higher resolution and $Ca = 0.09$, a bridge between the two drops is visible in the fourth frame of the sequence in Fig. 3.2. Such a bridge also forms and breaks at the lower resolution, but it breaks sooner and is not visible in the frames chosen for Fig. 3.2. These results show that doubling the resolution does not change the critical capillary number significantly. As will be described in "Droplet size effect," keeping the interface thickness constant at $\ell_\varphi = 2$ in simulations with $R = 37.5$ and $R = 75$ lowers the critical capillary number by almost a factor of three. Due to the absence of a significant change in the critical capillary number when doubling the resolution, the interface is judged to be adequately resolved with $\ell_\varphi = 2$. This choice for ℓ_φ agrees with the findings of van der Graaf and van der Sman[24, 25], who used this interface thickness because it provided the correct critical capillary number for droplet breakup in a shear flow. They found that the critical capillary number for breakup was too low with $\ell_\varphi = 1$. Since $\ell_\varphi = 2$ provides adequate resolution, all further simulations were

performed with this interface thickness. This choice allows us to simulate larger droplet sizes relative to the interface thickness with less computational resources.
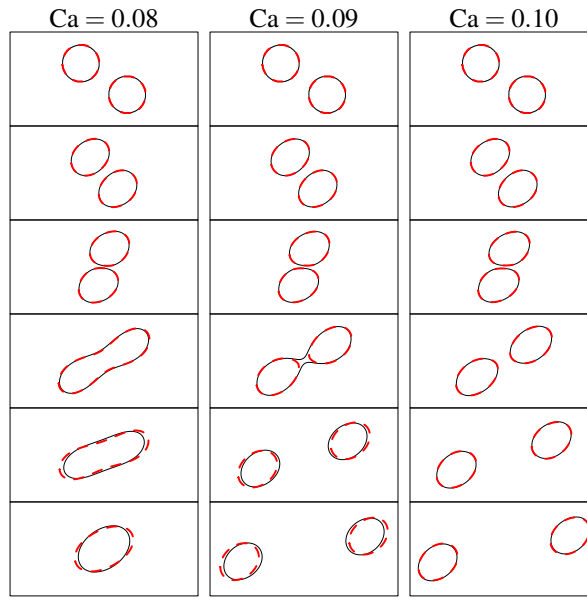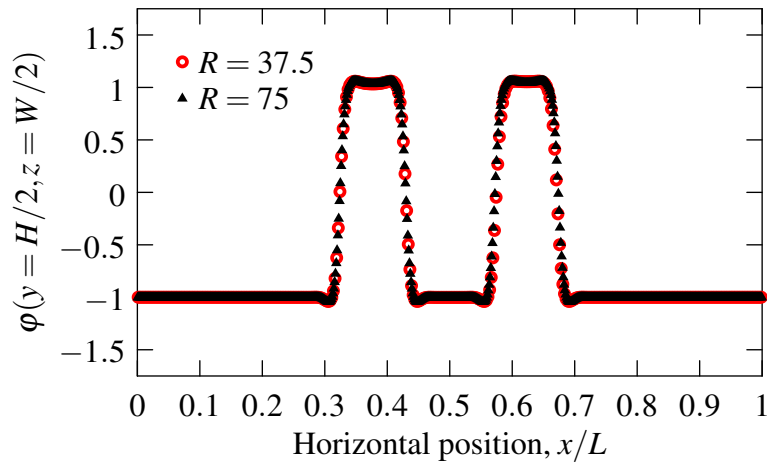
Figure 3.2: Effect of resolution on droplet collision simulations. The upper portion shows the value of φ along the x direction through the middle of the domain. Profiles are shown for the two resolutions ($R = 37.5$ and 75) at an early time when a smooth profile has been established but before significant shear has occurred ($\dot{\gamma}t = 0.13$). The profiles were visually identical for the three capillary numbers considered in the lower portion. The lower portion shows time series of the interface shape in cross-sections through the middle of the domain with $R = 37.5$ (dashed red) and $R = 75$ (solid black) at Ca $= 0.08$ (left), 0.09 (middle), and 0.1 (right). Time progresses from top ($\dot{\gamma}t = 0$) to bottom ($\dot{\gamma}t = 6.67$) in increments of $\dot{\gamma}t = 1.33$.

3.4.2 Domain size effect

Since the simulated domain is periodic in the two directions that are perpendicular to the height of the domain (i.e. the x and z axes in Fig. 3.1), we evaluated the effect of the domain size in these directions. The results for two domain sizes with $R = 37.5$ and $Ca = 0.08$, 0.09, and 0.10 were compared. The larger domain was $768 \times 192 \times 384$, which has twice the length and width of the smaller $384 \times 192 \times 192$ domain. Doubling these two dimensions did not change the shape of the droplets or the outcome of a collision at the three capillary numbers. A domain with $L \approx 10R$ and $W \approx 5R$ is therefore large enough that the effects of periodicity are minor. However, the effect of confinement, which is the ratio of the domain height and droplet diameter, is important, and this effect is discussed in the section "Confinement effect."

3.4.3 Droplet size effect

The effect of the droplet size on the outcome of a collision was studied by increasing the droplet radius and domain size in proportion while keeping the interface thickness (ℓ_φ, expressed as a number of lattice nodes) constant. This is in contrast to the simulations used to study the effects of the interface resolution (Fig. 3.2) in which the interface thickness was also scaled up by the same factor as the droplet radius and domain size. In the simulations used to study the effect of the droplet size, the Reynolds number, Péclet number, and geometry were kept constant at the previously-listed values. The simulations with different droplet sizes but the same interface thickness represent the physical situation of studying collisions of differently-sized droplets of the same pair of liquids. When the same liquid pair is used, the intermolecular interactions that determine the critical film thickness remain constant.

Figure 3.3 shows how the capillary number and the size of the droplet relative to the interface thickness determine the outcome of a collision. A bisection search method was used to find the critical values when the transitions between different outcomes occur. In general, droplets slide unless the capillary number is below a critical value. This critical capillary number decreases as the droplet becomes larger relative to the interface thickness, or equivalently, the interface thickness becomes smaller relative to the droplet radius. Considering previous discussion, this decreasing trend occurs because reducing the critical thickness for film rupture delays coalescence by increasing the time required for the film to drain. If the observed decreasing trend in the critical capillary number with increasing droplet size continues beyond the parameter range we studied, it is expected that droplets will not coalesce in the limit of a sharp interface, i.e. as $R/\ell_\varphi \to \infty$. Thus, to simulate a

physical system in which droplets coalesce, a finite $\frac{R}{\ell_\varphi}$ value is required.

As illustrated in Fig. 3.3, there are three possible outcomes of a simulated droplet collision for the parameter ranges that we consider. For every droplet size, there is a critical capillary number above which the droplets slide over each other and their interfaces remain distinct. There is also a critical capillary number below which the droplets coalesce. These two critical capillary numbers, however, are not necessarily the same.

The effect of the droplet size relative to the interface thickness $\left(\frac{R}{\ell_\varphi}\right)$ on the two critical capillary numbers is shown in Fig. 3.3. When $\frac{R}{\ell_\varphi} > 22$, there is only one critical capillary number that separates the regions of sliding and coalescence. When $\frac{R}{\ell_\varphi} < 22$ the situation is more complex. The higher critical capillary number specifies when the interfaces come close enough for the film to rupture. The newly-formed bridge is pulled apart by the shear flow. This happens until the capillary number falls below the lower critical capillary number that specifies when the outcome of a collision is coalescence. Both critical capillary numbers follow a simple scaling rule $\mathrm{Ca_c} \sim \left(\frac{R}{\ell_\varphi}\right)^{-n}$ with different values of n (with $n > 0$). Since n for the lower $\mathrm{Ca_c}$ is smaller than n for the higher $\mathrm{Ca_c}$, the two capillary numbers eventually become the same, and then the critical capillary number for film rupture becomes the critical value that determines if drops coalesce. This result is consistent with experiments[13] in which only one critical Ca for coalescence was observed. This suggests that the droplets in the experiments are sufficiently large that only one $\mathrm{Ca_c}$ exists. Experiments with smaller droplets are not available to verify if temporary bridges would be observed with smaller droplets.

To interpret the existence of a temporary bridge in simulations, we can compare the characteristic time scales of shear and bridge growth. The shear time scale is $\tau_s = \dot{\gamma}^{-1}$. The growth of the liquid bridge between drops is a complex phenomenon and only a brief discussion is presented here. There are two regimes for the growth of the bridge radius R_b over time (see e.g. Paulsen et al. [55]): a viscous and an inertial regime. Fig. 3.4 shows the growth of the bridge as a function of time for a simulation with $R = 37.5$, $\ell_\varphi = 2$, and $\frac{\sigma R}{\rho \nu^2} = 10.8$. The bridge radius R_b is proportional to the square root of time scaled by the inertial time scale $\tau_i = \sqrt{\frac{\rho R^3}{\sigma}}$, indicating that our binary-liquid simulations, like the liquid-vapour simulations by Lee and Fischer [56], are consistent with modelling for the inertial regime[57]. The proportionality factor of 0.7, however, is lower than the 1.2 found by Lee and Fischer [56]. An important difference between the modelling discussed here and the liquid-liquid coalescence experiments and simulations is that the modelling considers liquid drops in a vapour whose effects are often neglected. The slower growth of the bridge in liquid-liquid simulations may be due to the increased inertia of a liquid film compared
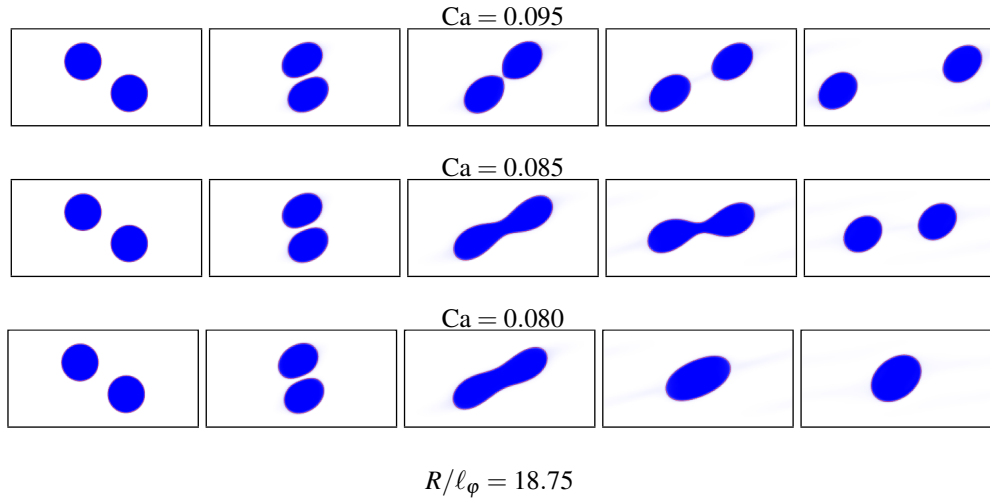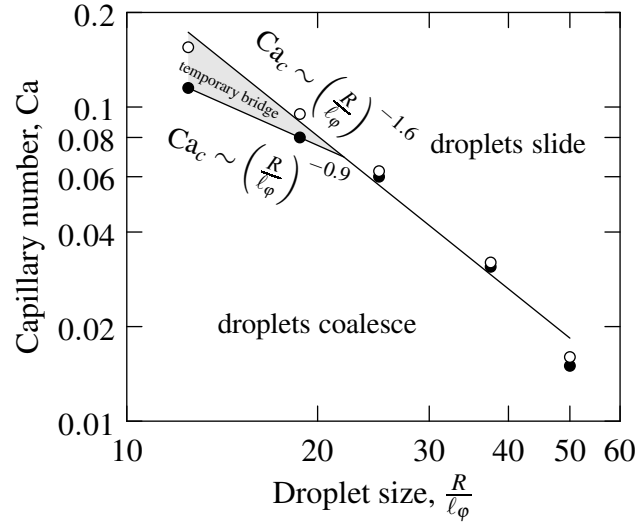
Figure 3.3: The effect of the droplet size (top) on the critical capillary numbers that separate the three possibilities (bottom) for the outcome of a simulated droplet collision. The open circles show the simulations with the lowest capillary number for a given droplet radius at which the two droplets remained separate. The filled circles show the highest capillary number at which the droplets coalesce. Solid lines show fitted scaling laws. The time sequences at the bottom show sample collisions with $R/\ell_\varphi = 18.75$ in which the droplets slide (top), a temporary bridge forms (middle), and the droplets coalesce (bottom). Cross-sections of the φ field are shown in the x-y plane through the middle of the domain with colours ranging from white ($\varphi = -1$) to blue ($\varphi = 1$). The $\varphi = 0$ contour is shown in red.

to a lower-density vapour film. Having shown that the inertial time scale determines the rate of bridge growth in the simulations, we can consider the ratio of the shear and inertial bridge growth time scales

$$\frac{\tau_s}{\tau_i} = \frac{\dot{\gamma}^{-1}}{\sqrt{\frac{\rho R^3}{\sigma}}} = \frac{1}{\sqrt{\mathrm{ReCa}}} \tag{3.20}$$

to determine the outcome of the competition between growth and shear that starts when the film ruptures and the bridge forms. When $\tau_s/\tau_i \ll 1$, the shear time scale is smaller than the bridge growth time scale, and we expect the slowly-growing bridge to be pulled apart; when $\tau_s/\tau_i \gg 1$, the bridge grows faster than shear pulls it apart, allowing the droplets to coalesce. A critical value of the ratio τ_s/τ_i must be exceeded for the droplets to coalesce. The value of this critical ratio may depend on various parameters. Based on the lower $\mathrm{Ca_c}$ values in Fig. 3.3, the critical value of τ_s/τ_i for the conditions of these simulations is slightly higher than 3. If this critical time scale ratio remains constant, the critical capillary number for bridge destruction scales as $\mathrm{Ca_c} \sim \mathrm{Re}^{-1}$ based on Eq. 3.20. At low Re, the dynamics switch to a viscous regime, and the Re^{-1} scaling is not applicable (by using the viscous time scale $\tau_v = \frac{\mu R}{\sigma}$ instead of τ_i, the time scale ratio Eq. 3.20 becomes the inverse of the capillary number and is therefore independent of Re). Thus in addition to the difference in droplet size relative to intermolecular length scales, the absence of experimental observations of a regime where a bridge forms and breaks may be also due to the difference in Reynolds numbers: the experiments of Chen et al. [13] had $\mathrm{Re} < 1 \times 10^{-7}$ compared with $\mathrm{Re} = 1$ in the simulations.
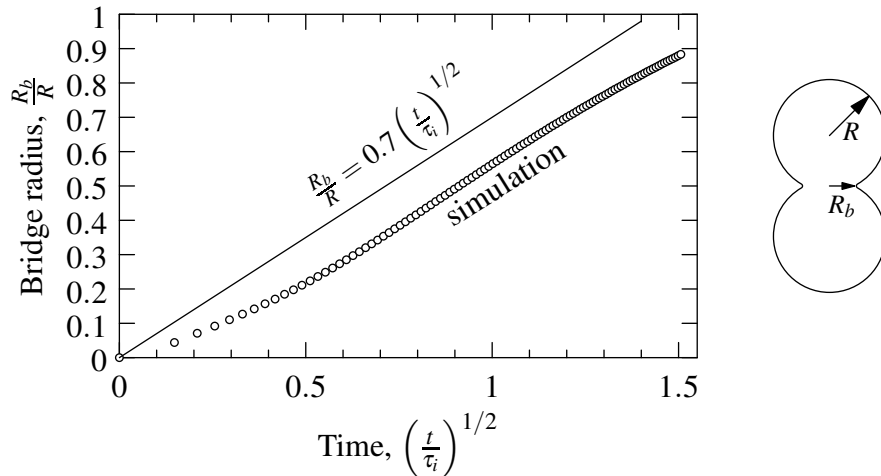
Figure 3.4: The radius of the bridge between two initially separate droplets in a simulation, which is illustrated on the right, grows with the square root of time scaled by the inertial time scale τ_i. The solid line shows the slope estimated at $t = \tau_i$.

3.4.4 Interface diffusivity effect

The chemical potential diffusivity, or mobility M (defined in Eq. 3.13), affects the critical capillary number for coalescence. Qualitatively, if the diffusivity is low, the φ profile over an interface responds slowly to changes in local conditions. As diffusion speeds up compared to advection, the interaction time between two interfaces that is required for sufficient diffusion to cause film rupture decreases. The critical capillary number increases, i.e. coalescence becomes "easier," as the mobility increases (Pe decreases).

Previous studies of the effect of the interface diffusivity in multiphase flow simulations with the free-energy method have not considered coalescence. Van der Graaf et al.[24] performed three-dimensional simulations of droplet formation in a microfluidic T-junction. They verified that the critical capillary number for droplet breakup in a simple shear flow was correct for their choice of resolution and Péclet number. Van der Sman and van der Graaf[25] systematically studied droplet deformation and breakup in two-dimensional simulations with the free-energy method. Yue and Feng [58] discuss diffuse-interface modelling of contact line motion on solid surfaces, a problem with features that are relevant to simulations of coalescence. In the limit of a sharp interface (a non-diffusing interface with zero thickness), contact lines remain unphysically pinned. The sharp-interface limit is also unphysical for simulations of coalescence. Reducing the interface thickness relative to the droplet size delays coalescence because the thickness of the film between the drops must thin to a greater extent before coalescence, as was shown in the section "Droplet size effect". Zero diffusivity is also undesirable because, in the absence of diffusivity, adjacent interfaces would not merge to cause coalescence. In simulations of contact line motion, the limit of zero thickness and non-zero diffusivity is desired[58], while both a non-zero interface thickness and diffusivity (and therefore a finite Péclet number) are required for coalescence. In fact, van der Sman and van der Graaf [25] found that the critical capillary number for droplet breakup in shear is correct when the rates of interface advection and diffusion balance, i.e. the Péclet number is near one. In three-dimensional simulations, van der Graaf et al. [24] obtained the correct critical capillary number for breakup in shear with Pe = 10. Droplet breakup and coalescence, however, involve topologically and hydrodynamically different interactions between two interfaces. As a result, the correct choice of the Péclet number for simulations of breakup and coalescence may not be the same. We therefore study the effect of the Péclet number on coalescence in this section. In the other sections, Pe = 10 was used.

The effect of the Péclet number on the collision outcome map (Fig. 3.3) is shown in Fig. 3.5. All dimensionless parameters were kept constant except the interface Péclet num-

ber that was varied between 1 and 100. Numerical instability prevented simulations with $Pe = 100$ and $R/\ell_\varphi > 25$. In general, as the Péclet number decreases, the critical capillary numbers increase and the area of the region where temporary bridges form increases. The critical capillary numbers as a function of the Péclet number for $R/\ell_\varphi = 18.75$ are also shown in Fig. 3.5. As expected, increasing the Péclet number lowers Ca_c. Compared to the effect of R/ℓ_φ on Ca_c, the effect of the Péclet number is weaker: Ca_c decreases by a factor of four as the Péclet number increases by a factor of 100, while doubling R/ℓ_φ reduces Ca_c by a factor of three. In the advection dominated region with $Pe > 50$, a temporary bridge does not form, and both Ca_c values become constant at about 0.05. As the Péclet number decreases, both critical capillary numbers increase and the difference between them also increases. If both breakup and coalescence can be simulated correctly with the same Péclet number, the results with $Pe = 10$ (with which van der Graaf et al. [24] obtained breakup at the correct capillary number) may be considered predictive. A region of temporary bridge formation is thus expected to exist in experiments, but experimental evidence is not presently available to assess this prediction. The existence and size of the parameter range for temporary bridge formation is highly sensitive to the Péclet number.
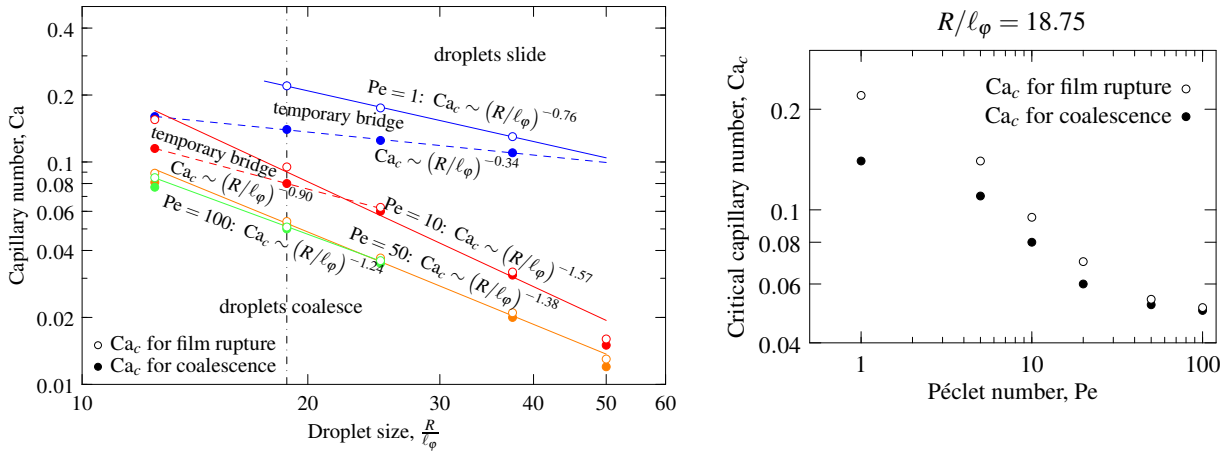
Figure 3.5: Effect of the Péclet number on the collision outcome map (left). The results for Péclet numbers of 1 (blue), 10 (red), 50 (orange) and 100 (green) are shown. The solid and dashed lines show fitted scaling laws. The dashed lines are for the high Ca at which the droplets remain coalesced; the solid lines are for the lowest Ca at which the droplets slide. At capillary numbers between these lines, a bridge forms then breaks. The effect of the Péclet number on the two critical capillary numbers at a constant droplet size of $R/\ell_\varphi = 18.75$, indicated by the vertical dash-dotted line on the left, is shown on the right.

56

3.4.5 Offset effect

To study the effect of the vertical offset, we performed additional simulations with a lower offset ΔY between the droplets. Simulations with capillary numbers exceeding 0.2 were not performed because the deformation of the droplets became significant, and the periodicity of the domain began to influence the outcome of the simulations. The non-dimensional vertical offset for the second set of simulations was 0.6. All other parameters were kept constant. The results of these simulations are compared with the previous simulations with an offset of 0.86 in Fig. 3.6. As the vertical offset decreases, the geometry approaches that of a head-on collision, and the Ca_c for coalescence increases. Simulations with $R = 100$ were also performed at $\frac{\Delta Y}{2R} = 0.3$ and 0.4. Results for $\frac{\Delta Y}{2R} = 0.4$ are shown in Fig. 3.7. At these offsets, critical capillary numbers between 0.1 and 0.25 are expected. Precise values were not obtained due to the computational requirements of the large domains. At these lower offsets, the droplets switch to coalescing in the compression stage (i.e. before sliding over each other) rather than the extension stage (when they move apart after sliding over). Comparing Figs. 3.3 and 3.7, the change in the critical capillary numbers and the relative orientation at coalescence (compression versus extension) can be seen. Complex behaviour is seen at Ca = 0.15. An internal droplet is present in the bridge and multiple drops form when the bridge breaks. Simulations at low offsets will be studied in greater detail in the future. Significantly larger droplets (and therefore simulation domains) are needed to determine the critical capillary number at the vertical offset of 0.16 for the droplets in the experiments of Chen et al[13].

3.4.6 Confinement effect

The effect of confinement was studied using simulations with the same range of radii as previously but in a domain with a constant size. In Fig. 3.8, the results of these simulations with a fixed domain size of $1024 \times 256 \times 256$ are compared to the previous simulations that had a constant confinement. Numerical instability prevented the completion of simulations at $\frac{2R}{H} = 0.29$ with Ca < 0.008. The critical capillary number is therefore not known for this confinement, but must be below 0.008. The open circle indicates this lowest capillary number that could be simulated. Comparing with the constant high-confinement $\left(\frac{2R}{H} = 0.39\right)$ simulations, reducing the confinement first decreases the critical capillary numbers, then increases them until they eventually exceed those for the highly-confined case. The reason for the reduction in the critical capillary numbers at $\frac{R}{\ell_\varphi} = 25$ is illustrated in Fig. 3.8. In the larger domain, the droplets are more free to move vertically and slide over each other. As a result, a lower shear rate (and therefore Ca) is needed to prevent sliding and cause
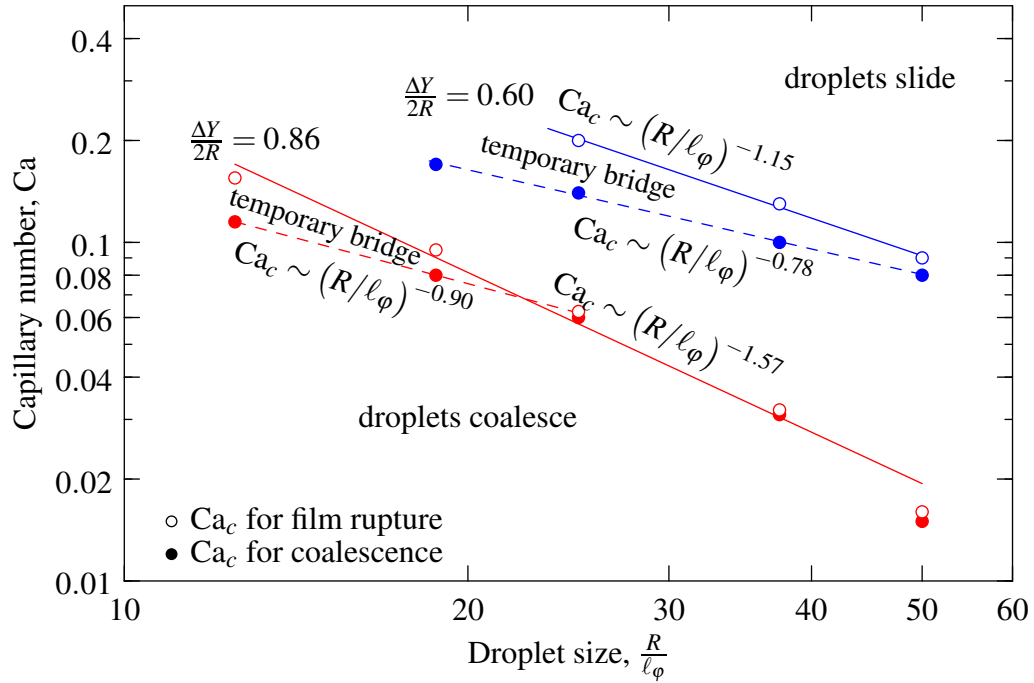
Figure 3.6: Effect of the vertical offset on the critical capillary numbers for coalescence. The red lines are for an offset of 0.86; the blue lines are for 0.60. A temporary bridge forms for capillary numbers between the open and filled symbols.
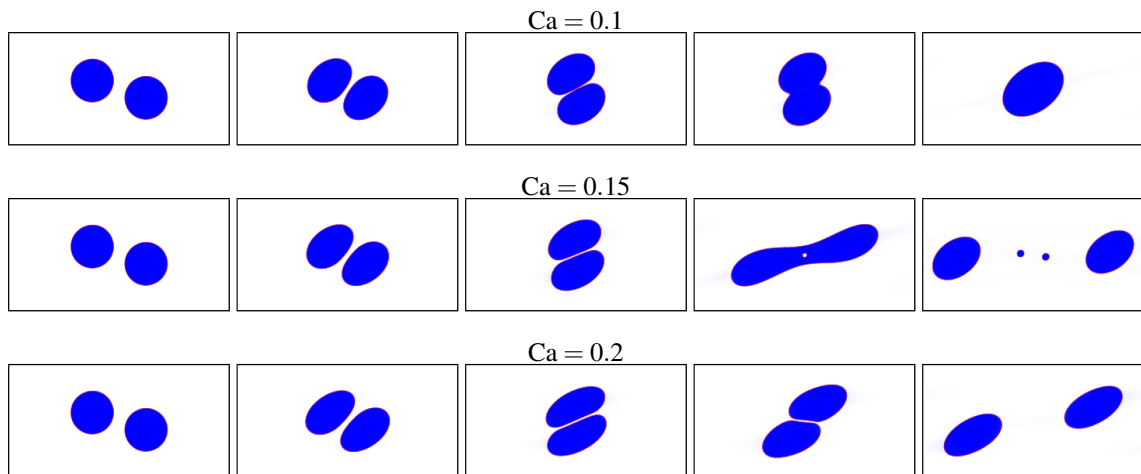
Figure 3.7: Sample collisions between droplets with $\frac{\Delta Y}{2R} = 0.4$ and $\frac{R}{\ell_\varphi} = 50$. The time increments are not uniform, differ between the three cases, and were chosen to illustrate the different stages of the collisions well.

coalescence.
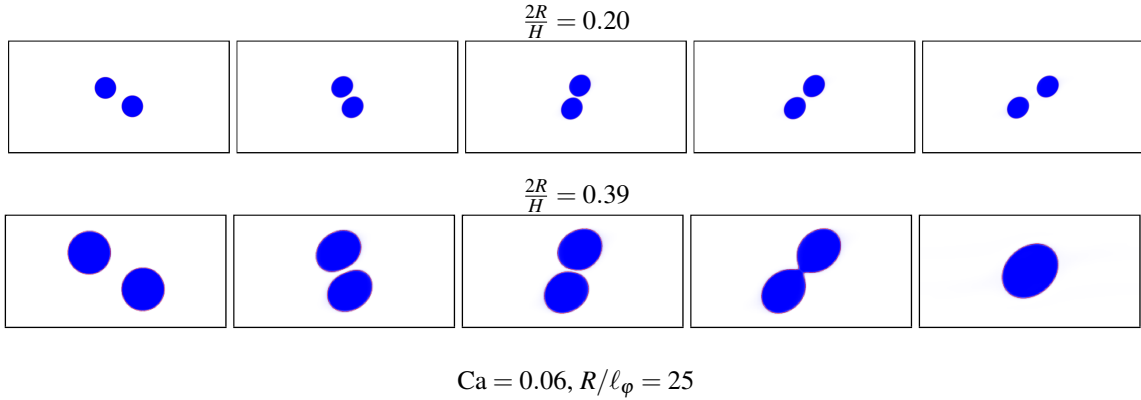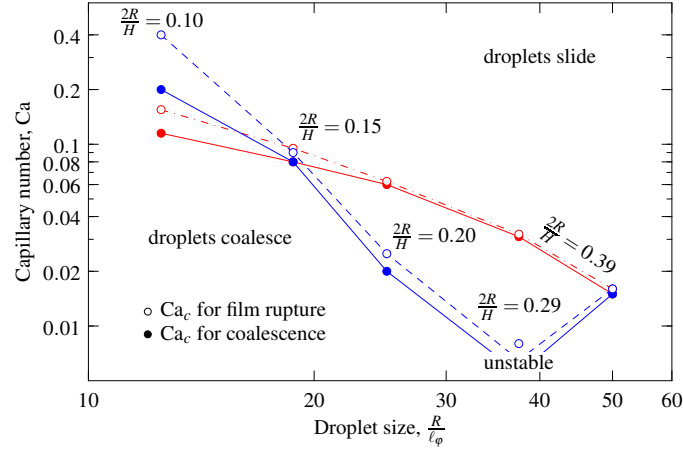
Figure 3.8: (top) Effect of confinement on the critical capillary numbers for coalescence. The red lines are for a constant confinement $\frac{2R}{H} = 0.39$. The blue lines are for a constant domain size and varying droplet sizes (and therefore confinements). (bottom) Sample collisions between droplets with confinements of $\frac{2R}{H} = 0.20$ (upper sequence) and 0.39 (lower sequence) and the same capillary number (Ca = 0.06) and droplet size ($R/\ell_\varphi = 25$). The images have been scaled so that the domains are the same size; the domain for $\frac{2R}{H} = 0.20$ is double the size of the domain for $\frac{2R}{H} = 0.39$.

3.5 Comparison with experimental results

While detailed experimental results are available for droplet coalescence in the extensional flow of a four-roll mill[9–12], few experimental results are available for simple shear flow. Early work by Guido and Simeone[8] did not determine critical capillary numbers. Recently, Chen et al. [13] reported critical capillary number ranges for confined and unconfined droplets in simple shear. Though these results are the most relevant to our simulations,

they cannot be compared quantitatively. Considering the increasing trend in the critical capillary number with decreasing droplet size, the high critical values for the simulations indicate that the effective physical sizes of the simulated droplets are smaller than those used in the experiments (radii 50 to 150 μm). Furthermore, the vertical offsets produced by breaking a drop are lower (0.16) than the lowest offset for which critical capillary numbers could be estimated in the simulations (0.3). Chen et al. [13] also present results for effectively unconfined droplets and droplets with varying confinement, while simulations with constant high confinement are most practical to obtain from simulations. Finally, the small difference in horizontal offset likely has a minor effect, while the difference in Reynolds number (1 in simulations vs. 10^{-7} in experiments) may be important. This Reynolds number is based on the droplet radius, and a Reynolds number based on the film thickness would be one to two orders of magnitude smaller in the simulations. The flow in the draining film is therefore likely in the Stokes regime for both the simulations and experiments. Due to the differences in the parameters between the simulations and experiments, we can only compare the results qualitatively. The simulation results are nonetheless useful because they indicate how different numerical parameters affect the critical capillary number and therefore how experiments and simulations can be matched by choosing the parameters correctly.

One key difference between the simulations and the experiments of Chen et al. [13] is the stage of the collision process in which coalescence occurs. Chen et al. obtained critical capillary numbers between 0.001 and 0.008 and always saw coalescence during the compression stage of the collision when the shear flow pushes the droplets together. In contrast, Guido and Simeone[8] observed coalescence during extension at Ca $= 0.13$, but with a viscosity ratio of 0.36 (droplet phase over continuous phase; the ratio is 1.1 for the experiments by Chen et al. [13] and 1 in the LBM simulations). The coalescence of droplets in the extension stage of the simulations is likely due to the high capillary numbers at which the droplets coalesce and the large vertical offset.

To understand the differences in fluid and interface parameters between the experiments and simulations better, we re-visit the bridge growth phenomenon. By differentiating the equation describing the growth rate of the bridge, $\frac{R_b}{R} = 0.7 \left(t \sqrt{\frac{\sigma}{\rho R^3}} \right)^{1/2}$, a Reynolds number Re$_b$ that characterizes the speed of the interface can be defined. Taking the growth rate of the bridge radius R_b at time $t = \tau_i$ as the characteristic speed and the droplet radius as the characteristic length, this Reynolds number is

$$\mathrm{Re}_b \equiv \frac{R}{\nu} \frac{\mathrm{d}R_b}{\mathrm{d}t}\bigg|_{t=\tau_i} = \frac{1}{2}\sqrt{\frac{\sigma R}{\rho \nu^2}} \tag{3.21}$$

The proportionality factor of order one has been omitted. In the limit of high Re_b, the momentum generated at the growing bridge cannot diffuse over the radius of the droplet in the time it takes the bridge to grow. If Re_b is low, momentum diffusion is fast, and the inertial growth model is invalid. This Reynolds number is related to the non-dimensional quantity $\frac{\sigma R}{\rho v^2}$, called the Suratman number Su[59]. With this definition of Su, $\text{Re}_b = \frac{1}{2}\sqrt{\text{Su}}$. For the shear flow simulations, $\text{Su} = \frac{\text{Re}}{\text{Ca}}$ and is between 5 and 100. In contrast, $\frac{\sigma R}{\rho v^2} \approx 10^{-6}$ for the experiments by Chen et al. [13] due to the high viscosity of the polymers they used. The growth of bridges between their polymer droplets is therefore not in the inertial regime, but rather in the viscous regime. If experiments are possible with a fluid pair that has a viscosity similar to water, the results could be compared with the simulations. Using $\sigma = 2\,\text{mN/m}$, $\rho = 1000\,\text{kg/m}^3$, $R = 10\,\mu\text{m}$, and $v = 10^{-6}\,\text{m}^2\text{/s}$, the value of $\frac{\sigma R}{\rho v^2}$ is 20, which is within the range that is feasible for simulations. While the difference in Suratman number between the experiments and simulations clearly affects the post-coalescence growth of the bridge, its effect on the pre-coalescence shape and trajectory of the droplets remains to be studied in greater detail.

In both experiments and simulations, the critical capillary number decreases as the droplet size increases. Due to the differences in parameters between the simulations and experiments, comparing the rate of the decrease is difficult. For reference, the experimental data of Chen et al. [13] for unconfined droplets are provided in Fig. 3.9. The experimental data do not follow a simple power law scaling, but the slope for simulations with $\text{Pe} = 10$ is shown for comparison. The exponent was determined for simulations at a constant confinement of 0.39, while the experimental results are for unconfined droplets ($2R/H < 0.1$). Considering Figs. 3.5 and 3.8, the rate of decrease is higher for low confinement and increases with increasing Péclet number. The apparent agreement between the exponent for unconfined experimental droplets and the confined droplet simulations at $\text{Pe} = 10$ is likely coincidental. Further experiments or simulations at matching parameters are required to evaluate the results. Due to the effect of the Péclet number on the exponent in the scaling law, the correct Péclet number for simulations could be determined by matching the exponent to experimental data.

It is worth noting that experimental results and scaling laws for the effect of the droplet size on the capillary number are presented by showing the capillary number (a dimensionless quantity) as a function of the droplet radius (a dimensional quantity)[9–13]. Ideally, one would non-dimensionalize the droplet size by an appropriate physical length scale, but the correct choice is not clear. If simulations and experiments with equal values for all dimensionless parameters were feasible, it would be possible to determine the effective physical length that corresponds to the interface thickness ℓ_φ in simulations. This length,

however, would likely not be universal and would depend on the specific liquid pair being considered.

As the vertical offset is decreased from 0.86 to 0.3 in the simulations, the critical capillary numbers increase by about one order of magnitude. The collision stage in which the droplets coalesce changes from being the extension stage at high offsets to the compression stage at low offsets. Coalescence during compression at low offsets and extension at high offsets is qualitatively consistent with the observations of Yoon et al. [12] for extensional flows.

The trend in the critical capillary numbers for constant domain size qualitatively matches the experimental results of Chen et al. [13]. Chen et al. found that the critical capillary number decreases monotonically as the droplet size increases in a fixed domain height when the confinement is low (< 0.2). The critical capillary number then rises once the confinement exceeds 0.2. In the simulations, a decrease in the critical capillary number was seen until a confinement of about 0.3, after which the critical capillary number increases.
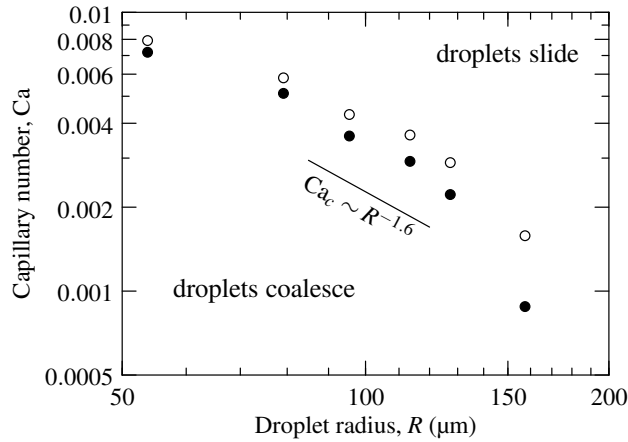
Figure 3.9: Experimental data of Chen et al.[13] for unconfined droplets in simple shear flow. The open symbols show the lowest capillary number at which the droplets slide; the filled symbols show the highest capillary number at which they coalesce.

3.6 Conclusions

Highly-resolved, three-dimensional simulations of equal-size liquid droplets colliding in the simple shear flow of another liquid were performed using the free-energy lattice Boltzmann method. In such a shear flow, the droplets coalesce unless a critical capillary number is exceeded. While the droplets in previous simulations were too small to determine the critical capillary number, we used a highly-parallel code to simulate sufficiently large

domains. With these large-scale simulations, we determined the critical capillary number and explained why droplets coalesced at unrealistically high capillary numbers in previous simulations. The most important factor that determines the critical capillary number in the simulations is the relative size of the droplets with respect to the thickness of the diffuse interface. The critical capillary number decreases as the size of the droplets increases. When the droplet radius is 25 lattice nodes and the characteristic thickness of the interface is 2, which are typical values for droplet simulations, the critical capillary number is 0.16. Our largest simulations had droplets with radii of 100 lattice nodes; with these large droplets, the critical capillary number was 0.016. The interface diffusivity, expressed as a Péclet number, also affects the critical capillary number. With faster diffusion (lower Péclet number), droplets coalesce at higher capillary numbers. A parameter range was found where small droplets temporarily coalesce until shear pulls the newly-formed droplet apart. Two geometric parameters, the vertical offset and confinement, were also considered. As the vertical offset between the droplets is decreased, the critical capillary number increases and the time of coalescence switches from the extension stage to the compression stage of the collision. If the domain size is kept constant and the droplet size is increased (thereby increasing the confinement), the critical capillary number first decreases then increases, as in experiments.

The results of the simulations appear to be physically reasonable. However, simulations at the scale required to match experimental work reported in the literature remain computationally impractical. If experiments were instead performed with smaller droplets and less viscous fluids than the previously-used polymers, a direct comparison with simulations may now be possible due to the feasibility of sufficiently large-scale simulations. For such a direct comparison, we estimate that 1 to 50μm diameter droplets are required together with a fluid for which $\frac{\sigma R}{\rho v^2} \approx 20$. This value could be achieved with a fluid whose viscosity is approximately that of water. Such experiments are needed to determine the interface thickness and diffusivity (Péclet number) that should be used in simulations to correctly model physical systems. Experiments and simulations at matched conditions would also reveal the physical length scale that corresponds to the numerical interface thickness. Future work will involve simulations of larger droplets relative to the interface thickness and lower offsets to further explore the parameter space. The results presented in this chapter are not only relevant to free-energy LBM simulations and likely also apply to simulations with other phase-field Cahn-Hilliard methods, such as those of Ceniceros et al. [60]

References

[1] C. Tsouris and L.L. Tavlarides. Breakage and coalescence models for drops in turbulent dispersions. *AIChE J.*, 40:395–406, 1994.

[2] M. Kostoglou and A.J. Karabelas. A contribution towards predicting the evolution of droplet size distribution in flowing dilute liquid/liquid dispersions. *Chem. Eng. Sci.*, 56:4283–4292, 2001.

[3] F. Laurenzi, M. Coroneo, G. Montante, A. Paglianti, and F. Magelli. Experimental and computational analysis of immiscible liquid-liquid dispersions in stirred vessels. *Chem. Eng. Res. Des.*, 87:507–514, 2009.

[4] S.-Y. Teh, R. Lin, L.-H. Hung, and A.P. Lee. Droplet microfluidics. *Lab Chip*, 8: 198–220, 2008.

[5] C.N. Baroud, F. Gallaire, and R. Dangla. Dynamics of microfluidic droplets. *Lab Chip*, 10:2032–2045, 2010.

[6] N. Bremond and J. Bibette. Exploring emulsion science with microfluidics. *Soft Matter*, 8:10549–10559, 2012.

[7] N. Bremond, A.R. Thiam, and J. Bibette. Decompressing emulsion droplets favors coalescence. *Phys. Rev. Lett.*, 100:024501, 2008.

[8] S. Guido and M. Simeone. Binary collision of drops in simple shear flow by computer-assisted video optical microscopy. *J. Fluid Mech.*, 357:1–20, 1998.

[9] Y.T. Hu, D.J. Pine, and L.G. Leal. Drop deformation, breakup, and coalescence with compatibilizer. *Phys. Fluids*, 12:484–489, 2000.

[10] H. Yang, C.C. Park, Y.T. Hu, and L.G. Leal. The coalescence of two equal-sized drops in a two-dimensional linear flow. *Phys. Fluids*, 13:1087–1106, 2001.

[11] L.G Leal. Flow induced coalescence of drops in a viscous fluid. *Phys. Fluids*, 16: 1833–1851, 2004.

[12] Y. Yoon, M. Borrell, C.C. Park, and L.G. Leal. Viscosity ratio effects on the coalescence of two equal-sized drops in a two-dimensional linear flow. *J. Fluid Mech.*, 525: 355–379, 2005.

[13] D. Chen, R. Cardinaels, and P. Moldenaers. Effect of confinement on droplet coalescence in shear flow. *Langmuir*, 25:12885–12893, 2009.

[14] A.K. Chesters. The modelling of coalescence processes in fluid-liquid dispersions: A review of current understanding. *Chem. Eng. Res. Des.*, 69:259–270, 1991.

[15] V. Cristini and Y.-C. Tan. Theory and numerical simulation of droplet dynamics in complex flows — a review. *Lab Chip*, 4:257–264, 2004.

[16] M. Loewenberg and E.J. Hinch. Collision of two deformable drops in shear flow. *J. Fluid Mech.*, 338:299–315, 1997.

[17] A.Z. Zinchenko and R.H. Davis. Shear flow of highly concentrated emulsions of deformable drops by numerical simulations. *J. Fluid Mech.*, 455:21–62, 2002.

[18] A.Z. Zinchenko and R.H. Davis. Large-scale simulations of concentrated emulsion flows. *Phil. Trans. R. Soc. Lond. A*, 361:813–845, 2003.

[19] R.H. Davis and A.Z. Zinchenko. Motion of deformable drops through granular media and other confined geometries. *J. Colloid Interf. Sci.*, 334:113–123, 2009.

[20] G. Tryggvason, R. Scardovelli, and S. Zaleski. *Direct Numerical Simulations of Gas-Liquid Multiphase Flows*. Cambridge University Press, 2011.

[21] S. Zaleski, J. Li, and S. Succi. Two-dimensional Navier-Stokes simulation of deformation and breakup of liquid patches. *Phys. Rev. Lett.*, 72:244–247, 1995.

[22] J. Zhang. Lattice Boltzmann method for microfluidics: models and applications. *Microfluid Nanofluid*, 10:1–28, 2011.

[23] A.J. Briant and J.M. Yeomans. Lattice Boltzmann simulations of contact line motion. II. Binary fluids. *Phys. Rev. E*, 69:031603, 2004.

[24] S. van der Graaf, T. Nisisako, C.G.P.H. Schroën, R.G.M. van der Sman, and R.M. Boom. Lattice Boltzmann simulations of droplet formation in a T-shaped microchannel. *Langmuir*, 22:4144–4152, 2006.

[25] R.G.M. van der Sman and S. van der Graaf. Emulsion droplet deformation and breakup with lattice Boltzmann model. *Comput. Phys. Commun.*, 178:492–504, 2008.

[26] X. Jia, J. B. McLaughlin, and K. Kontomaris. Lattice Boltzmann simulations of flows with fluid-fluid interfaces. *Asia-Pac. J. Chem. Eng.*, 3:124–143, 2008.

[27] G.F. Christopher, J. Bergstein, N.B. End, M. Poon, C. Nguyen, and S.L. Anna. Coalescence and splitting of confined droplets at microfluidic junctions. *Lab Chip*, 9: 1102–1109, 2009.

[28] D. L. Chen, L. Li, S. Reyes, D.N. Adamson, and R.F. Ismagilov. Using three-phase flow of immiscible liquids to prevent coalescence of droplets in microfluidic channels: Criteria to identify the third liquid and validation with protein crystallization. *Langmuir*, 23:2255–2260, 2007.

[29] H. Farhat and J.S. Lee. Suppressing the coalescence in the multi-component lattice Boltzmann method. *Microfluid Nanofluid*, 11:137–143, 2010.

[30] T.J. Spencer, I. Halliday, and C.M. Care. A local lattice Boltzmann method for multiple immiscible fluids and dense suspensions of drops. *Phil. Trans. R. Soc. Lond. A*, 369:2255–2263, 2011.

[31] P. Yue, J.J. Feng, C. Liu, and J. Shen. Diffuse-interface simulations of drop coalescence and retraction in viscoelastic fluids. *J. Non-Newtonian Fluid Mech.*, 129: 163–176, 2005.

[32] P.M. Dupuy, M. Fernandino, H.A. Jakobsen, and H.F. Svendsen. Using Cahn-Hilliard mobility to simulate coalescence dynamics. *Computers and Mathematics with Applications*, 59:2246–2259, 2010.

[33] K.N. Premnath and J. Abraham. Lattice Boltzmann simulations of drop-drop interactions in two-phase flows. *Int. J. Mod. Phys. C*, 16:25–44, 2005.

[34] K.N. Premnath and J. Abraham. Simulations of binary drop collisions with a multiple-relaxation-time lattice-Boltzmann model. *Phys. Fluids*, 17:122105, 2005.

[35] T. Inamuro, T. Ogata, S. Tajima, and N Konishi. A lattice Boltzmann method for incompressible two-phase flows with large density differences. *J. Comput. Phys.*, 198:628–644, 2004.

[36] T. Lee and C.-L. Lin. A stable discretization of the lattice Boltzmann equation for simulation of incompressible two-phase flows at high density ratio. *J. Comput. Phys.*, 206:16–47, 2005.

[37] K. Sun, M. Jia, and T. Wang. Numerical investigation of head-on droplet collision with lattice Boltzmann method. *Int. J. Heat and Mass Transfer*, 58:260–275, 2013.

[38] D. Chiappini, G. Bella, S. Succi, and S. Ubertini. Applications of finite-difference lattice Boltzmann method to breakup and coalescence in multiphase flows. *Int. J. Mod. Phys. C*, 20:1803–1816, 2009.

[39] D. Lycett-Brown, I. Karlin, and K.H. Luo. Droplet collision simulation by a multi-speed lattice Boltzmann method. *Commun. Comput. Phys.*, 9:1219–1234, 2011.

[40] X. Shan and H. Chen. Lattice Boltzmann model for simulating flows with multiple phases and components. *Physical Review E*, 47:1815–1820, 1993.

[41] P. Perlekar, L. Biferale, M. Sbragaglia, S. Srivastava, and F. Toschi. Droplet size distribution in homogeneous isotropic turbulence. *Phys. Fluids*, 24:065101, 2012.

[42] A. Gunstensen, D. Rothman, S. Zaleski, and G. Zanetti. Lattice Boltzmann model of immiscible fluids. *Phys. Rev. A*, 43:4320–4327, 1991.

[43] M. Latva-Kokko and D.H. Rothman. Diffusion properties of gradient-based lattice Boltzmann models of immiscible fluids. *Phys. Rev. E*, 71:056702, 2005.

[44] H. Liu, A.J. Valocchi, and Q. Kang. Three-dimensional lattice boltzmann model for immiscible two-phase flow simulations. *Phys. Rev. E*, 85:046309, 2012.

[45] L. Wu, M. Tsutahara, L.S. Kim, and M.Y. Ha. Three-dimensional lattice Boltzmann simulations of droplet formation in a cross-junction microchannel. *Int. J. Multiphase Flow*, 34:852–864, 2008.

[46] H. Liu and Y. Zhang. Droplet formation in microfluidic cross-junctions. *Phys. Fluids*, 23:082101, 2011.

[47] R. Benzi, S. Succi, and M. Vergassola. The lattice Boltzmann equation: Theory and applications. *Phys. Rep.*, 222:145–197, 1992.

[48] S. Chen and G.D. Doolen. Lattice Boltzmann method for fluid flows. *Annu. Rev. Fluid Mech.*, 30:329–364, 1998.

[49] C.K. Aidun and J.R. Clausen. Lattice-Boltzmann method for complex flows. *Annu. Rev. Fluid Mech.*, 42:439–472, 2010.

[50] G. Falcucci, S. Ubertini, C. Biscarini, S. Di Francesco, D. Chiappini, S. Palpacelli, A. De Maio, and S. Succi. Lattice Boltzmann methods for multiphase flow simulations across scales. *Commun. Comput. Phys.*, 9:269–296, 2011.

[51] C.M. Pooley and K. Furtado. Eliminating spurious velocities in the free-energy lattice Boltzmann method. *Phys. Rev. E*, 77:046702, 2008.

[52] O. Shardt, J.J. Derksen, and S.K. Mitra. Simulations of droplet collisions in shear flow. In *Proceedings of the ASME 2012 International Mechanical Engineering Congress & Exposition*, 2012.

[53] A.J.C. Ladd. Numerical simulations of particulate suspensions via a discretized Boltzmann equation. part 1. theoretical foundation. *J. Fluid Mech.*, 271:285–309, 1994.

[54] Q. Zou and X. He. On pressure and velocity boundary conditions for the lattice Boltzmann BGK model. *Phys. Fluids*, 9:1591–1598, 1997.

[55] J.D. Paulsen, J.C. Burton, and S.R. Nagel. Viscous to inertial crossover in liquid drop coalescence. *Phys. Rev. Lett.*, 106:114501, 2011.

[56] T. Lee and P.F. Fischer. Eliminating parasitic currents in the lattice Boltzmann equation method for nonideal gases. *Phys. Rev. E*, 74:046709, 2006.

[57] L. Duchemin, J. Eggers, and C. Josserand. Inviscid coalescence of drops. *J. Fluid Mech.*, 487:167–178, 2003.

[58] P. Yue and J.J. Feng. Can diffuse-interface models quantitatively describe moving contact lines? *Eur. Phys. J. Special Topics*, 197:37–46, 2011.

[59] W. Yao, H.J. Maris, P. Pennington, and G.M. Seidel. Coalescence of viscous liquid drops. *Phys. Rev. E*, 71:016309, 2005.

[60] H.D. Ceniceros, R.L. Nós, and A.M. Roma. Three-dimensional, fully adaptive simulations of phase-field fluid models. *J. Comp. Phys.*, 229:6135–6155, 2010.

The critical conditions for coalescence in phase field simulations of colliding droplets in shear[1]

4.1 Introduction

Phase field models for computing multiphase flows describe interface motion and deformation in a way that conveniently handles the topological changes of breakup and coalescence. These methods have been used to study the deformation and breakup of droplets in simple shear[1, 2] and microfluidic junctions[3] as well as the motion of three phase contact lines[4–7]. In fact, simulations of contact line motion with the Cahn-Hilliard[8] model have matched molecular dynamics simulations[5, 9]. While these interfacial flow phenomena have been studied in detail with phase field methods, the interactions between interfaces that lead to coalescence have received comparatively little attention. A key reason is the need for high resolution: the colliding droplets in simulations of coalescence must be significantly larger than the films that can form between them. The difficulty of achieving sufficient resolution led to the observation that coalescence was too easy in simulations[10] and methods with suppressed coalescence were developed[11, 12]. While models with suppressed coalescence are useful for studying flows where coalescence does not occur, they cannot be used to study the transition to coalescence. The ability to perform simulations with accurate predictions of the conditions for coalescence would be useful in a wide variety of applications. Examples include droplet collisions in shear, confined droplet flows in microchannels[13], and situations where breakup and coalescence must both be modelled correctly, such as the droplet size distributions of falling raindrops[14] and emulsions in turbulence[15, 16]. Consequently, there is a need to understand the conditions for and dy-

---

[1]A version of this chapter will be submitted to a journal.

namics of coalescence in phase field simulations of fluid mixtures to assess their ability to describe coalescence phenomena. Due to its physical foundations and success in describing other flow phenomena, the Cahn-Hilliard model is the focus of this work. We perform simulations of droplet collisions in confined simple shear flow, a flow configuration in which the critical conditions for coalescence have been studied experimentally[17, 18].

Simulations of colliding droplets in shear were first performed by Loewenberg and Hinch [19] using a boundary integral method and preceded the experimental work of Guido and Simeone [20], who found agreement with the simulations. These experiments did not provide the critical conditions for coalescence, but revealed the trajectories and deformation of drops during collisions at different conditions. A sample experimental trajectory was reproduced in simulations by Cristini et al. [21]. Earlier experiments by Bartok and Mason [22] and Allan and Mason [23] showed that deformation of the drops was needed for their separation in the velocity gradient direction to increase during a collision. The critical conditions for coalescence in primarily extensional linear shear flows were studied by Yang et al. [24] and the effect of the viscosity ratio was determined[25]. Mousa et al. [26] studied the coalescence efficiency of droplets in simple shear flow, and recently the critical conditions for coalescence in confined simple shear flow were determined[17, 18]. In these and previous experimental studies, flow inertia has been negligible. Simulations with a front-tracking finite difference method have examined the effects of finite inertia, confinement, and viscosity ratio[27–29].

While the purpose of these previous studies was to examine the self-diffusion of sheared droplets due to collisions, the focus of our work is not on the trajectories and deformation of colliding droplets but rather on determining the critical conditions for coalescence in phase field models and studying the behaviour of the film between the drops at near-critical conditions. In simulations with the free-energy lattice Boltzmann method[6], we have previously found[30] conditions at which colliding droplets in impulsively-started simple shear flow do not coalesce. In these simulations, the interface profile was resolved well to ensure that coalescence occurred as a consequence of the phase field dynamics without artifacts of a poorly resolved diffuse interface. The resolution of these previous simulations proved insufficient to determine the effective physical size of the simulated droplets, and we now address this question by presenting simulations with twice the previous droplet size. Due to the larger drop size, we can now determine the critical capillary number for coalescence at an initial offset in the velocity gradient direction of 20% the diameters of the drops, near the value (16%) in the experiments of Chen et al. [17].

In the sections that follow, we briefly describe the numerical method and sample results with twice the resolution of our previous work[30]. We then present the details of the inter-

face behaviour during a collision, including the evolution of the minimum distance between the droplets and the orientation of the film between them. We compare the critical capillary number in the simulations with experimental values, accounting for differences in the conditions, and examine the role of diffusion in the behaviour of the thin film between the drops. We conclude with remarks on the prospects of predictive simulations of coalescence with Cahn-Hilliard-type phase field models.

4.2 Numerical model

The numerical method and its implementation are the same as we have used previously[30]; the scale of the computations is, however, significantly larger. We use the free-energy binary-liquid lattice Boltzmann method[6] to perform the simulations. In general, lattice Boltzmann methods (LBMs) compute flows by evolving a discrete probability density function for the velocity distribution of fictitious fluid molecules[31]. This is typically implemented in a two-step process: motion (or streaming) of the molecules along the discrete directions connecting adjacent lattice nodes and collisions between molecules, which are modelled as relaxation towards an equilibrium velocity distribution. We use the BGK (Bhatnagar-Gross-Krook[32]) collision operator. The bulk flow properties (density, velocity, and stress) are computed by summation of moments of the probability distribution, and provided that flow speeds are slow (compared to the speed of sound in the lattice), they satisfy the incompressible Navier-Stokes equation.

To model a mixture of two liquids, a second probability density function is used to compute the advection and diffusion of a scalar composition variable, the phase field φ. The simulations are three dimensional, and both the hydrodynamic and phase field lattices have 19 discrete velocities. The phase field evolves according to the advection-diffusion equation

$$\frac{\partial \varphi}{\partial t} + \nabla(\varphi \vec{u}) = M\nabla^2 \mu_\varphi \tag{4.1}$$

where $\mu_\varphi = A\varphi\left(\varphi^2 - 1\right) - \kappa_\varphi \nabla^2 \varphi$ is the chemical potential, and M is the mobility. The phase field dynamics and flow are coupled through a modified pressure tensor in the flow solver. With the specified chemical potential, the fluid separates into two phases with $\varphi = \pm 1$. The two parameters A and κ_φ in the chemical potential together specify the thickness and tension of the interface. The steady solution for φ across a planar interface between two semi-infinite domains is

$$\varphi(x) = \tanh\left(\ell_\varphi^{-1}x\right) \tag{4.2}$$

where $\ell_\varphi = \sqrt{2\kappa_\varphi/A}$ is a characteristic length of the distance over which φ varies between

its values in the two domains (± 1). Based on previous work[30], all simulations were performed with $\ell_\varphi = 2$ (lattice spacings) to ensure that the interface is well-resolved. It was previously shown[30] that simultaneously doubling ℓ_φ, the droplet radius, and the domain size does not change the behaviour of colliding drops. Therefore with $\ell_\varphi = 2$, coalescence is a consequence of the dynamics of the phase field without significant discretization errors. The thickness of the interface is larger than the characteristic length ℓ_φ: 95% of the change in composition across an interface occurs over the distance $3.7\ell_\varphi$; 99% of the change occurs over $5.3\ell_\varphi$. For large droplets (with a radius that exceeds 20 lattice nodes[10]), the interfacial tension σ may be determined from the excess free energy of a planar interface (Eq. 4.2) to be

$$\sigma = \frac{2\sqrt{2}}{3}\sqrt{\kappa_\varphi A} \tag{4.3}$$

The conditions of the simulations can be described with several dimensionless numbers that capture the hydrodynamics, interfacial properties, and geometry of the simulated system. Figure 4.1 shows a schematic of the cross-section through the centre of the simulation domain along the omitted z axis. This figure provides the definitions of the variables that describe the initial geometry of the simulated system and the variables of interest for the later analysis. Two shear planes separated by a distance H move in opposite directions at a speed u_0. Between them, two droplets with equal radii R are located in the middle of the domain, separated by a (non-dimensional) horizontal separation $\Delta X/(2R) = 1.26$ and a vertical offset $\Delta Y/(2R) = 0.2$. The confinement of the droplets is $2R/H = 0.39$. The minimum distance between the interfaces of the droplets is h, and the film inclination angle θ_f is the angle of the tangent to the interface of the higher droplet at the point of minimum distance from the lower droplet. The other dimensions of the system are a length $L = 2H$ in the x direction (shear direction), a height H in the y direction (velocity gradient direction), and a width $W = H$ in the z direction (vorticity direction). The simulations only compute one quarter of the full $L \times H \times W$ system because symmetry boundary conditions are employed along the $z = 0$ and $z = W/2$ planes and a rotational symmetry condition is used at $y = 0$. The $x = \pm L/2$ boundaries are periodic. While the hydrodynamic field has a shear condition at $y = H/2$, the phase field has a symmetry condition on this plane. The shear condition is implemented using the method of Ladd [33] because this method conserves the density of the fluid along the boundary, which is an important feature for our simulations that run for several million time steps.

The Reynolds number of the shear flow is

$$\mathrm{Re} = \frac{\dot{\gamma}R^2}{\nu} \tag{4.4}$$
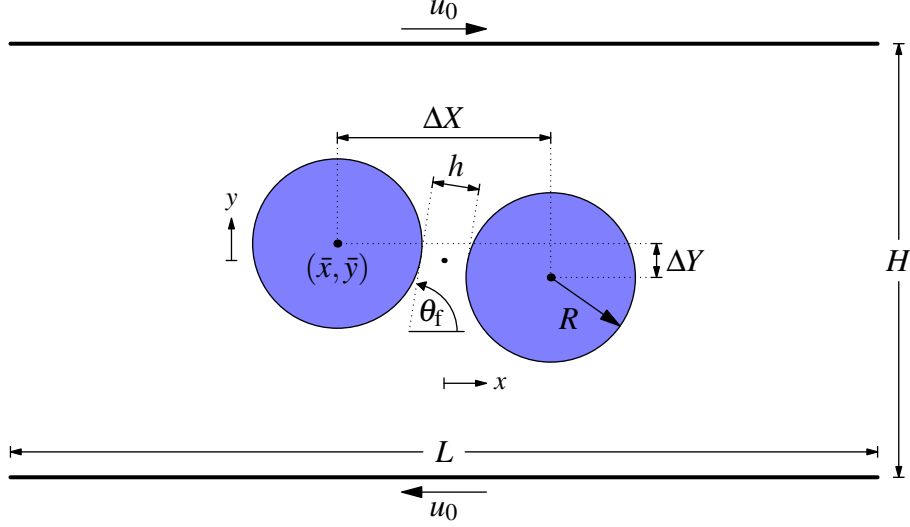
Figure 4.1: Schematic of the cross section through the simulated three dimensional domain including the definitions of variables that describe the geometry and conditions of the colliding droplets. The omitted z axis points out of the page, and this cross section is at $z = 0$.

based on $\dot{\gamma}R$ as the characteristic speed, where $\dot{\gamma} = 2u_0/H$ is the shear rate, and the radius R of both droplets as the characteristic length. The kinematic viscosity of the droplet and bulk fluids is $v = 1/6$ (in lattice units which corresponds to a relaxation time of one for the collision operator of the LBM hydrodynamic density distribution). All simulations are performed with Re $= 1$ as in previous work[30].

We define the capillary number Ca as

$$Ca = \frac{\rho v \dot{\gamma} R}{\sigma} \tag{4.5}$$

where $\rho = 1$ (in lattice units) is the density of the fluid. The interface Péclet number

$$Pe = \frac{\dot{\gamma} R \ell_\varphi}{MA} \tag{4.6}$$

expresses the ratio of the rates of advection and diffusion of φ over the characteristic distance of the interface thickness. As in previous work[30], we use Pe $= 10$, a value at which simulations of droplet deformation in shear were found to be accurate[3]. In the specification of the mobility in the LBM for the phase field, the relaxation time in the collision operator is kept fixed at one.

We present simulations in which the radius of each droplet spans 200 lattice spacings, twice the radius of our previous work[30] and 100 times the characteristic length ℓ_φ of

73

the diffuse interface. The simulated domain is eight times larger than previously, spanning $2048 \times 512 \times 512$ lattice nodes (which is one quarter of the full system domain due to symmetry). We consider the range of capillary numbers from 0.01 to 0.25 with more simulations performed near the critical capillary number for coalescence, approximately 0.2.

4.2.1 Implementation

The numerical model is highly amenable to parallelization because the computations at each lattice node of the domain require information from only the adjacent nodes. The locality of the calculations also allows acceleration of the simulations through the use of graphics processing units (GPUs) instead of conventional (multicore) central processing units (CPUs). The limited memory available on GPU devices, however, necessitates splitting the computational domain across multiple devices and communicating boundary layers between them. The simulations were run on two Compute/Calcul Canada GPU clusters with NVIDIA Tesla M2070 GPUs. One cluster has three GPUs per node (of which 66 GPUs were used); the other, which has two per node (of which 64 were used), performs the computations slightly faster. The average speed on the faster system is 1248 million lattice updates per second (Mlups). In comparison, an implementation of the same method runs at 2 Mlups on eight conventional CPU cores[2]. On both systems, communication between GPUs on the same node occurs over a system bus, while communication over the Infiniband interconnect between nodes is performed with a Message Passing Interface (MPI) library. A cross section of the phase and velocity fields through the middle of the domain is saved every 32000 time steps (a non-dimensional time interval of $\dot{\gamma}\Delta t = 0.133$). All computations are performed with double precision and with error checking and correction (ECC) enabled on the GPUs.

4.3 Results and discussion

Since the critical capillary numbers at the conditions of the new simulations, specifically $R/\ell_\varphi = 100$ and $\Delta Y/(2R) = 0.2$, were not known, several capillary numbers between 0.01 and 0.25 were chosen to explore the parameter range and observe the nature of the collisions. These simulations also provided the intervals that were then bisected repeatedly to determine the critical capillary numbers. At the conditions of the present and previous work[30], two critical capillary numbers separate three possible outcomes. Below the lower critical capillary number, droplets coalesce. Above the upper critical capillary number, the

droplets slide over each other and their interfaces never merge. Between the two critical values, the droplet interfaces merge, the bridge between them grows, and eventually this bridge breaks because the merging droplet is sheared apart faster than the bridge grows[30]. A sample simulation at Ca = 0.200, which is in this intermediate region and near the upper critical capillary number, is shown in Figure 4.2. The visualizations of cross-sections through the droplets reveal several fine details due to the high resolution of the simulations. After the droplets approach, a thin film forms with an initial inclination angle $\theta_f \approx 45°$. The shapes of the droplets until this time qualitatively match the front-tracking simulations of Olapade et al. [27] at similar conditions (Re = 2, Ca = 0.2, $\Delta X/(2R) = 1.25$, and $\Delta Y/(2R) = 0.125$). They are also similar to boundary integral simulations at Ca = 0.3 with $\Delta X/(2R) = 5$ and $\Delta Y/(2R) = 0.25$ [19]. While Olapade et al. [27] and Loewenberg and Hinch [19] do not simulate coalescence, in our simulations the droplets start to slide over each other, and the film rotates and thins until two dimples form when the film is parallel to the shear direction. As the interfaces merge, a drop of the bulk fluid is trapped in the growing bridge. As this bridge grows, the lobes at the ends continue to be sheared apart, and the bridge thins and rotates. The end lobes eventually pinch off. The bridge retracts, leaving an encapsulated droplet of the bulk fluid in the centre and a droplet between this central droplet and each of the recently pinched-off drops. At Ca = 0.202, the breakup of the bridge produces two additional drops (Fig. 4.3). The number of drops and their positions and sizes is notably similar to the experiments and simulations of filament breakup by Tjahjadi et al. [34] for equal drop and external liquid viscosities. These sample simulations shown in Figs. 4.2 and 4.3 are very close to the upper critical capillary number. This upper critical Ca is between 0.2020 and 0.2028 based on a sequence of simulations that successively bisected the initial range 0.2–0.25. A precise estimate of the lower critical capillary number that determines whether the growing bridge breaks is not available from the simulations of this study. The lower critical capillary number is between 0.1 and 0.2, and likely between 0.15 and 0.2, but the simulation at 0.15 was stopped immediately after the interfaces merged to provide computing resources instead for simulations near the upper critical Ca. Complete coalescence at Ca = 0.15 is expected because $\theta_f > 0$ at the time of coalescence. In this orientation, the applied shear compresses the growing bridge rather than stretching it. In all the cases where the droplet breaks after coalescing, the capillary number is less than required to break an initially stationary drop. Breakup after temporary coalescence occurs because the bridge does not grow quickly enough to achieve a near-equilibrium shape before the growing drop is sheared apart[30] and not because the critical Ca for breakup in an impulsively-started flow is exceeded by the coalesced drop. With Re = 1 and equal droplet and external viscosities, initially spherical droplets in an impulsively-started shear

flow break when the capillary number exceeds 0.28[2, 35]. Since the coalesced drop has twice the volume of each initial drop, its radius and capillary number would be $2^{1/3} \approx 1.26$ times larger than those of the initial drops. Therefore the droplet formed after coalescence must break when the capillary number of the two initial droplets exceeds 0.22, which is higher than the critical capillary number for coalescence at the simulated conditions.

$\dot{\gamma}t = 0.3$ $\quad$ $\dot{\gamma}t = 4.3$ $\quad$ $\dot{\gamma}t = 6.7$

$\dot{\gamma}t = 8.1$ $\quad$ $\dot{\gamma}t = 8.4$ $\quad$ $\dot{\gamma}t = 10.3$

$\dot{\gamma}t = 18.8$ $\quad$ $\dot{\gamma}t = 20.9$ $\quad$ $\dot{\gamma}t = 21.3$

$\dot{\gamma}t = 21.7$ $\quad$ $\dot{\gamma}t = 22.3$
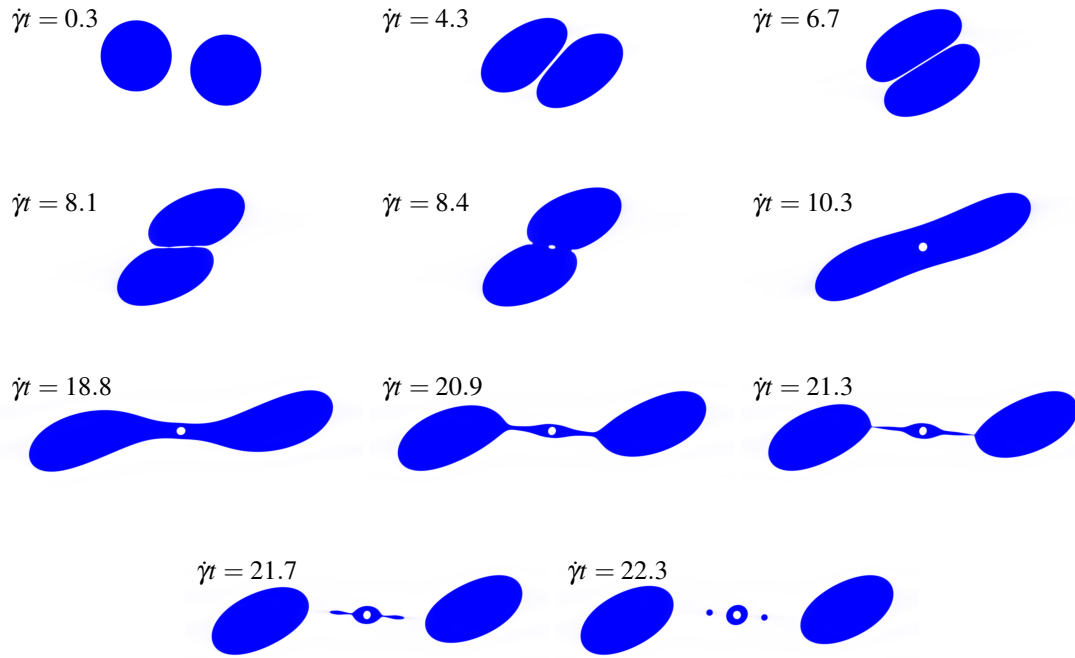
Figure 4.2: Coalescence and subsequent breakup at Ca $= 0.200$, Re $= 1$, $\Delta X/(2R) = 1.26$, $\Delta Y/(2R) = 0.2$, and $2R/H = 0.39$.

Sample trajectories of the upper droplet at capillary numbers between 0.01 and 0.25 are shown in Fig. 4.4. The droplets coalesce at progressively later stages of the collision with increasing capillary number. These trajectories reveal two features of the collisions. The first feature is the compression and deformation of the droplets. For reference, the solid line in Fig. 4.4 shows the circle that would be traced out by a sphere rotating in contact with another identical sphere with the same size as the initially spherical droplets. The centres of mass of the two colliding droplets approach much closer than the initial diameters of the drops. At Ca $= 0.25$, the minimum distance between the centres of mass of the two drops is 58% of the diameters. Only at the lowest capillary number considered (Ca $= 0.01$) does the trajectory temporarily follow the path of rigidly rotating spheres before coalescing. We point out that at this low capillary number, the droplets coalesce slightly later and higher than at Ca $= 0.05$. The second noteworthy feature of the trajectories is the absence of
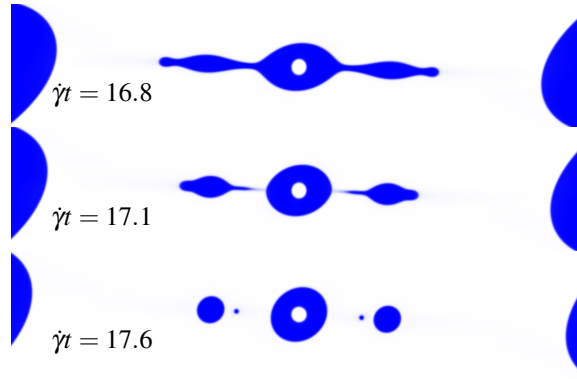
Figure 4.3: Breakup of the temporarily coalesced drop at Ca = 0.202. Compared to Ca = 0.200 (Fig. 4.2), the drop breaks earlier and two more drops form. The full domain has been cropped to focus on the breaking bridge.

an abrupt change as the capillary number crosses the upper critical value. As the critical capillary number is approached from above and below, the trajectories converge to the same shape. The motion of the droplets is unaffected by the details of the behaviour of the film between them unless this film ruptures and triggers a change in the topology of the fluid domain. As will be shown later, the film behaviour changes significantly in several ways as the capillary number approaches the upper critical value.

We briefly compare the trajectory of a non-coalescing drop (Ca = 0.21 in Fig. 4.4) with other simulations reported in the literature for similar conditions. The vertical position of this trajectory achieves a minimum soon after the shear flow starts and later reaches a maximum of $\bar{y}/R = 0.79$. Guido and Simeone [20] obtained a peak of $\bar{y}/R = 0.88$, independent of the initial vertical offset in experiments at low Re, Ca = 0.13, and a droplet viscosity 0.36 times the external viscosity. Simulations by Loewenberg and Hinch [19] with equal viscosities, $\Delta Y/(2R) = 0.25$, and Ca = 0.1 and 0.3 show peaks at $\bar{y}/R = 0.88$ and 0.77, respectively. Front tracking simulations have been used to study collision trajectories under a wide range of conditions, including finite inertia[27–29]. A maximum $\bar{y}$ is not seen in simulations of unconfined droplets at Re = 1, equal viscosities, and Ca = 0.2[27], but a finite domain size causes a maximum to appear[27]. The presence of an initial downward trajectory has been observed by others. It is enhanced by high Re, high Ca, small vertical offset, large horizontal separation and low drop viscosity relative to the external fluid[27, 28]. The purpose of these previous studies was, in general, to determine the increase in vertical offset between droplets after a collision and study the self-diffusion of drops in emulsions. Our interest, however, is in the details of the film behaviour and we do not consider the trajectories in further detail.

In the sections that follow, we examine the behaviour of the film between the drops at
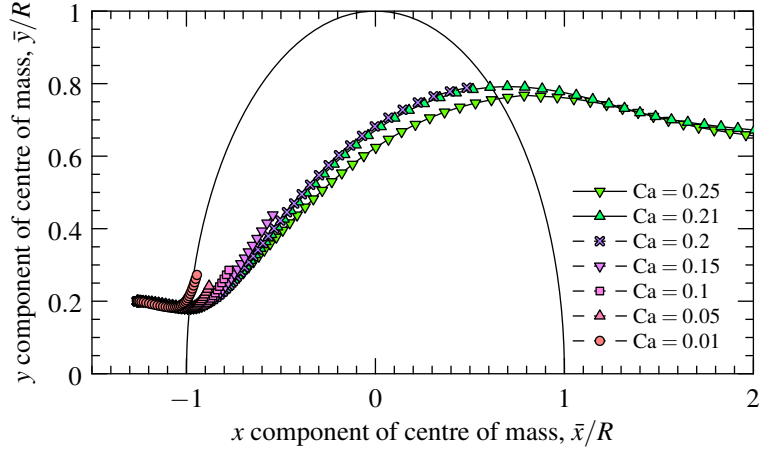
Figure 4.4: Position of the centre of mass $(\bar{x}, \bar{y})$ of the upper droplet during collisions at several capillary numbers. The solid line shows the trajectory of one sphere in a pair of touching rigid spheres rotating about the origin. The time interval between consecutive symbols is $\dot{\gamma}\Delta t = 0.133$.

capillary numbers near the upper critical value. Of the two critical capillary numbers, the upper critical number decreases faster with increasing radius of the drops (relative to the interface thickness)[30]. For sufficiently large drops, only one critical Ca separates the conditions for coalescence and sliding; temporary coalescence is not observed. These trends were determined for collisions with higher vertical offsets (0.86 and 0.6) than the present work, and we assume that the same trends hold for $\Delta Y/(2R) = 0.2$, specifically that the lower critical Ca decreases slower than the upper critical Ca as R/ℓ_φ increases. Therefore it is the upper critical Ca that should be compared with critical Ca for coalescence of larger droplets, for which experimental critical capillary numbers are available but simulations are not feasible due to excessive computational demands. In the remainder of this chapter, the upper critical capillary number is denoted Ca_c, and we do not discuss the lower critical Ca further.

4.3.1 Film behaviour

Due to the large domain size and limited computing and storage resources (20 GiB is required to store all values of φ, ρ, and the three velocity components in the $2048 \times 512 \times 512$ domain), we analyze cross-sections through the middle of the domain ($z = 0$) in the $x - y$ plane. The interface is located where $\varphi = 0$, and we calculate the minimum distance between polygonal droplet contours determined by bilinear interpolation of the values of φ at each lattice node[36]. We focus on capillary numbers near the critical value and examine the minimum distance between the two interface contours when they are in close proximity

and a film can be considered to exist. Figure 4.5 shows the evolution of the minimum distance between the drops as a function of time for all simulations. Three stages are evident in the interaction between the droplets for capillary numbers in the interval $0.20 \leq \text{Ca} \leq 0.25$: an approach phase that lasts until $\dot{\gamma}t \approx 5$, a film thinning stage until $\dot{\gamma}t \approx 8.5$ at the latest, and finally a separation or coalescence stage. At lower capillary numbers, i.e. $\text{Ca} < 0.2$, droplets coalesce before a distinct film thinning stage occurs.
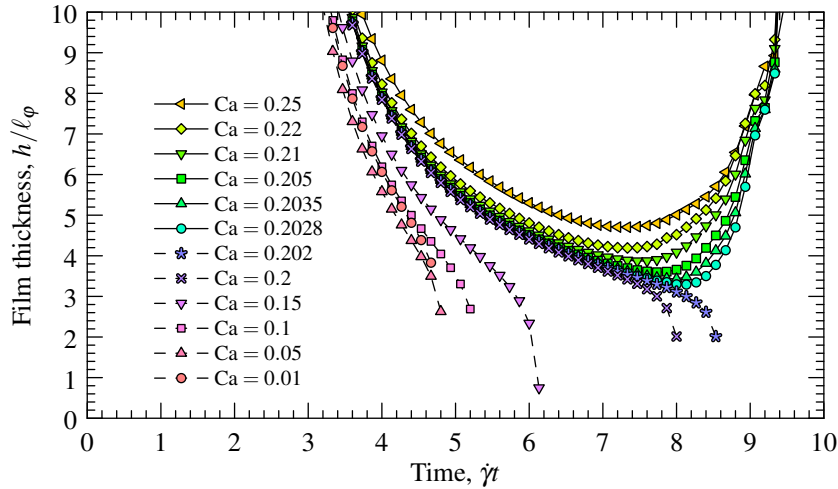
Figure 4.5: Minimum distance between droplets as a function of time for collisions at capillary numbers between 0.01 and 0.25.

Among the simulations in which the interfaces never merge, the smallest film thickness observed is $3.3\ell_\varphi$ with $\text{Ca} = 0.2028$. Over this distance, 93% of the change in φ across a flat interface (Eq. 4.2) occurs. The minimum film thickness is therefore similar to the thickness of the interface, and only a small overlap of adjacent interfaces is needed to start coalescence. While the range for the critical capillary number (0.202–0.2028) is at most 0.4% of its value, the minimum film thickness at the lowest supercritical capillary number (0.2028) provides a significantly less precise estimate of the critical film thickness. The dependence of the minimum film thickness on the capillary number reveals a better estimate of the critical thickness. A power law model $h_{\min} - h_{\text{c}} = \alpha \left(\text{Ca} - \text{Ca}_{\text{c}}\right)^n$ describes the dependence well. In this model, the difference between the minimum film thickness $h_{\min}$ and the critical film thickness h_{c} is proportional to a power of the difference between the capillary number and the critical capillary number Ca_{c}. The capillary number Ca is an input to the simulations, $h_{\min}$ is an output, and h_{c}, α, Ca_{c}, and n are fitting parameters. As shown in Fig. 4.6, the fit is excellent, though we note that four model parameters have been estimated from six simulations. A least squares fit provided the estimated critical capillary number $\widetilde{\text{Ca}}_{\text{c}} = 0.20245$ and the estimated critical film thickness $\tilde{h}_{\text{c}}/\ell_\varphi = 3.00$.

The fitted exponent is $\tilde{n} = 0.363$, and the proportionality factor is $\tilde{\alpha} = 5.13$. The fitted critical capillary number is higher than the highest subcritical Ca that has been simulated (0.202), raising confidence in the model. The critical film thickness cannot be determined more precisely with the current resolution of the simulations. Based on the fitted model, the capillary number may only exceed the critical value by $3 \times 10^{-4}\%$ for the minimum film thickness to be within 1% of the critical value. At the lowest supercritical Ca we simulate (0.2028), the minimum film thickness is $0.29\ell_\varphi$, or 0.58 lattice nodes, higher than the critical value, which is 10% of the critical thickness. To determine a more precise critical thickness, simulations with a thicker interface, i.e. $\ell_\varphi > 2$ and a proportionally larger droplet radius and domain, are needed. Further bisections of the critical range with $\ell_\varphi = 2$ are not worthwhile due to the imprecision of minimum film thicknesses obtained from interface contours that are computed by interpolating between the values of φ at lattice nodes.
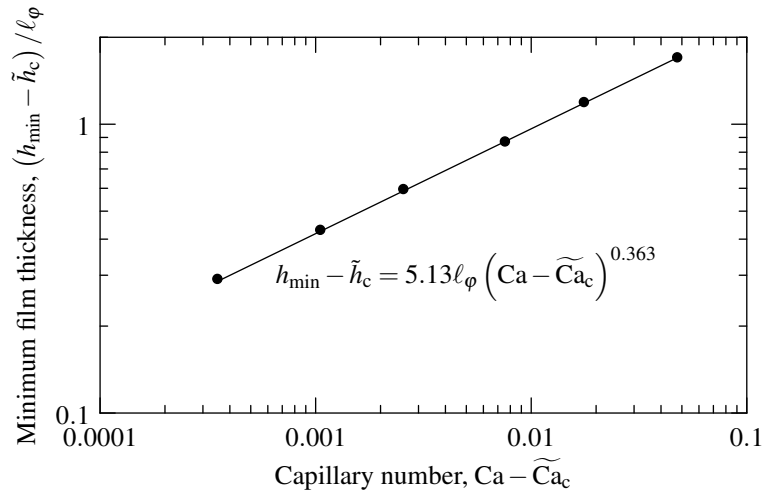
Figure 4.6: Dependence of the minimum film thickness on the capillary number. The proportionality factor, exponent, critical film thickness ($\tilde{h}_c/\ell_\varphi = 3.00$), and critical capillary number ($\widetilde{Ca}_c = 0.20245$) were determined by least squares fitting.

The dynamics of the film thinning process can be understood better by considering how the rate of film growth/thinning varies with the film thickness near the critical conditions. Figure 4.7 shows a phase portrait of the film thinning dynamics at near-critical capillary numbers. Time proceeds from the bottom right to the top right (supercritical Ca) or the bottom left (subcritical Ca). States in the upper left quadrant of the figure, where the film would grow while having a subcritical thickness, are not reached. The phase portrait emphasizes the sensitivity of the collision outcome and film dynamics to small changes in the capillary number, and it reveals several interesting features of the film drainage process. At

supercritical capillary numbers, a minimum film thickness must necessarily exist, and the thinning rate must be zero when the film is thinnest. An arrow along $\mathrm{d}h/\mathrm{d}t = 0$ indicates the extrapolated critical film thickness (Fig. 4.6). As $\mathrm{Ca} \downarrow \mathrm{Ca_c}$, $\mathrm{d}h/\mathrm{d}t$ increases quickly soon after $\mathrm{d}h/\mathrm{d}t = 0$ (see also Fig. 4.5). This can be seen as a vertical straightening of the trajectory in phase space as it crosses $\mathrm{d}h/\mathrm{d}t$ with decreasing Ca and a corner in the film thickness as a function of time (at $\dot{\gamma}t \approx 8.5$ in Fig. 4.5). These results suggest that $\mathrm{d}h/\mathrm{d}t$ soon after the time of minimum thickness may diverge as $\mathrm{Ca} \downarrow \mathrm{Ca_c}$.
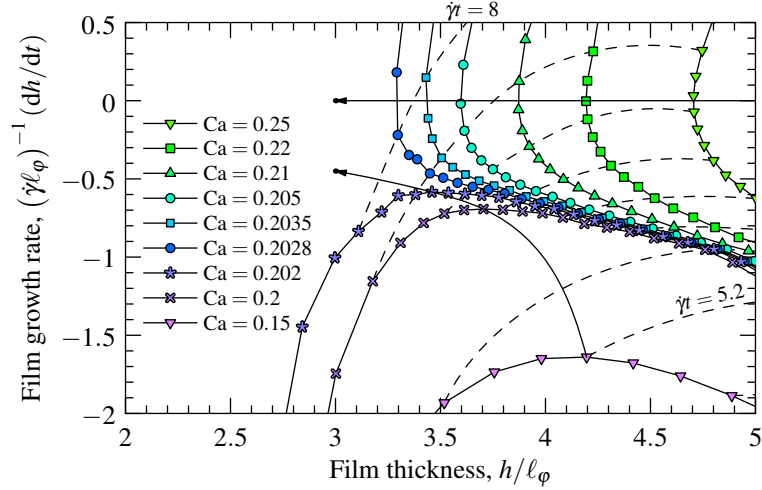
Figure 4.7: Dynamics of the film thickness h at near-critical capillary numbers. The dashed curves connect points at equal times spaced by $\dot{\gamma}\Delta t = 0.4$ with the latest (upper left) at $\dot{\gamma}t = 8$. The arrows indicate the locations of the estimated critical minimum thickness and potential position of the critical minimum thinning rate.

The bisection method for finding the critical conditions led to few simulations at subcritical capillary numbers. Fig. 4.7 shows that the presence of a minimum thinning rate is a unique feature of the subcritical simulations, a feature that can also be seen as an inflection point in Fig. 4.5. In general, the film thins at a decreasing rate until reaching either a minimum thickness (and then separating) or a minimum thinning rate (and then accelerating to coalescence). The minimum thinning rate decreases as the capillary number increases to its critical value, but the two highest subcritical cases do not clearly indicate whether the critical minimum thinning rate reaches zero or a particular positive value (negative $\mathrm{d}h/\mathrm{d}t$). The region of inadmissible states in Fig. 4.7 is therefore not yet precisely known. The film thickness at the time when the thinning rate reaches its minimum exceeds the critical film thickness, and it decreases as $\mathrm{Ca} \uparrow \mathrm{Ca_c}$. Therefore the outcome of subcritical simulations is known the moment a minimum thinning rate occurs, which is before the critical thickness is reached. Furthermore, at near-critical Ca, the film rotates rapidly, and therefore its inclination at the time of coalescence differs from the inclinations when the thinning

rate is minimum and when the thickness crosses the critical value. This raises questions about whether the attainment of a critical film thickness is an appropriate phenomenological model for determining when coalescence occurs. This criterion has been used to specify when meshes of nearby droplets are connected in some simulation methods[37, 38].

Figures 4.5 and 4.7 have shown the outcome of the competition between the hydrodynamic forces that pull the droplets apart in the late stages of the collision and the film flow and phase field dynamics that lead to coalescence. It is important to emphasize that the dynamics described in these figures are for the distance between the two closest points on the droplets, and the behaviour in the whole film is more complex. An examination of the flow in a cross-section of the film at the lowest supercritical capillary number (0.2028) reveals an interesting feature of the flow in the film near the critical conditions. The flow field $\vec{u}$ in the film may be considered the sum of a rigid rotation at the rate with which the film is rotating $(\mathrm{d}\theta_\mathrm{f}/\mathrm{d}t)$ and a velocity relative to this rigid rotation. Figure 4.8 shows that this relative fluid motion is out of the film at $\dot{\gamma}t = 4.5$, as expected for a draining film. However, by $\dot{\gamma}t = 6.9$, the flow reverses, and now points into the film. These relative flow speeds are small, about one tenth of the characteristic speed $\dot{\gamma}R$, and should be compared with spurious currents (in the absence of applied shear) to ensure that the relative flows are not a similar magnitude. Though a stationary simulation was not performed with $R = 200$, results for $R = 50$ and $R = 100$ indicate that spurious currents are sufficiently low. When Re and Ca are kept constant as R is increased by factor of two, $\dot{\gamma}R$ and σ are halved. With increasing R, spurious currents decrease because of the larger radius of curvature of the interface and the lower interfacial tension. The decrease in the maximum spurious speed appears to match the decrease in $\dot{\gamma}R$: maximum spurious speeds are $0.008\dot{\gamma}R$ with $R = 50$ and $0.009\dot{\gamma}R$ with $R = 100$, both at Ca = 0.1. For $R = 200$ and Ca = 0.1, spurious speeds are not expected to exceed $0.01\dot{\gamma}R$ and are likely lower for Ca = 0.2 due to the lower interfacial tension. The relative flow in the film is therefore an order of magnitude faster than the expected maximum spurious currents around a stationary droplet with the same interfacial tension.

The presence of a reversal in the film flow can also be seen in the absolute (not relative to rotation) flow field. Over the same time interval that the relative flow in the film reverses, the vorticity $\Omega = \partial u_y/\partial x - \partial u_x/\partial y$ (calculated by central finite differences of the velocity data) in the film changes sign from positive (counterclockwise) at $\dot{\gamma}t = 4.5$ to negative (clockwise) at $\dot{\gamma}t = 6.9$, as illustrated in Fig. 4.9. The flow fields do not change significantly near the critical capillary number and the same reversal phenomena were found in both sub- and supercritical simulations near Ca$_\mathrm{c}$. The reversal therefore happens before coalescence when the capillary number is sufficiently high: at Ca = 0.202, coalescence does not occur

until $\dot{\gamma}t = 8.5$. The reversal of the flow in the film occurs surprisingly early in the interaction: the film orientation angle is positive and the centres of mass of the droplets are not yet vertically aligned (they align at $\dot{\gamma}t \approx 7.1$). The reversal therefore occurs during what is usually considered the "compressive" stage of the collision.
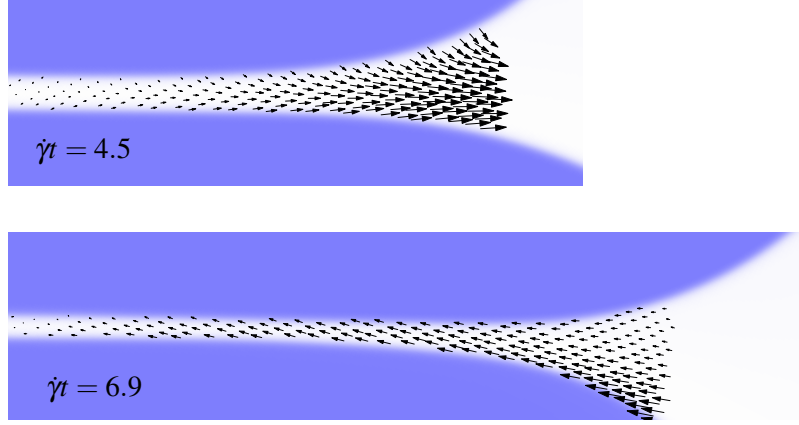
Figure 4.8: Flow fields in the film relative to rigid rotation at the rotation rate of the film $d\theta_{\mathrm{f}}/dt$ for the simulation with $\mathrm{Ca} = 0.2028$ at times $\dot{\gamma}t = 4.5$ (top) and 6.9 (bottom). The images have been rotated so that the film is horizontal. One arrow is shown for every fourth lattice node in both directions. To illustrate the structure of the flow, the lengths of the arrows are scaled relative to the maximum relative flow speeds at each time, which are $0.18\dot{\gamma}R$ ($\dot{\gamma}t = 4.5$) and $0.12\dot{\gamma}R$ ($\dot{\gamma}t = 6.9$).
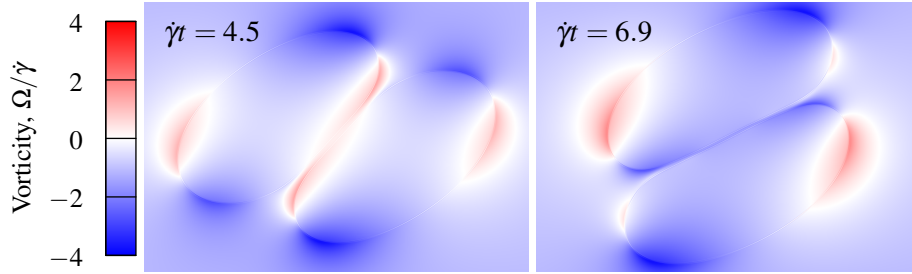
Figure 4.9: Vorticity $\Omega = \partial_x u_y - \partial_y u_x$ (normalized by the applied shear rate $\dot{\gamma}$) in the film, the drops, and the nearby fluid at $\dot{\gamma}t = 4.5$ (left) and 6.9 (right) for the collision with $\mathrm{Ca} = 0.2028$.

When the flow reversal occurs, the thickness of the film is between one and two times the interface thickness. One should therefore consider whether the flow in the film is adequately resolved with this thickness. Simulations of confined droplet motion in a channel with the same free-energy binary-liquid LBM have been reported[39]. The thickness of the film between the drop and the wall was found to be accurate when it was at least twice the interface thickness. However, the thickness of the film changed only 4% when the resolution was halved. We therefore consider that the flow in the film is reasonably resolved until

the thickness of the film approaches the critical thickness (which is similar to the interface thickness). It is important to note that one cannot have full resolution of the film (by choosing R/ℓ_φ so that for example $h_{\min} \gtrsim 8\ell_\varphi$ to meet the criterion given by Kuzmin et al. [39]) yet still observe coalescence, which requires the film thickness to reach the critical film thickness $h_{\mathrm{c}} = 3\ell_\varphi$. Low resolution of the flow in the film is not the reason for coalescence: coalescence occurs due to the phase field dynamics and gradients in chemical potential in the adjacent interfaces.

The continued decrease of the minimum distance between the interfaces despite the reversal of the flow in the film occurs due to fluxes of φ that counteract sharp gradients of chemical potential. Based on the film thickness and time when the reversal occurs, we may consider the mobility of the phase field to contribute significantly to the dynamics of h in the portion of Fig. 4.5 where $h \lesssim 5\ell_\varphi$. Consequently, diffusion of φ contributes to the dynamics of h throughout the ranges of time, thickness, and growth rate shown in the phase portrait, Fig. 4.7. This choice is consistent with a convergence study of the film thickness at supercritical capillary numbers (see appendix "Convergence of film thickness") in which the film thicknesses for two different Pe cross when $h = 6\ell_\varphi$ at near critical Ca. The independence of the film thickness to the Péclet number prior to the cross-over thickness suggests that the mobility does not have a significant effect on interfaces that are further apart.

We look more closely now at the rotation and thinning of the film during near-critical collisions. Figure 4.10 shows the film inclination angle as a function of time for several capillary numbers. Like the centre of mass (Fig. 4.4), the sub- and supercritical inclination angles converge as $\mathrm{Ca} \to \mathrm{Ca_c}$. Figure 4.11 illustrates the shapes of the thinnest films at the simulated capillary numbers, and Fig. 4.12 shows the films when the thinning rate is slowest and at moments before and after coalescence. For $\mathrm{Ca} \leq 0.15$, a single point of minimum film thickness exists, while two dimples are present when $\mathrm{Ca} \geq 0.2$ and a droplet of the external fluid forms inside the bridge. In the supercritical cases (Fig. 4.11), two dimples are present and the separation between them increases with increasing capillary number. The presence of two dimples is a hydrodynamic feature of a draining film[40]. As the capillary number decreases to the critical value, the minimum thickness occurs later in the collision process and therefore when the film is inclined further clockwise. At the lowest supercritical capillary number (0.2028), the film slopes downward ($\theta_{\mathrm{f}} = -4.2° < 0$). At subcritical capillary numbers (Fig. 4.12), the minimum thinning rate and coalescence occur later and with further clockwise rotation as the capillary number increases to its critical value. At the low capillary numbers, the film does not rotate significantly between the time of minimum thinning and subsequent coalescence. In contrast, a significant change in

inclination can be seen between these two times at $Ca \approx Ca_c$. For $Ca = 0.202$, the minimum thinning rate occurs when the film is inclined upward ($\theta_f = 16° > 0$) while coalescence occurs with a downward-inclined film ($\theta_f = -23° < 0$). Considering the phase portrait of the film thinning process (Fig. 4.7), we hypothesize that as $Ca \to Ca_c$ the angle at minimum thickness converges to the angle at minimum thinning rate and not the coalescence angle.
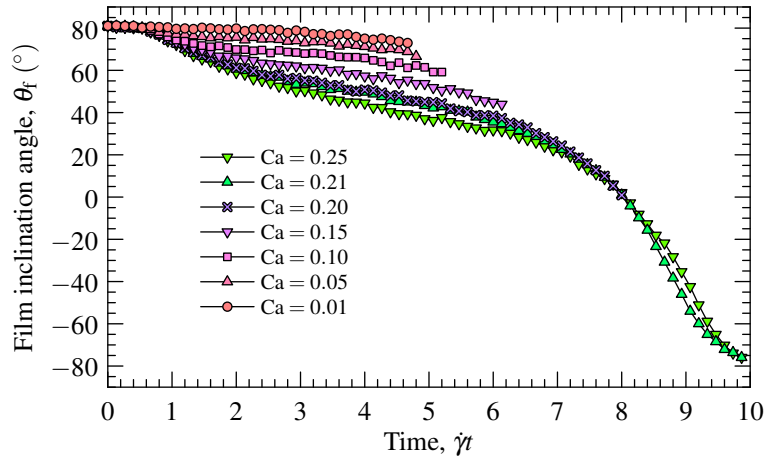
Figure 4.10: Film inclination angle as a function of time for several capillary numbers.
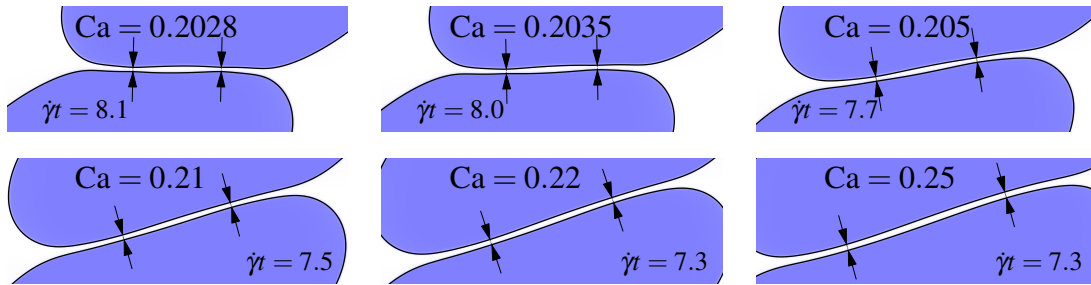
Figure 4.11: Cross-sections through the droplets at the time of minimum film thickness for $Ca = 0.2028, 0.2035, 0.205, 0.21, 0.22,$ and 0.25. The arrows indicate the locations where the films are thinnest.

Figure 4.13 summarizes the variation in the film inclination angle as a function of the capillary number at key events in the sub- and supercritical collision processes, and Fig. 4.14 presents the times of these events. As mentioned previously, the critical events occur later and with a lower film angle as the critical capillary number is approached from above and below. The time between the minimum thinning rate and coalescence increases as $Ca \to Ca_c$. Since the interaction between colliding drops occurs over a finite time interval, maximum times of minimum film thickness, minimum thinning rate, and coalescence must exist. However, the high sensitivity of the film behaviour to the capillary number
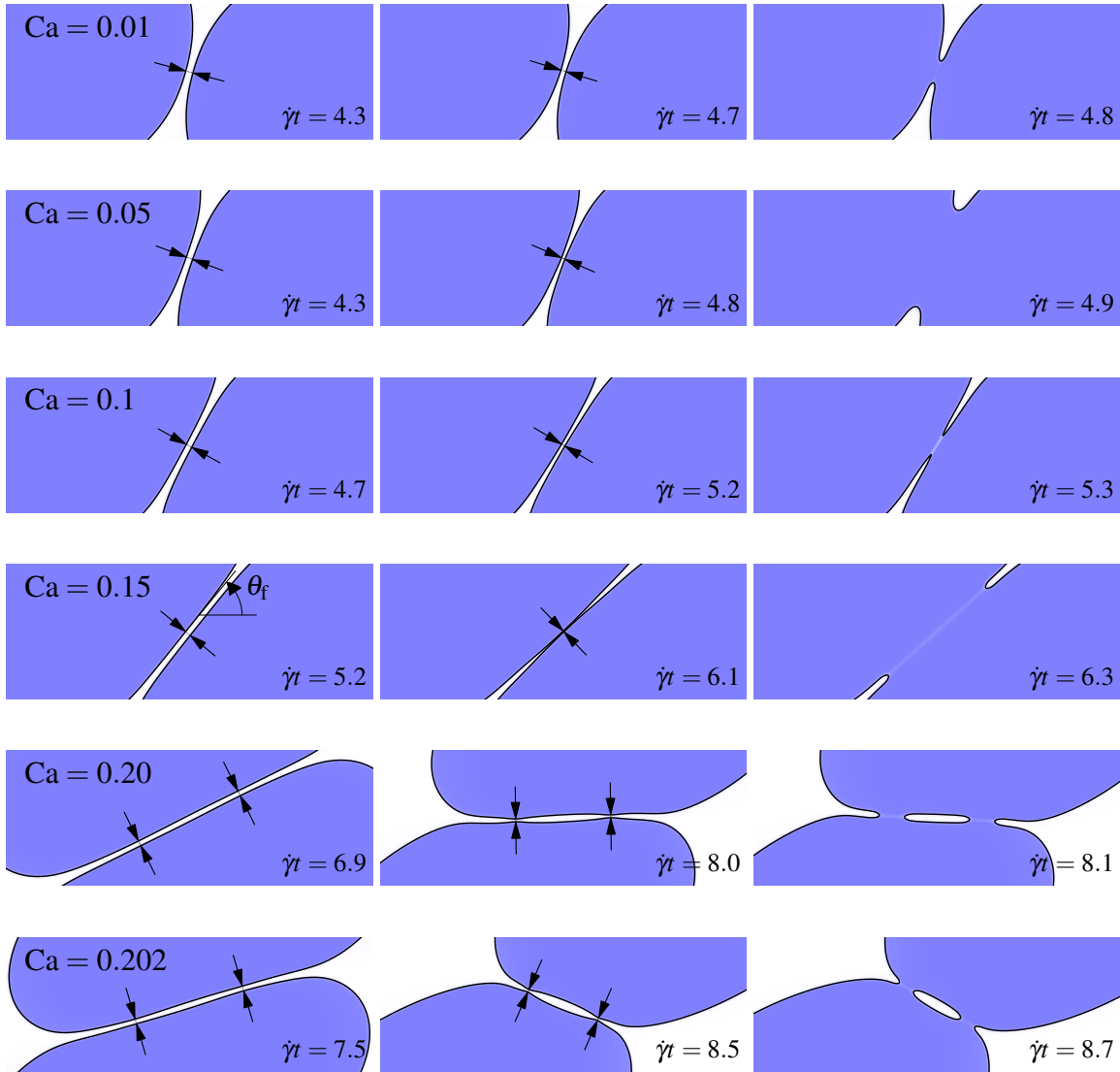
Figure 4.12: Cross-sections through the droplets at the time of slowest film thinning (left), at the last saved time step before coalescence (centre), and the first after coalescence (right) for (top to bottom) Ca $= 0.01, 0.05, 0.1, 0.15, 0.2, 0.202$. The time interval between the right pair of images is $\dot{\gamma}\Delta t = 0.133$. The arrows indicate the locations where the films are thinnest.

near Ca_c prevents an accurate estimate of these times and the critical angles. Based on the highest subcritical and lowest supercritical simulations, the maximum time for minimum thickness or minimum thinning exceeds $\dot{\gamma}t = 8.1$ while the maximum coalescence time exceeds 8.5. The corresponding critical angles are $\theta_f < -1.4°$ for minimum film thickness and thinning rate and $\theta_f < -23°$ for coalescence. Considering the small change in spacing between the lines that connect points at the same time in the phase portrait (Fig. 4.7), we estimate an upper bound of $\dot{\gamma}t \approx 8.4$ on the times of minimum film thickness and thinning rate, from which a lower bound of $-17°$ on the corresponding critical angle is estimated using $\theta_f(\dot{\gamma}t)$ at the lowest supercritical Ca.
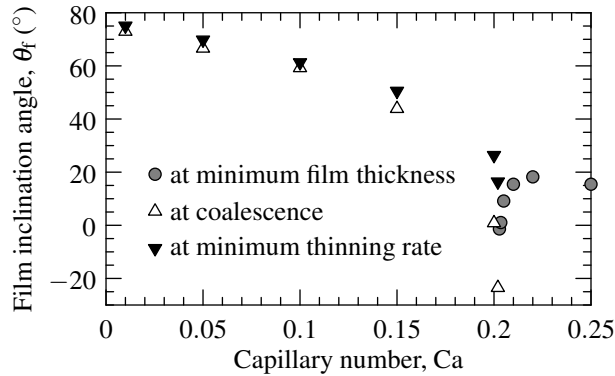
Figure 4.13: Film inclination angle at several events in the sub- and supercritical collision processes
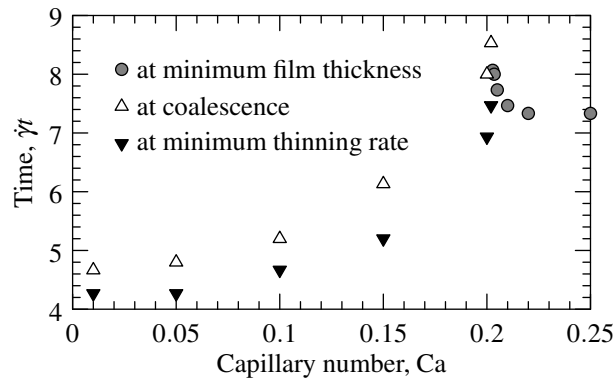
Figure 4.14: Times of key events in the collision processes at sub- and supercritical capillary numbers

4.3.2 Physical size of droplets

To estimate the physical size of the simulated droplets, we compare the critical capillary number of the simulations with experiments at similar conditions. Chen et al. [17] present critical capillary numbers for Newtonian polymer droplets (polydimethylsiloxane in poly-isobutylene) with radii between 54 and 158 μm at confinements $2R/H$ up to 0.315. The ratio of the droplet to bulk liquid viscosities was 1.1, and the difference in density was considered negligible. De Bruyn et al. [18] present similar experiments, but their viscosity ratio was 0.1, which we judge to be too low for a meaningful comparison with our current simulations. Guido and Simeone [20] did not determine critical capillary numbers for coalescence, but depending on the initial vertical offset, observed sliding and coalescence during extension with a $\sim$100 μm radius drop at $Ca = 0.13$ and a viscosity ratio of 0.36. The power law $Ca_c \sim R^{-0.84}$, in which the exponent is independent of the viscosity ratio[41], fit the confined and unconfined experiments of De Bruyn et al. [18] reasonably, and we use this model to extrapolate experimental Ca_c to smaller drop sizes. Using $Ca_c = 0.0075$ for experiments with $2R = 315$ μm, $2R/H = 0.315$ and $\Delta Y/(2R) = 0.16$[17], the critical capillary number is $Ca_c = 0.202$ when $R = 3.12$ μm. Use of this power law at high capillary numbers (at which the droplet trajectories deviate from those of rigid spheres) requires caution since this power law was determined for primarily extensional flow and has not been evaluated experimentally at capillary numbers higher than the 10^{-2} to 10^{-1} range considered by Hu et al. [41]. We note also that simulations at an initial offset of 0.6 and 0.86 provided exponents of -1.15 and -1.57, respectively[30], for critical capillary numbers between 0.02 and 0.2. We consider therefore the effect of a different exponent on the extrapolated physical size: With $Ca_c \sim R^{-1}$, the physical radius is 5.9 μm for the simulated drops; with $Ca_c \sim R^{-0.65}$ it is 1 μm.

A second way to estimate the physical size of the droplets is to consider the ratio of the droplet radius and the critical film thickness. In the simulations, this ratio is 33 based on the extrapolated critical thickness $3.00\ell_\varphi$. An order of magnitude estimate for the critical film thickness for the experimental polymer system is 27 nm[17]. The resulting physical size of the simulated droplets is $R = 0.89$ μm. Extrapolating this size and $Ca_c = 0.202$ to the experimental droplet size with the scaling $Ca_c \sim R^{-0.84}$, we obtain a critical capillary number of 0.0026 for a droplet with $2R = 315$ μm, compared with 0.007–0.008 reported by Chen et al. [17].

The two methods for estimating the physical size of the droplets agree to within a factor of 3.5 and indicate a physical radius between 0.9 and 3.1 μm. We consider this agreement to be reasonable given the uncertainty in determining physical critical film thicknesses,

the differences between the experimental and simulated parameters, and uncertainty in the variation of the critical capillary number with drop sizes in the range 1–10 μm where Ca_c is of order 10^{-1}. This range of droplet sizes is relevant to studies of polymer blends[42] and emulsions, such as those used in enhanced oil recovery that have mean droplet diameters between 1 and 12 μm[43].

Now that an estimate of the physical size of the droplets is available, we may assess whether the interface Péclet number is physically reasonable. For this purpose we define a modified Péclet number $\hat{Pe}$ that is the ratio of the timescale $h_c^2/(MA)$ for phase field diffusion over the critical film thickness and the droplet advection timescale $\dot{\gamma}$:

$$\hat{Pe} = \frac{\dot{\gamma}h_c^2}{MA} = Pe\frac{h_c^2}{\ell_\varphi R} \tag{4.7}$$

For the simulations, we have $\hat{Pe} = 0.9$, and the two timescales are effectively equal. In the limit $\hat{Pe} \gg 1$ interfaces cannot merge because insufficient diffusion occurs over the interaction time of a collision; for $\hat{Pe} \ll 1$ diffusion is quick and does not hinder coalescence during the interaction time. To relate the modified Péclet number with the other parameters of the system we note that

$$\hat{Pe} = Re\frac{\nu}{MA}\left(\frac{h_c}{R}\right)^2 \tag{4.8}$$

The modified Péclet number is thus the product of the Reynolds number, the ratio of the fluid kinematic viscosity and the phase field diffusivity, and the square of the ratio of the critical thickness and droplet radius. We estimate the diffusivity for liquids to be on the order of 10^{-9} m^2/s, as estimated by Jacqmin [4]. Using the viscosity of water $\nu = 10^{-6}$ m^2/s and $R/h_c = 33$, we obtain $\hat{Pe} = 0.92$. The simulations are therefore at a physically reasonable Péclet number. Since shear rates (and the factors in Eq. 4.8) may span many orders of magnitude, for example 10^{-4} to 10^4 s^{-1} for a typical rheometer, the Péclet numbers for physical systems are expected to span a similarly wide range. Since maximum possible shear rates and micron size droplets provide $\hat{Pe}$ of order one, $\hat{Pe}$ exceeding one are not expected for physical systems unless they have diffusivities much lower than 10^{-9} m^2/s. Table 4.1 summarizes the parameters of a sample physical system with the dimensionless parameters of the simulations. The required shear rate is below the maximum of a commercially available viscometer (10^7 s^{-1} for the Ultra Shear Viscometer, PCS Instruments, London, UK) and the required gap size is larger than the 1.25 μm of this device. The remaining values are typical for liquid systems. The purpose of this comparison is to show that the conditions of the simulations are applicable to physical systems; experiments with droplet collisions at this small size and high shear would need to address challenges such

as the generation and observation of the drops. Simulations at lower Re are possible, but would take longer to run since Re would be decreased by reducing the shear rate rather than increasing the fluid viscosity in the LBM we use.

Table 4.1: Parameters of a sample physical system with the same dimensionless parameters as the simulations

parameter	symbol	value
droplet radius	R	1 μm
gap between shear planes	H	5.1 μm
confinement	$2R/H$	0.39
kinematic viscosity (droplet and external)	ν	10^{-6} m^2/s
fluid density (droplet and external)	ρ	10^3 kg/m^3
shear rate	$\dot{\gamma}$	10^6 s^{-1}
wall speed	u_0	2.6 m/s
wall shear stress	$\rho\nu\dot{\gamma}$	10^3 Pa
Reynolds number	Re	1
interfacial tension	σ	5×10^{-3} N/m
capillary number	Ca	0.2

4.4 Conclusions

The interactions between adjacent interfaces during binary droplet collisions in simple shear flow were examined in high resolution phase field simulations with the free-energy lattice Boltzmann method. Large-scale parallel GPU computing was used to simulate droplets with radii spanning $R = 200$ lattice nodes in a $10R \times 5R \times 5R$ domain, of which only one quarter was computed by exploiting symmetry. The drops had the same density and viscosity as the external fluid, and the Reynolds number of the flow was fixed at one. The critical capillary number for coalescence at a low initial offset between the droplets (20% of the droplet diameters) was determined to within 0.4%. In collisions without coalescence, the difference between the minimum distance and a critical film thickness depends on the difference between the capillary number and the critical capillary number through a simple power law. This relationship was used to estimate a more precise critical capillary number and critical film thickness by fitting the power law to the minimum thicknesses and capillary numbers of several supercritical simulations. At subcritical capillary numbers, an inflection point (and a corresponding minimum thinning rate) exists in the evolution of the minimum film thickness over time. This inflection point occurs before the critical thickness is reached.

The rotating film between the droplets exhibits interesting behaviour at near-critical conditions. In this film, the flow relative to rigid rotation at the angular speed of the film reverses from exiting to entering the gap between the drops. The reversal of the (relative) flow coincides with a change in sign of the vorticity in the film. The minimum thickness between the interfaces continues to decrease after the flow reversal due to the phase field mobility. At near-critical capillary numbers, there are two points in the film where it is thinnest. As the critical capillary number is approached from subcritical conditions, the minimum thinning rate and coalescence occur at later times and with further clockwise rotation of the film. When approaching the critical capillary number under supercritical conditions, the minimum film thickness also occurs later and with further film rotation. Due to the high sensitivity of the film behaviour to the capillary number (even within 0.5% of the critical value), the details of the film behaviour in the critical capillary number limit, such as whether the minimum thinning rate approaches zero or a finite value, remain open questions.

The effective physical size of the simulated droplets could be estimated due to the similarity of the simulated conditions with those of droplet collision experiments in confined shear flow. The use of an empirical scaling for the dependence of the critical capillary number on the size of the droplets provided a 3.1 μm effective physical radius for the simulated droplets. The ratio of the simulated droplet size and the (numerical) critical film thickness, together with an (order of magnitude) estimate of the critical film thickness for the experimental fluid pair, provided another estimate of the physical size of the simulated droplets: 0.9 μm. The difference between these estimates is judged reasonable considering the imprecision of the scaling law, critical film thickness, and the differences in properties of the numerical and experimental fluid pair.

The late stages of the interaction between interfaces, specifically at and near the points of minimum distance to the adjacent interface, are determined by the phase field mobility. If it is sufficiently low, this mobility delays the merging of the interfaces. We show that the interface Péclet number Pe of the simulations, which was chosen based on studies of droplet deformation in shear, is reasonable for physical systems. However, a wide range of Péclet numbers is possible, and there is therefore a need to understand the effects of Pe better. Future work could examine how the mobility affects the phase portrait of the film thickness dynamics at near-critical conditions. The effects of the viscosity ratio, initial distance between the drops, and size ratio could also be evaluated. However, further studies of the behaviour under one set of conditions and comparison with experimental results are currently more important as they would examine the adequacy of phase field models in describing coalescence physics, thereby revealing the utility of further parameter studies.

Several other avenues are open for future work. Clusters with thousands of GPUs exist, and larger scale computations could be used to further bridge the gap between simulations and experiments. Multiscale modelling of interface behaviour would be useful for studies of large-scale flows where films cannot be fully resolved. Studies of relatively small fluid volumes could be used to study drop size distributions and population balance models for their evolution. A question to be addressed by multiscale modelling is whether the simplification that interfaces merge when they reach a critical thickness is reasonable. Considering the small length scales of the simulations, the effects of non-continuum phenomena are also an area for future work. One aim for future work is to further evaluate the applicability of phase field models to studies of coalescence phenomena and work towards nanoscale direct numerical simulations of interacting interfaces in the spirit of such studies of contact line motion[4, 44]. A second aim is to apply the insights from simulations to flows of many droplets under a wide range of conditions.

References

[1] R.G.M. van der Sman and S. van der Graaf. Emulsion droplet deformation and breakup with lattice Boltzmann model. *Comput. Phys. Commun.*, 178:492–504, 2008.

[2] A.E. Komrakova, O. Shardt, D. Eskin, and J.J. Derksen. Lattice Boltzmann simulations of drop deformation and breakup in shear flow. *Int. J. Multiphase Flow*, 59: 24–43, 2014.

[3] S. van der Graaf, T. Nisisako, C.G.P.H. Schroën, R.G.M. van der Sman, and R.M. Boom. Lattice Boltzmann simulations of droplet formation in a T-shaped microchannel. *Langmuir*, 22:4144–4152, 2006.

[4] D. Jacqmin. Contact-line dynamics of a diffuse fluid interface. *J. Fluid Mech.*, 402: 57–88, 2000.

[5] T. Qian, X.-P. Wang, and P. Sheng. Molecular scale contact line hydrodynamics of immiscible flows. *Phys. Rev. E*, 68:016306, 2003.

[6] A.J. Briant and J.M. Yeomans. Lattice Boltzmann simulations of contact line motion. II. Binary fluids. *Phys. Rev. E*, 69:031603, 2004.

[7] P. Yue and J.J. Feng. Can diffuse-interface models quantitatively describe moving contact lines? *Eur. Phys. J. Special Topics*, 197:37–46, 2011.

[8] J.W. Cahn and J.E. Hilliard. Free energy of a nonuniform system. I. Interfacial free energy. *J. Chem. Phys.*, 28:258–267, 1958.

[9] T. Qian, X.-P. Wang, and P. Sheng. A variational approach to moving contact line hydrodynamics. *J. Fluid Mech.*, 564:333–360, 2006.

[10] X. Jia, J. B. McLaughlin, and K. Kontomaris. Lattice Boltzmann simulations of flows with fluid-fluid interfaces. *Asia-Pac. J. Chem. Eng.*, 3:124–143, 2008.

[11] H. Farhat and J.S. Lee. Suppressing the coalescence in the multi-component lattice Boltzmann method. *Microfluid Nanofluid*, 11:137–143, 2010.

[12] T.J. Spencer, I. Halliday, and C.M. Care. A local lattice Boltzmann method for multiple immiscible fluids and dense suspensions of drops. *Phil. Trans. R. Soc. Lond. A*, 369:2255–2263, 2011.

[13] N. Bremond, A.R. Thiam, and J. Bibette. Decompressing emulsion droplets favors coalescence. *Phys. Rev. Lett.*, 100:024501, 2008.

[14] I. Zawadzki and M. Antonio. Equilibrium raindrop size distributions in tropical rain. *J. Atmospheric Sci.*, 45:3452–3459, 1988.

[15] C. Tsouris and L.L. Tavlarides. Breakage and coalescence models for drops in turbulent dispersions. *AIChE J.*, 40:395–406, 1994.

[16] P. Perlekar, L. Biferale, M. Sbragaglia, S. Srivastava, and F. Toschi. Droplet size distribution in homogeneous isotropic turbulence. *Phys. Fluids*, 24:065101, 2012.

[17] D. Chen, R. Cardinaels, and P. Moldenaers. Effect of confinement on droplet coalescence in shear flow. *Langmuir*, 25:12885–12893, 2009.

[18] P. De Bruyn, R. Cardinaels, and P. Moldenaers. The effect of geometrical confinement on coalescence efficiency of droplet pairs in shear flow. *J. Colloid Interf. Sci.*, 409: 183–192, 2013.

[19] M. Loewenberg and E.J. Hinch. Collision of two deformable drops in shear flow. *J. Fluid Mech.*, 338:299–315, 1997.

[20] S. Guido and M. Simeone. Binary collision of drops in simple shear flow by computer-assisted video optical microscopy. *J. Fluid Mech.*, 357:1–20, 1998.

[21] V. Cristini, J. Bł023awzdziewicz, and M. Loewenberg. An adaptive mesh algorithm for evolving surfaces: Simulations of drop breakup and coalescence. *J. Comp. Phys.*, 168: 445–463, 2001.

[22] W. Bartok and S.G. Mason. Particle motions in sheared suspensions. VIII. Singlets and doublets of fluid spheres. *J. Colloid Sci.*, 14:13–26, 1959.

[23] R.S. Allan and S.G. Mason. Particle motions in sheared suspensions. VIV. Coalescence of liquid drops in electric and shear fields. *J. Colloid Sci.*, 17:383–408, 1962.

[24] H. Yang, C.C. Park, Y.T. Hu, and L.G. Leal. The coalescence of two equal-sized drops in a two-dimensional linear flow. *Phys. Fluids*, 13:1087–1106, 2001.

[25] Y. Yoon, M. Borrell, C.C. Park, and L.G. Leal. Viscosity ratio effects on the coalescence of two equal-sized drops in a two-dimensional linear flow. *J. Fluid Mech.*, 525: 355–379, 2005.

[26] H. Mousa, W. Agterof, and J. Mellema. Experimental investigation of the orthokinetic coalescence efficiency of droplets in simple shear flow. *J. Colloid Interf. Sci.*, 240: 340–348, 2001.

[27] P.O. Olapade, R.K. Singh, and K. Sarkar. Pairwise interactions between deformable drops in free shear at finite inertia. *Phys. Fluids*, 21:063302, 2009.

[28] R.K. Singh and K. Sarkar. Effects of viscosity ratio and three dimensional positioning on hydrodynamic interactions between two viscous drops in a shear flow at finite inertia. *Phys. Fluids*, 21:103303, 2009.

[29] K. Sarkar and R.K. Singh. Spatial ordering due to hydrodynamic interaction between a pair of colliding drops in a confined shear. *Phys. Fluids*, 25:051702, 2013.

[30] O. Shardt, J.J. Derksen, and S.K. Mitra. Simulations of droplet coalescence in simple shear flow. *Langmuir*, 29:6201–6212, 2013.

[31] C.K. Aidun and J.R. Clausen. Lattice-Boltzmann method for complex flows. *Annu. Rev. Fluid Mech.*, 42:439–472, 2010.

[32] P.L. Bhatnagar, E.P. Gross, and M. Krook. A model for collision processes in gases. I: Small amplitude processes in charged and neutral one-component system. *Phys. Rev.*, 94:511–525, 1954.

[33] A.J.C. Ladd. Numerical simulations of particulate suspensions via a discretized Boltzmann equation. Part 1. Theoretical foundation. *J. Fluid Mech.*, 271:285–309, 1994.

[34] M. Tjahjadi, H.A. Stone, and J.M. Ottino. Satellite and subsatellite formation in capillary breakup. *J. Fluid Mech.*, 243:297–317, 1992.

[35] D.B. Khismatullin, Y. Renardy, and V. Cristini. Inertia-induced breakup of highly viscous drops subjected to simple shear. *Phys. Fluids*, 15:1351–1354, 2003.

[36] A. Hammerlindl, J. Bowman, and T. Prince. Asymptote: The vector graphics language. `http://asymptote.sourceforge.net/`, 2004–2014.

[37] G. Tryggvason, B. Bunner, A. Esmaeeli, D. Juric, N. Al-Rawahi, W. Tauber, J. Han, S. Nas, and Y.-J. Jan. A front-tracking method for the computations of multiphase flow. *J. Comp. Phys.*, 169:708–759, 2001.

[38] S. Quan, J. Lou, and D.P. Schmidt. Modeling merging and breakup in the moving mesh interface tracking method for multiphase flow simulations. *J. Comp. Phys.*, 228:2660–2675, 2009.

[39] A. Kuzmin, M. Januszewski, D. Eskin, F. Mostowfi, and J.J. Derksen. Simulations of gravity-driven flow of binary liquid in microchannels. *Chem. Eng. J.*, 171:646–654, 2011.

[40] A.K. Chesters. The modelling of coalescence processes in fluid-liquid dispersions: A review of current understanding. *Chem. Eng. Res. Des.*, 69:259–270, 1991.

[41] Y.T. Hu, D.J. Pine, and L.G. Leal. Drop deformation, breakup, and coalescence with compatibilizer. *Phys. Fluids*, 12:484–489, 2000.

[42] U. Sundararaj and C.W. Macosko. Drop breakup and coalescence in polymer blends: The effects of concentration and compatibilization. *Macromolecules*, 28:2647–2657, 1995.

[43] C. D. McAuliffe. Oil-in-water emulsions and their flow properties in porous media. *J. Petrol. Technol.*, 24:727–733, 1973.

[44] D. Jacqmin. Calculation of two-phase Navier-Stokes flows using phase-field modeling. *J. Comput. Phys.*, 155:96–127, 1999.

Simulations of charged droplet collisions in shear flow[1]

5.1 Introduction

Interfaces between fluids are often charged for a variety of reasons[1], such as adsorption of ions and dissociation of acidic groups, and these charges give rise to a wide range of phenomena. For example, air bubbles[2, 3] and oil drops in water[4–6] have a negative charge that depends on the pH of the electrolyte solution they are in. Because of the charge on their surface and the diffuse charge in the electrolyte around them, drops move when external fields are applied[7–11]. Attractive and repulsive forces due to electric interactions between charges on interfaces and ions in the fluid also play an important role in the stability of emulsions against coalescence[1]. In the classic DLVO (Derjaguin and Landau [12] and Verwey and Overbeek [13]) theory, the balance between van der Waals attraction and electric attraction/repulsion on droplets and particles is used to assess the stability of emulsions and particle suspensions. Interactions between interfaces are not limited to electric and van der Waals forces[1]; for example many types of surfactants are used to control interfacial interactions, and they may have molecular structures, such as long hydrocarbon chains, that allow them to interact over longer distances. As a further complication, the distribution of surfactants and charges on an interface may not be uniform[14, 15]. Furthermore, variations in surface tension on interfaces give rise to Marangoni stresses and flows that alter the motion of droplets[16] and the flow between them during collisions[17].

Despite the important role of charge in the interactions between interfaces, simulations of multiphase flow rarely include electric phenomena. In fact, the details of the interactions are usually neglected due to the already considerable computational expense of simulating the flow. In typical simulations, interfaces merge and threads break when their size falls be-

---

[1]A version of this chapter will be submitted to a journal.

low the resolution of the simulation or a specified critical size[18–20]. Since small changes in composition, such as addition of a surfactant or a change in pH, can have a profound effect on macroscopic characteristics of multiphase flows, there is a need to account for the different interactions between interfaces that determine the conditions for the coalescence and breakup of droplets. The ability to perform such detailed simulations of multiphase flows would be relevant to studies of droplet size distributions in turbulent mixing[21, 22] and the behaviour of droplets in micro-scale devices[23]. Working towards this goal, we have coupled a multiphase flow solver with a solver for electrostatic potential to simulate collisions of deforming charged droplets. To our knowledge, simulations of moving charged interfaces and collisions of charged droplets have not been previously reported in the open literature.

The critical conditions for coalescence of *uncharged* droplets in shear flow have been previously studied in experiments with polymers[24–29] and simulations[30] with the free-energy binary-liquid lattice Boltzmann method (LBM)[31]. In general, droplets coalesce unless the capillary number (ratio of viscous and interfacial forces) exceeds a critical value. The phase field method is straightforward to parallelize and has been implemented on graphics processing units (GPUs), whose improved performance relative to conventional CPUs has allowed highly-resolved simulations with droplet radii that span up to 200 lattice nodes. In these simulations, the diffuse interface was sufficiently resolved that the merging of adjacent interfaces was determined by the phase field dynamics rather than the resolution limit of the simulations. We now add electrostatic forces and charged interfaces to the previous simulations of clean interfaces.

While Matsuyama et al. [32] studied the Rayleigh instability[33] of a charged drop, most previous simulations of coupled flow and electric phenomena with LBM have considered the effects of external fields on diffuse charges and interfaces between dielectric media (droplets and their surrounding fluid). For example, Wang et al. [34], Wang and Kang [35], and Lin and Chen [36] used coupled lattice Boltzmann methods to study electroosmotic flow, while Hlushkou et al. [37] coupled a lattice Boltzmann flow solver with a finite difference solver for the potential. Wang et al. [38] studied electroosmotic flow in porous media. The effects of external fields on multiphase flows with interfaces between (leaky) dielectrics have been simulated with the volume-of-fluid[39], level set[40], and phase field[41] methods.

In the sections that follow we describe the relevant theory of electrokinetic phenomena and the numerical methods that have been combined to form the coupled multiphase flow and electrostatic potential solver. We then assess the accuracy of the solver through benchmarks of transient electroosmotic flow in a square channel and the equilibrium pressure in

and around charged and uncharged droplets. Finally, we present and interpret the effects of surface charge on the critical conditions for coalescence of a droplet pair in simple shear flow.

5.2 Theory and numerical models

The simulation method consists of two parts: a multiphase flow solver and a potential solver. Both solvers have been implemented on GPUs. In this work, we use only one GPU, though the methods may also be implemented on clusters of GPUs as has been done for the flow solver[30].

5.2.1 Multiphase flow

The multiphase flow solver provides the solution to the incompressible Navier-Stokes equations, consisting of the usual mass balance and the momentum balance

$$\frac{\partial \vec{u}}{\partial t} + (\vec{u} \cdot \nabla)\vec{u} = -\frac{1}{\rho}\nabla P + \nu \nabla^2 \vec{u} + \frac{1}{\rho}\vec{b} \qquad (5.1)$$

where $\vec{u}$ is the flow velocity, ρ is the fluid density, P is the pressure, ν is the fluid kinematic viscosity, and $\vec{b}$ is the sum of any external forces (per unit volume) acting on the fluid. For simplicity, we consider a pair of fluids with equal densities and viscosities. The composition of the fluid mixture is tracked by the order parameter φ, which varies between -1 and +1, and evolves according to the advection-diffusion equation

$$\frac{\partial \varphi}{\partial t} + \nabla \cdot (\varphi \vec{u}) = M \nabla^2 \mu_\varphi \qquad (5.2)$$

In Eq. 5.2, μ_φ is the local chemical potential of the fluid that depends on the composition φ and its gradient $\nabla \varphi$. The mobility of the phase field is M. We solve this system of equations with the binary-liquid free-energy lattice Boltzmann method[31]. Both the flow and phase field evolution are solved in three dimensions with LBM density distributions that have 19 discrete directions. The phase field is coupled bidirectionally with the flow: the velocity in Eq. 5.2 is obtained from the flow field and the pressure tensor in the momentum balance (Eq. 5.1) is modified to include a thermodynamic component. The resulting pressure is

$$P = \frac{1}{3}\rho - \frac{1}{2}A\varphi^2 + \frac{3}{4}A\varphi^4 \qquad (5.3)$$

where A is a parameter of the free-energy model (terms with gradients of φ have been omitted for simplicity and Eq. 5.3 is therefore only applied far from interfaces). Due to the use of a free energy with two minima, the fluid mixture separates into regions with $\varphi = \pm1$ and interfaces between regions have an excess energy (interfacial tension) σ. The transition in composition across interfaces is smooth, has a characteristic length ℓ_φ, and 99% of the change occurs over the distance $5.3\ell_\varphi$ that may be considered the thickness of the interface. The body force is included in the collision operation of the LBM using the method of He et al. [42]. We note that including the term $\vec{b}\Delta t/(2\rho)$ in the calculation of the physical flow velocity (see e.g. Ref. [43]) is essential for the simulations of electroosmotic flow in which the force is highest where the flow speed is slowest.

For single phase flow simulations, we initialize φ to -1 throughout the domain. In the simulations of sheared droplet pairs, φ is initialized to 1 inside the drops and -1 outside. We allow the interface to smooth out for 100 time steps before starting the shear flow and applying the electrostatic body force.

For the purposes of this chapter, we consider the LB method to provide the velocity, pressure, and phase fields that describe the evolution of the system. The details of the specific method used, and in general the use of lattice Boltzmann methods for computing flows, are available in a wide variety of sources[31, 43–45]. The free-energy LBM we employ has been used to study, for example, droplet formation in microchannels[46] and droplet deformation and breakup in shear[47]. We do not describe the free-energy LBM in further detail, and instead turn our attention to the modelling of electrokinetic phenomena. These effects are coupled with the multiphase flow solver through the body force $\vec{b}$. The nature of the body force, which depends on the electrokinetic phenomena being considered, is described in the next section.

5.2.2 Electrokinetics

The literature on electrokinetic phenomena, which are flow phenomena that occur due to charge, is extensive and has a long history[48]. Near charged surfaces or interfaces, the distribution of ions is determined by the balance between the electrostatic forces on them and their thermal diffusion. The result is an electric double layer (EDL) in which ions with the same charge as the interface are repelled from it, and ions with the opposite charge are attracted. The net charge in the EDL is opposite to the charge of the interface, and it decays with increasing distance from the interface. In electro-neutral systems, the total charges on the interface and in the electrolyte balance. The Poisson equation

$$\varepsilon\nabla^2\psi = -\rho_e \tag{5.4}$$

relates the electrostatic potential ψ to the free charge density ρ_e in a linear dielectric material with permittivity ε. At equilibrium, the concentration of ions is related to the electrostatic potential through the Boltzmann distribution

$$\eta_i = \eta_{i\infty} \exp\left(-\frac{z_i e \psi}{k_B T}\right) \tag{5.5}$$

where η_i is the number density (number per unit volume) of the ith charged component, $\eta_{i\infty}$ is the density in the bulk (far from the interface), z_i is the valence, e is the elementary charge, k_B is the Boltzmann constant, and T is the absolute temperature. We restrict our attention to symmetric $z : z$ electrolytes, with components denoted by $i = +, -$, for which $\eta_{+\infty} = \eta_{-\infty} \equiv \eta_\infty$. It follows that the net free charge density is

$$\rho_e = ez(\eta_+ - \eta_-) = -2ez\eta_\infty \sinh \frac{ze\psi}{k_B T} \tag{5.6}$$

For $\frac{ze\psi}{k_B T}$ sufficiently small, the hyperbolic sine may be linearized as $\sinh \frac{ze\psi}{k_B T} \approx \frac{ze\psi}{k_B T}$. Using this simplification, which is called the Debye-Hückel approximation, and combining Eqs. 5.4 and 5.6 yields the linearized Poisson-Boltzmann equation:

$$\nabla^2 \psi = \kappa^2 \psi \tag{5.7}$$

where

$$\kappa^2 = \frac{2e^2 z^2 \eta_\infty}{\varepsilon k_B T} \tag{5.8}$$

The Debye length κ^{-1} characterizes the thickness of the EDL. We note that under the Debye-Hückel approximation, $\rho_e = -\varepsilon \kappa^2 \psi$, a form that simplifies computations by avoiding the evaluation of the Laplacian of the potential (Eq. 5.4).

Boundary conditions for the electrostatic potential are in general complex due to the adsorption and reaction phenomena that are responsible for surface charges[1]. Two limiting cases are commonly considered[49–51]: a prescribed surface charge or surface potential. We limit our scope to the latter case and consider only the zeta potential ζ, which is the potential at the slip plane that separates the fluid from molecules that stay attached to the surface. Since we study systems that are characterized by only one zeta potential, we normalize the potential by ζ in the numerical solver. In simulations of electroosmotic flow, the zeta potential is imposed on the walls of the channel; in the droplet collision simulations, it is imposed on the liquid-liquid interface.

The electrostatics and flow solvers are coupled through the body force term in Eq. 5.1.

The general form for the body force is

$$\vec{b} = \rho_e \vec{E} \qquad (5.9)$$

where terms due to non-uniform dielectric permittivity and electrostriction have been omitted from the Korteweg-Helmholtz force density[1]. The electric field $\vec{E}$ depends on the problem being considered. For the electroosmotic flow benchmark it is the applied external field and the charge density is determined from the potential ψ. In the simulations of charged droplets, it is electric field in the EDL, $-\nabla\psi$. For these simulations with only internal fields, we include the osmotic pressure of the ions in P (Eq. 5.1). One may alternatively add an osmotic body force, the difference between the two methods being an irrotational body force that can be absorbed into a modified P[52]. For the droplets with constant surface potential that we simulate, the osmotic pressure at their surface is constant and does not contribute a net force on them[51].

We solve Eq. 5.7 on a uniform grid whose points are aligned with the nodes of the LBM flow solver. We discretize the Laplace operator in Eq. 5.7 with a 19 point stencil[43, 53]. This matches the stencil used to compute the Laplacian of the phase field in the free-energy LBM[43]. Discretization provides a system of linear equations, one per grid point, which are solved with the Jacobi iteration method implemented on a GPU. Though other methods, such as successive over-relaxation[54], converge in fewer iterations, the Jacobi method is straightforward to parallelize. At this time, we consider only the Dirichlet type boundary condition $\psi = \zeta$ at various locations in the domain, depending on the system being simulated. When required for the body force term, the gradient of ψ is computed with a 10 point stencil[43].

In the simulations with moving droplet interfaces, we adopt several simplifying assumptions. We assume that the two fluids are perfect dielectrics with equal permittivity (leaky dielectrics have been previously coupled with phase field simulations[41]). No ions are present in the droplets, and we assume that the potential in the external electrolyte evolves quasi-statically. In other words, we assume that the charge distribution relaxes quickly to its equilibrium compared to the time scale of the flow. Without this assumption, a Nernst-Planck advection-diffusion equation would need to be solved for each ion. While this is a reasonable direction for future work, it is not pursued in this chapter. At every time step of the flow solver, we update the location of the interface. This is performed by setting $\psi/\zeta = 1$ in all nodes with $\varphi > 0$ and $\psi/\zeta < 1$ (arbitrarily chosen to be $\psi/\zeta = 0.99$) in any nodes where $\varphi \leq 0$ having previously been > 0. We then iterate the finite-difference solver at all nodes with $\psi/\zeta < 1$ until convergence. Due to the absence of free charge inside the

drops and a fixed potential on their surface, the potential inside the drops is $\psi = \zeta$.

The body force in the droplet simulations is computed at each time step from the updated potential field. Nodes are classified into three groups that have different body forces. In bulk nodes (nodes with $\psi/\zeta < 1$), the body force is $\vec{b} = \varepsilon \kappa^2 \psi \nabla \psi$ (Eq. 5.9 with $\vec{E} = -\nabla \psi$). Droplet nodes, which are nodes with $\psi/\zeta = 1$ that are not adjacent to any nodes with $\psi/\zeta < 1$, have $\vec{b} = 0$. Nodes with $\psi/\zeta = 1$ that are adjacent to at least one node with $\psi/\zeta < 1$ are considered interface nodes. For these nodes, the force per unit area of the interface is distributed over the (unit) volume of the node. This force per unit area is the product of the surface charge density q_s and the average of the internal (zero) and external ($-(\hat{n} \cdot \nabla \psi)\hat{n}$, where $\hat{n}$ is the outward unit normal of the droplet interface) electric fields[55], which may also be derived from the Maxwell stress[1] on a constant-potential surface. The surface charge density is

$$q_s = -\varepsilon \hat{n} \cdot \nabla \psi \tag{5.10}$$

where $\nabla \psi$ is evaluated (infinitesimally) outside the droplet. We compute the surface normal from the gradient of the phase field as $\hat{n} = -\nabla \varphi / ||\nabla \varphi||$, with the negative sign because φ decreases from 1 inside to -1 outside the drop. The body force on surface nodes $\vec{b}_s$ is therefore

$$\vec{b}_s = -\frac{1}{2} \frac{q_s \Delta x^2}{\Delta x^3} (\hat{n} \cdot \nabla \psi)\hat{n} = \frac{\varepsilon}{2\Delta x} (\hat{n} \cdot \nabla \psi)^2 \hat{n} \tag{5.11}$$

where $\Delta x = 1$ is the spacing of the (uniform) computational grid. The gradient of φ (for $\hat{n}$) is computed with a 10 point stencil. The gradient of ψ outside the drop is computed with forward finite differences between the potential of the surface node (ζ) and the potentials at adjacent bulk nodes. If an adjacent bulk node is not available along a coordinate axis, this component of the gradient is taken to be zero.

As an alternative to coupling electrostatics with multiphase flow through a body force, the electrostatic free energy could be added to the free energy of the system[56] and coupled through a modified pressure tensor, like the coupling of the phase field. We expect that this alternative method would increase spurious currents[43], and we therefore use a body force.

5.3 Results and discussion

5.3.1 Benchmarks

Before studying collisions of charged droplets in shear, we evaluate the accuracy of the electrostatic potential solver, the convergence of the coupled solver applied to transient

single-phase electroosmotic flow, and the potential and hydrostatic pressure in and around a stationary drop.

Electrostatic potential in a square channel

We first assess the accuracy of the iterative finite-difference solver for the electrostatic potential. Through this benchmark we select a termination criterion for the iterative solver that is then used in subsequent simulations. Two types of error contribute to the error in the numerical solution: the error due to the discretization of the governing differential equation and the error in the solution of the resulting linear system. The discretization error is controlled by the number of grid points in the EDL. Keeping in mind the goal of simulating droplet collisions, we need a Debye length that is larger than half the interface thickness (≈ 5 lattice nodes) to ensure that droplets interact electrically before their diffuse interfaces overlap and coalesce. For relevance to physical systems, the Debye length must be smaller than the droplet radius, but computational demands limit the maximum droplet radii (relative to the interface thickness and therefore Debye length) that are feasible. Due to these constraints, we select the two Debye lengths $\kappa^{-1} = 15$ and 25 lattice spacings.

The chosen termination criterion for the iterative solver determines the accuracy of the solution to the discretized linear system. Since the electrostatic potential decays to zero over several Debye lengths, a criterion based on the maximum relative change at each node is unreasonable because a significant number of iterations would be required due to nodes where $\psi \to 0$. We therefore pick a maximum absolute change as the termination condition.

Figure 5.1 shows the difference between the numerical and exact solutions for the potential along a line through the centre of a square channel with constant wall potential ζ. Solutions are shown for the two Debye lengths and two channel widths. The square domain has a width $2W$ and covers the region $(y,z) \in (-W,W) \times (-W,W)$. Though the system is two-dimensional, we use the full three-dimensional solver and several (32) layers in the x direction together with periodic boundaries. The series solution for the potential ψ_{exact} is[57]:

$$\psi_{\text{exact}}(y,z) = \zeta \left(1 - \sum_{n=1}^{\infty} \cos\left(\alpha_n \frac{y}{W} \right) f_{\text{n}}\left(\frac{z}{W} \right) \right) \tag{5.12}$$

where

$$\alpha_{\text{n}} = \left(n - \frac{1}{2} \right) \pi$$

$$f_{\text{n}}(z/W) = \frac{a_{\text{n}}(\kappa W)^2}{\gamma_{\text{n}}^2} \left[1 - \frac{\cosh(\gamma_{\text{n}} z/W)}{\cosh(\gamma_{\text{n}})} \right]$$

$$a_{\text{n}} = 2(-1)^{n+1} \alpha_{\text{n}}^{-1}$$

$$\gamma_n = \sqrt{\alpha_n^2 + (\kappa W)^2}$$

We evaluate 75 terms of the series. The initial guess for the numerical solver was $\psi = 0$, and iteration proceeded until the absolute change in ψ/ζ at all nodes was less than 10^{-6} in the last iteration. With this termination criterion, the maximum error between the numerical and exact solutions is between 4×10^{-4} and 2×10^{-3}. The error is lowest $(10^{-5} - 10^{-4})$ near the channel walls. Convergence was reached after approximately 4000 iterations (0.5 seconds in the narrower domain; 1.8 in the wider domain) with $\kappa^{-1} = 15$ and 9000 iterations (1 and 4 seconds) with $\kappa^{-1} = 25$. Significantly more iterations (and time) are needed to improve the accuracy of the solution appreciably, and since the accuracy is high and convergence time is reasonable with the chosen convergence criterion, this criterion was used in the simulations of charged droplet collisions.
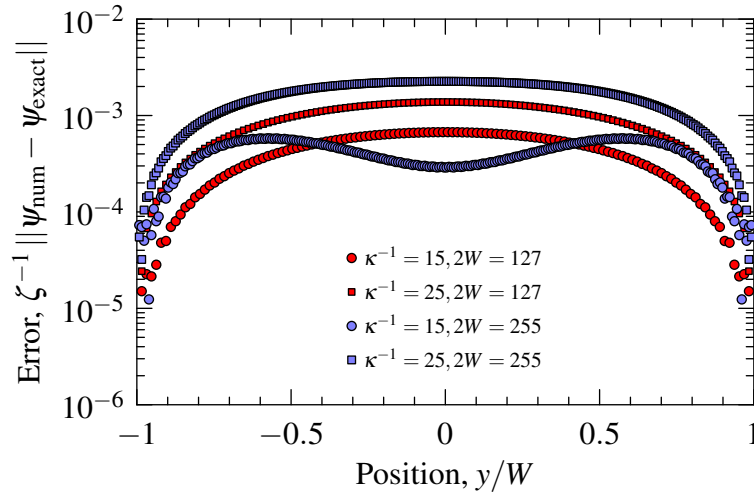
Figure 5.1: Absolute difference between the analytical potential solution ψ_{exact} and the iterative finite-difference solution ψ_{num} for two Debye lengths ($\kappa^{-1} = 15$ and 25 in lattice units) and two domain sizes ($2W = 127$ and 255 also in lattice units) through the centre ($z = 0$) of a cross-section of the square channel.

As a potentially faster alternative to Jacobi iteration, multigrid acceleration[54] was evaluated for the electrostatic potential solver. Although such acceleration provided a significant improvement for the first time step (in which the initial guess is zero throughout the domain), it did not reduce the time required for convergence in subsequent time steps. For multigrid acceleration to be useful in the simulations we perform, the interpolated solution from a coarser mesh must be closer to the solution than the converged solution from the previous time step. Given that flow speeds are necessarily low (measured in lattice spacings per time step) due to the low Mach number constraint in LBM for incompressible flow, only small changes in the position of the interface can occur over one time step. As a

result, the potential from one time step is a good initial guess for the next time step, while the interpolated solution used in multigrid methods is a worse initial guess.

Transient electroosmotic flow

We now examine a transient benchmark of the coupled flow and electrostatics solvers: the starting electroosmotic flow of an initially stationary electrolyte in response to a step change in the applied electric field. The system geometry is the same square channel that was considered in the analysis of the accuracy of the potential solution. An electric field with strength E_x is applied in the x direction and the result is a flow $u(y,z,t)$ parallel to the applied field. The boundary conditions at the walls are $\psi = \zeta$ and $u = 0$. To ensure that the location of the no-slip boundary coincides with the position where the wall zeta potential is specified, i.e. the centre of each lattice node, we use the on-site velocity boundary conditions of Hecht and Harting [58]. The domain is periodic in the x direction.

The series solution for the transient flow is given by Chang and Wang [57]:

$$\tilde{u}_{\text{exact}}(y,z,t) = \frac{\rho \nu}{\varepsilon E_x \zeta} u_{\text{exact}}(y,z,t)$$

$$= \tilde{u}_{e0} - \sum_{m=1}^{\infty} \sum_{n=1}^{\infty} A_{\text{mn}} \cos(\alpha_{\text{n}} y/W) \cos(\beta_{\text{m}} z/W) \exp\left(-\lambda_{\text{mn}} \frac{W^2}{\nu} t\right) \quad (5.13)$$

where $\tilde{u}_{e0}$ is the normalized steady flow speed

$$\tilde{u}_{e0} = 1 - \psi/\zeta = \sum_{n=1}^{\infty} \cos(\alpha_n y/W) f_{\text{n}}(z/W)$$

and

$$A_{\text{mn}} = \frac{2a_{\text{n}}(\kappa W)^2 (-1)^{m+1}}{\beta_{\text{m}}(\beta_{\text{m}}^2 + \gamma_{\text{n}}^2)}$$

$$\beta_{\text{m}} = \left(m - \frac{1}{2}\right)\pi$$

$$\lambda_{\text{mn}} = \alpha_{\text{n}}^2 + \beta_{\text{m}}^2$$

As for the potential solution, 75 terms of each sum were computed.

To evaluate the convergence of the transient solution, we consider the L2 norm of the error between the normalized numerical solution $\tilde{u}_{\text{num}}$ and the exact solution $\tilde{u}_{\text{exact}}$, defined as:

$$E_{\text{L2}}^2(t) = \frac{1}{N_y N_z} \sum_{j=1}^{N_y} \sum_{k=1}^{N_z} \left(\tilde{u}_{\text{num}}(y_j, z_k, t) - \tilde{u}_{\text{exact}}(y_j, z_k, t)\right)^2 \quad (5.14)$$

where N_y and N_z are the number of nodes along the sides of the square ($2W = N_y - 1 = N_z - 1$).

In all simulations, the ratio of the characteristic internal electric field in the EDL and the external applied field was $\kappa\zeta/E_x = 25$. This is the value for a typical physical system with $\zeta = 25$ mV, $\kappa^{-1} = 0.1$ μm, and $E_x = 10$ kV/m. Simulations were performed with two values of $\varepsilon\zeta^2/\rho v^2$ that span the range used in the simulations of droplet collisions: 3.6 and 3.6×10^{-4}. The difference in the L2 error between these two cases was negligible, and we present results only for $\varepsilon\zeta^2/\rho v^2 = 3.6$. With these parameters, the maximum flow speed among all cases is 0.003 l.u., which is sufficiently smaller than the speed of sound in the LBM that the flow can be considered incompressible.

Figure 5.2 demonstrates the second order convergence of the L2 error in the velocity at two times, an early time $\tilde{t} = W^2 t/v = 0.021$ and a late time $\tilde{t} = 2.1$ at which the flow is nearly steady. Intermediate times show the same trends but were omitted for clarity. Simulations were performed for two ratios of the channel width and Debye length, $\kappa W = 2.5$ and 4.2, and three domain sizes: $32 \times 64 \times 64$, $32 \times 128 \times 128$ and $32 \times 256 \times 256$ l.u. (The extent of the domain in the first dimension could be decreased to 1 but was fixed at 32 due to the design of the GPU-based code for large domains.) In simulations with the same domain size, the error is higher with the shorter Debye length. The difference is due to the resolution of the potential (i.e. the number of lattice nodes per Debye length), and the error trends for the two κW values effectively collapse to one line for each time. The L2 error at the later time is about three times higher than the early error. In this convergence study, the exact solution for the potential ψ_{exact} (Eq. 5.12) was used to compute the body force. This choice separates the effects of the termination criterion in the finite-difference solver on the accuracy of the transient flow solution. For comparison, L2 errors for two simulations with the numerical solution ψ_{num} are also shown in Fig. 5.2. In these simulations, which had $32 \times 128 \times 128$ domains and $\kappa^{-1} = 15$ and 25 l.u., the L2 error is nearly the same as with the exact potential solution at the early time and about an order of magnitude higher at the late time. The error with the numerical potential solution, though higher, is satisfactory: the relative errors in the maximum flow speed are between 0.3 and 1%, depending on the time and Debye length. With the exact potential the relative errors are 0.001 to 0.5%.

Stationary droplets

While the previous benchmarks have considered planar boundaries, in this section we evaluate the accuracy of the coupled solvers for stationary droplets. We assess the accuracy in three ways: the potential solution, the pressure field around a solid charged sphere, and the difference in pressure between the inside and outside of a droplet. As before, we consider
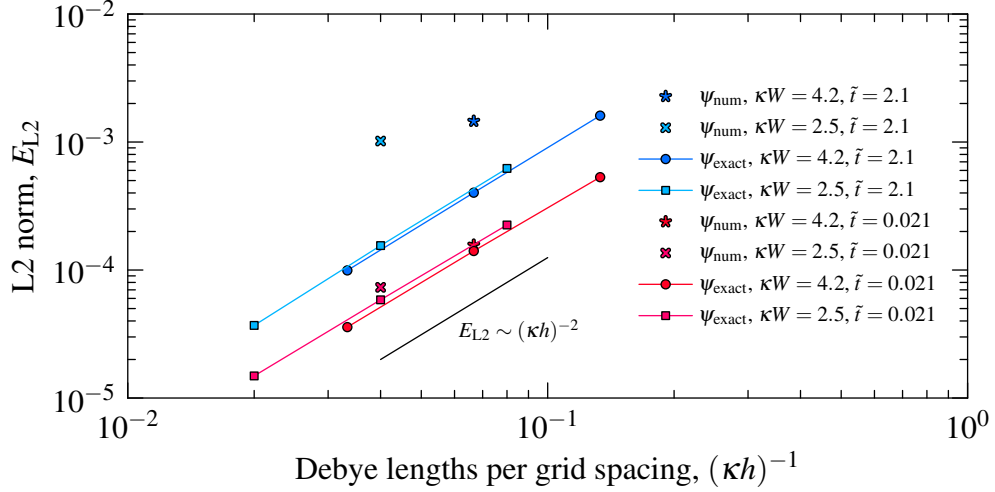
Figure 5.2: Convergence of the electroosmotic flow velocity in the coupled solver at an early time ($\tilde{t} = W^2 t/\nu = 0.021$, red symbols) and near steady state ($\tilde{t} = 2.1$, blue symbols). The exact solution for the potential (ψ_{exact}) was used in the convergence study (circle and square symbols), and for comparison, sample results with the numerical solution for the potential are also shown (star and cross symbols).

the two Debye lengths $\kappa^{-1} = 15$ and 25. Droplets are implemented with a stair-stepped interface. The domains are cubic and periodic.

Figure 5.3 shows the potentials along two lines in cross-sections through a $128 \times 128 \times 128$ domain with a 25 l.u. radius sphere. Solid lines indicate the exact potential outside a sphere of radius R in an infinite domain:

$$\psi(\vec{x}) = \zeta \frac{R}{r} \exp(\kappa(R - r)) \tag{5.15}$$

where $r = ||\vec{x}||$ is the distance of the point $\vec{x}$ from the centre of the sphere ($\vec{x} = 0$). The numerical (periodic domain) and exact (infinite domain) solutions agree well until a distance of one radius from the surface ($2R$ from the centre). The computed potentials along the two lines then deviate from the exact solution, with greater deviation along the line to the closest boundary ($y = 0$). The difference between the numerical and exact potentials is larger, as expected, for the longer Debye length.

The gradient of the potential at the surface is used to compute the surface charge in the droplet simulations. It follows from Eqs. 5.10 and 5.15 that the expected surface charge density q_s is $\varepsilon \zeta (R^{-1} + \kappa)$. Forward finite differences along the two lines underestimate the exact value by at most 14%, with slightly lower error for the shorter Debye length. The error is attributed to the resolution of the Debye length, the finite difference approximation of the derivative, and the finite domain size.
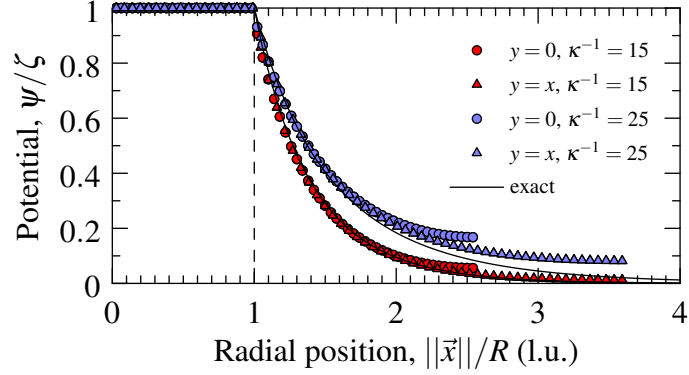
Figure 5.3: Exact (infinite domain, solid line) and numerical (cubic domain, symbols) solutions for the electrostatic potential around a sphere with a 25 l.u. radius in a $128 \times 128 \times 128$ domain. Results are shown for two Debye lengths ($\kappa^{-1} = 15$: red and 25: blue) along two lines in the cross-section through the middle of the sphere: $z = 0, y = 0$ (circles) and $z = 0, y = x$ (triangles).

From the Navier-Stokes momentum balance (Eq. 5.1), the static pressure with the body force $\vec{b} = \varepsilon \kappa^2 \psi \nabla \psi$ satisfies

$$\nabla P = \varepsilon \kappa^2 \psi \nabla \psi \tag{5.16}$$

which may be rewritten as

$$\nabla P = \frac{1}{2} \varepsilon \kappa^2 \nabla \psi^2 \tag{5.17}$$

from which it follows that

$$P - P_{\text{ref}} = \frac{1}{2} \varepsilon \kappa^2 \left(\psi^2 - \psi_{\text{ref}}^2 \right) \tag{5.18}$$

where P_{ref} and ψ_{ref} are a reference pressure and potential at an arbitrary point in the domain. This is the expected dependence of the osmotic pressure with potential[1]. In Fig. 5.4 we examine the relationship between the computed static pressure and potential around a sphere in a periodic cubic domain. The reference point was a corner node of the domain, and pressures were computed along the same lines as in Fig. 5.3 using Eq. 5.3. For the two simulations shown (with Debye lengths 15 and 25 in a $128 \times 128 \times 128$ domain), bounce-back (no slip) boundaries were implemented for the fluid solver for all internodal links that cross the stair-stepped sphere with radius 25 nodes in the centre of the domain. A single-phase flow was simulated outside the solid surface; the multiphase flow solver was used but with φ fixed at -1. The agreement between the numerical and exact dependence of the pressure on the potential is good. The slight offset between the two numerical results and the exact trend is attributed to scatter in the values near the chosen reference point. The results for ε spanning four orders of magnitude were visually indiscernible, and data for

only one value are shown.
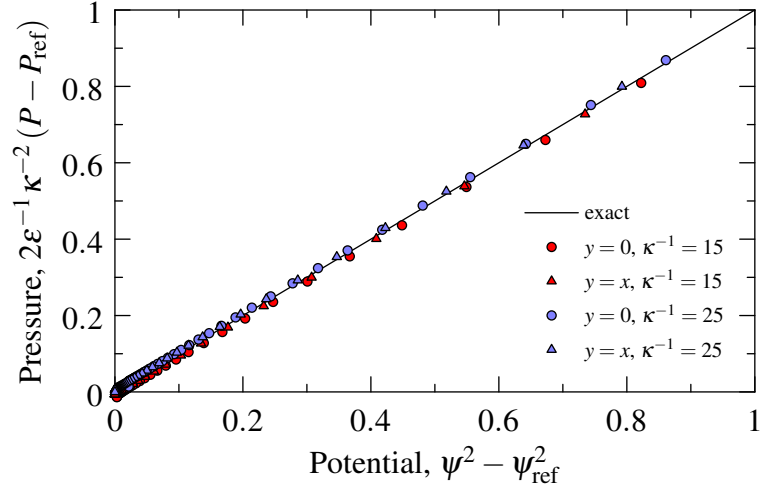
Figure 5.4: Pressure as a function of electrostatic potential at equilibrium in the electrolyte around a charged sphere (radius 25 l.u.) in a periodic cubic domain ($128 \times 128 \times 128$). The symbols show the pressures for two Debye lengths ($\kappa^{-1} = 15$: red, 25: blue) at the same points from a cross-section through the centre of the droplet as in Fig. 5.3. The solid line indicates the expected relationship (Eq. 5.18).

We now replace the solid spherical boundary with a droplet and consider the equilibrium of a charged drop in electrolyte. Using the exact solution for the potential (Eq. 5.15), the spherical shell of interfacial charge experiences an outward electrostatic pressure (the product of the surface charge, Eq. 5.10, and the average of the internal and external electric fields):

$$\frac{1}{2}q_s\left(-\left.\frac{d\psi}{dr}\right|_{r=R^+}\right) = \frac{1}{2}\varepsilon\left.\frac{d\psi}{dr}\right|_{r=R^+}^2 = \frac{\varepsilon\zeta^2}{2R^2}(\kappa R+1)^2 \tag{5.19}$$

The decrease in pressure inside the drop due to the electrostatic pressure is (partially) balanced by the rise in pressure outside the drop. From Eq. 5.18, the pressure at the surface is $\frac{1}{2}\varepsilon\kappa^2\zeta^2$ higher than infinitely far from the surface. The total difference in pressure between the inside and outside of a drop may be expressed as the sum of the usual Laplace pressure ΔP_φ and the electrostatic contribution ΔP_ψ such that

$$\Delta P = \Delta P_\varphi + \Delta P_\psi \tag{5.20}$$

where the two components of the pressure change are

$$\Delta P_\varphi = \frac{2\sigma}{R} \tag{5.21}$$

110

and

$$\Delta P_\psi = \frac{1}{2}\varepsilon\kappa^2\zeta^2 - \frac{\varepsilon\zeta^2}{2R^2}(\kappa R + 1)^2 = -\frac{\varepsilon\zeta^2}{2R^2}(2\kappa R + 1) \tag{5.22}$$

We may define an effective interfacial tension $\sigma_{\text{net}} = \frac{1}{2}R\Delta P$ that leads to

$$\sigma_{\text{net}} = \sigma - \frac{\varepsilon\zeta^2}{4R}(2\kappa R + 1) \tag{5.23}$$

In the limit of a small Debye length relative to the drop radius ($\kappa R \gg 1$), the decrease in the interfacial tension is $\frac{1}{2}\varepsilon\kappa\zeta^2$. For physical parameters that create a large decrease (for example, the permittivity of water, a $0.1~\mu$m Debye length, and a 100 mV zeta potential), the decrease is 35 μN/m, a small fraction of typical mN/m interfacial tensions. (We note that with a 100 mV zeta potential, the Debye-Hückel approximation no longer holds.)

In the simulations, we consider a wide range of strengths of the electrostatic interactions. We therefore evaluate the accuracy of the pressure difference between the interior of a drop and its surroundings. For this benchmark, we consider a stationary drop with phase field parameters that match the simulations of uncharged collisions with a capillary number of 0.15 and a 25 l.u. drop radius. Keeping the phase field parameters constant, simulations with droplet radii of 25, 37.5, and 50 l.u. were performed in periodic cubic domains with 128, 192, and 256 l.u. sides. For each drop radius, three simulations were performed: one without charge, one with $\kappa^{-1} = 15$ l.u., and one with $\kappa^{-1} = 25$. In the charged simulations, $\varepsilon\kappa\zeta^2/\sigma$ was 0.9 with $\kappa^{-1} = 15$ and 0.53 with $\kappa^{-1} = 25$. The pressure difference at steady state between the centre of the drop and the corner of the domain is shown in Fig. 5.5. Excellent agreement is seen in the uncharged cases. In the charged cases, the pressure differences are consistently overestimated by at most 10% (for $\kappa^{-1} = 25$) and 35% (for $\kappa^{-1} = 15$). Though the agreement appears to be better for the larger Debye length, this is only true for the pressure difference: the relative error in the decrease in pressure from the uncharged cases is consistently near 30%. Considering the 14% error in the computation of the surface charge density, the higher error in the pressure difference is attributed to the error in the other factors in the force on interface nodes: the finite difference approximations of the potential gradient and surface normal. While the parameters of this benchmark were chosen to examine the decrease in pressure difference, the decrease in pressure from the uncharged case is negligible at the conditions of most of the simulations we present in the section that follows. However, the possibility of errors up to 30% in the forces on the droplet interfaces should be kept in mind in the interpretation of the results.

In diffuse interface methods, spurious currents are present at static equilibrium. With the high body forces used in the pressure benchmark, the maximum spurious speed was
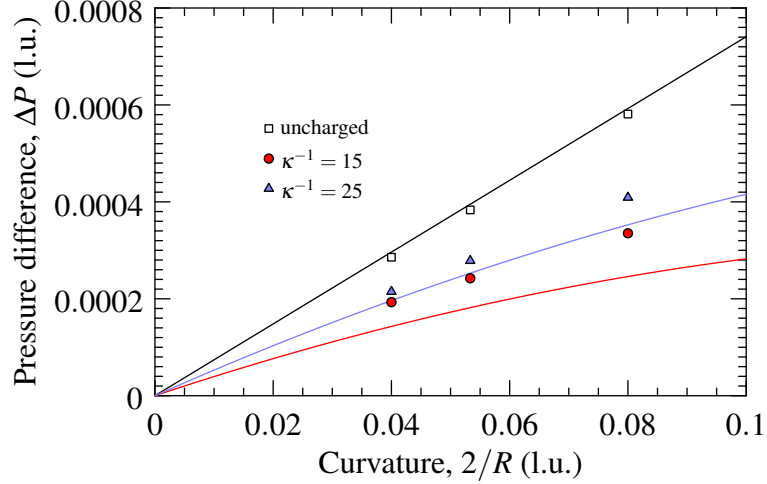
Figure 5.5: Difference between the internal and external pressures for drops with increasing curvature $2/R$. The expected relationship (solid lines, Eq. 5.20) and simulation results (symbols) are shown for uncharged (black squares) and charged drops with two Debye lengths ($\kappa^{-1} = 15$: red circles, 25: blue triangles).

3.8×10^{-4} (l.u.) while the average in a cross-section through the droplet was 1.5×10^{-5} for the worst case. In the simulations without charge, the maximum speed was 2.8×10^{-5} and the average was 1.1×10^{-6}. To assess the magnitude of these spurious currents, we compare them with the characteristic shear speed $\dot{\gamma}R$, where $\dot{\gamma}$ is the shear rate, of the collision simulations we perform at the same conditions. For the worst charged case, the maximum spurious speed is 5% of $\dot{\gamma}R$, and the average spurious speed is 0.2% of $\dot{\gamma}R$. In comparison, the maximum and average spurious speeds are 0.4% and 0.02%, respectively, in simulations without electric body forces. Though spurious currents are an order of magnitude higher in the simulations with charge, they are low compared to the flow speeds we impose to shear the droplets.

We briefly point out that the pressure change given by Eq. 5.20 is negative when the electrostatic contribution exceeds the contribution from the phase field. Such cases are easy to implement in the simulations by specifying a sufficiently low interfacial tension. Under these conditions, the interface is unstable, and the drop breaks apart. This outcome is similar to the Rayleigh instability of charged drops in air[32, 33], but we do not study this phenomenon in electrolytes further.

Overall, the benchmark simulations indicate high accuracy for the potential solution and coupling with the flow. Errors in the finite difference calculations of surface charges and therefore forces on interfaces are more significant, but this error is small compared to the range of electric force strengths, which spans several orders of magnitude, that we consider next in the simulations of droplet collisions.

5.3.2 Droplet collisions

Simulations of collisions between charged droplets in shear were performed to determine the effects of varying strengths of the electrostatic repulsion on the critical conditions for coalescence. These simulations were performed under conditions identical to those in our previous study of uncharged droplets[30]. Two shear planes moving in opposite directions are separated by a height H (in y, the velocity gradient direction) in a domain with a width $W = H$ (in z, the vorticity direction) and a length $L = 2H$ (in x, the shear direction). Two droplets with radius R are placed in the middle of the domain, with their centres separated by a vertical offset $\Delta Y/(2R) = 0.86$ and a horizontal distance $\Delta X/(2R) = 1.26$. The confinement of the drops is $2R/H = 0.39$. The two fluids have equal densities and viscosities. The domain is periodic in the x direction, and reflection boundary conditions are specified at the ends of the domain in the z direction. On the shear planes, the flow velocity is the shear velocity, and a reflection condition is used for the phase field. For the simulations with charge, the potential is periodic in the x direction and has reflection (zero charge) conditions on the other planes. As before[30], we use internal symmetry and rotational symmetry boundary conditions through the centres of the drops to reduce the computed domain size to one quarter of the full $L \times W \times H$ system.

In all simulations of droplet collisions in shear, the shear rate $\dot{\gamma}$ was specified such that the Reynolds number was $\mathrm{Re} = \frac{\dot{\gamma}R^2}{\nu} = 1$. The phase field parameters were chosen to have well-resolved interfaces with $\ell_\varphi = 2$. When interfaces are resolved, coalescence is a consequence of the dynamics of the phase field rather than inadequate resolution of interfaces and films between drops[30]. The Péclet number that characterizes the phase field mobility (M in Eq. 5.2) was fixed at 10. The interfacial tension between the drop and bulk phases was varied to study the effect of the capillary number $\mathrm{Ca} = \frac{\rho\nu\dot{\gamma}R}{\sigma}$.

Droplets coalesce unless the capillary number exceeds a critical value that is affected by the ratio of the drop radius and interface thickness[30]. For fixed capillary and Reynolds numbers, a larger radius relative to the interface thickness suppresses coalescence. Therefore, critical capillary numbers decrease with increasing R/ℓ_φ. The rate of this decrease was has been previously studied[30] by performing simulations with increasing droplet (and domain) sizes while keeping the interface thickness constant. We now study the effects of electrostatic repulsion on the relationship between the critical capillary number and droplet size.

The inclusion of electrostatic interactions between charged droplets through an electrolyte introduces two non-dimensional parameters. The first parameter is the ratio of the Debye length and a characteristic length for which two choices are meaningful: the drop

radius and interface thickness. The resulting ratios are κR and $\kappa \ell_\varphi$, respectively. For the second parameter, which characterizes the strength of electric forces, we choose the ratio of electric and viscous forces $\frac{\varepsilon \zeta^2}{\rho v^2}$. In the simulation parameter space, the zeta potential, density, and viscosity are all fixed, leading to $\frac{\varepsilon \zeta^2}{\rho v^2} = 36\varepsilon$. While in physical experiments the strength of electric interactions usually varies due to ζ, in the simulations potentials are normalized with respect to ζ and we vary ε.

Figure 5.6 illustrates sample collisions between uncharged and charged droplets at otherwise identical conditions. In these simulations, the droplet radius was 50 l.u., the largest we consider in this work, and the computed domain was $512 \times 128 \times 128$. Running on one NVIDIA Tesla M2070 GPU, the uncharged simulation completed 240000 time steps in 16 hours at a speed of 34.9 million lattice updates per second (Mlups). The speed of simulations with charge depends on the number of iterations required for the potential to converge. For the charged simulation shown in Fig. 5.6, the effective speed was 2.8 Mlups with an average of 147 iterations of the potential solver at each time step. Though 12.5 times slower than the uncharged simulation, this simulation running on a GPU is faster than an implementation of the free-energy LBM (without charge) on 8 conventional CPUs that ran at 2 Mlups[47]. Comparing the outcomes of the two simulations in Fig. 5.6, we see that the repulsion between the charged droplets prevents coalescence at the chosen capillary number.

Ca = 0.06, $R/\ell_\varphi = 25$, uncharged

Ca = 0.06, $R/\ell_\varphi = 25$, $\kappa R = 3.33$, $\frac{\varepsilon \zeta^2}{\rho v^2} = 0.036$
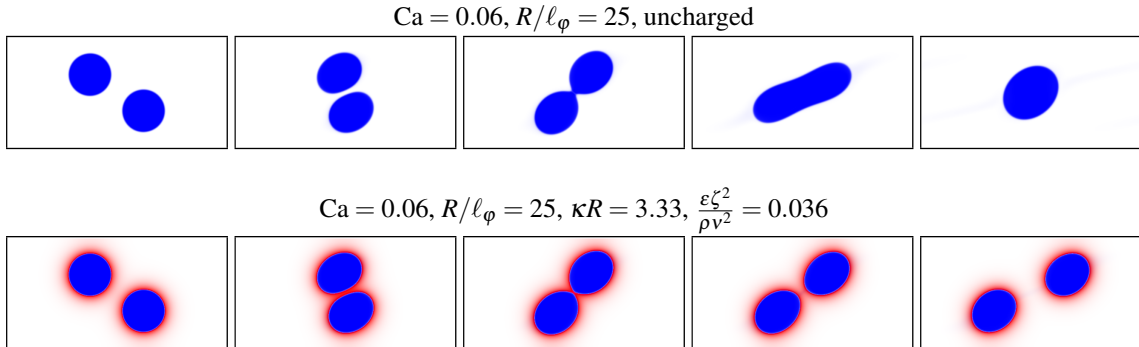
Figure 5.6: Sample collisions of uncharged (upper sequence) and charged (lower sequence) droplets. The colour ranges from white ($\varphi = -1$) to blue ($\varphi = 1$) for the phase field and white ($\psi = 0$) to red ($\psi = \zeta$) for the potential outside the drops.

The effects of the Debye length and the strength of the electrostatic interactions on the outcomes of droplet collisions are shown in Fig. 5.7. To imitate physical experiments with the same fluid system and increasing droplet radii, the Debye length was kept constant while the droplet radius and domain size were increased in the same proportion. Simulations were performed with $\frac{\varepsilon \zeta^2}{\rho v^2}$ from 3.6×10^{-4} to 3.6 (based on choosing ε from 10^{-5} to

10^{-1} in lattice units). The simulations of uncharged collisions were repeated (instead of using previous results[30]) to include an equilibration delay because the simulations with charge included a short delay for interface equilibration before shearing is started. As would be expected, this delay did not change the critical capillary numbers. At the conditions of the simulations, two critical capillary numbers separate the capillary number ranges for three possible outcomes. Below the lower critical capillary number, the droplets coalesce, while above the upper critical capillary number the droplets slide over each other. Between the two critical Ca, the interfaces of the droplets temporarily merge, but the bridge breaks because the drops are sheared apart faster than the bridge grows[30]. Capillary numbers were systematically searched until the range of each critical capillary number was narrowed to 0.005. In the cases with the strongest electric interactions, coalescence was not observed, and a symbol is shown for the lowest capillary number that could be simulated before numerical instability occurred. This instability is attributed to the high interfacial tensions needed to achieve low capillary numbers.

Figure 5.7 shows that the critical capillary numbers for coalescence shift downward with increasing $\varepsilon \zeta^2 / \rho v^2$ and the decrease is smaller for the longer Debye length. This means that a slower shear rate is needed to coalesce charged drops than uncharged drops. To interpret these outcomes, we consider the force per unit area f_p on two parallel plates with equal potential separated by a distance d[1]:

$$f_\mathrm{p} = \frac{\varepsilon \kappa^2 \zeta^2}{2 \cosh^2(\kappa d/2)} \tag{5.24}$$

For a compressed pair of colliding droplets, we choose a separation distance equal to the thickness of the phase field interface, $d = 5\ell_\varphi = 10$ l.u.. At this separation, f_p is maximum when $\kappa^{-1} \approx 0.42d = 4.2$ l.u. and decreases with increasing Debye length (decreasing κ). This explains the weaker repulsion of droplets with thicker EDLs. Due to the flattening of drops during collisions (Fig. 5.6), we estimate the force on the drops as $\pi R^2 f_\mathrm{p}$ rather than being proportional to $\pi R \varepsilon \kappa \zeta^2$ for spheres in the Derjaguin limit[1]. To determine when electrostatic forces affect droplet collisions, we therefore compare f_p with the viscous stress $\rho v \dot{\gamma}$ and form the ratio

$$\frac{\varepsilon \kappa^2 \zeta^2}{\rho v \dot{\gamma}} \tag{5.25}$$

We have omitted the proportionality constant $\frac{1}{2}$ and also the factor $\cosh^2(\kappa d/2)$ because $\cosh(\kappa d/2) \approx 1$ for the parameters we consider. As shown in Fig. 5.8, the critical capillary number decreases as this ratio increases. Electrostatic forces change the critical capillary numbers for coalescence once $\frac{\varepsilon \kappa^2 \zeta^2}{\rho v \dot{\gamma}} \approx 1$. With increasing R and fixed physical properties,
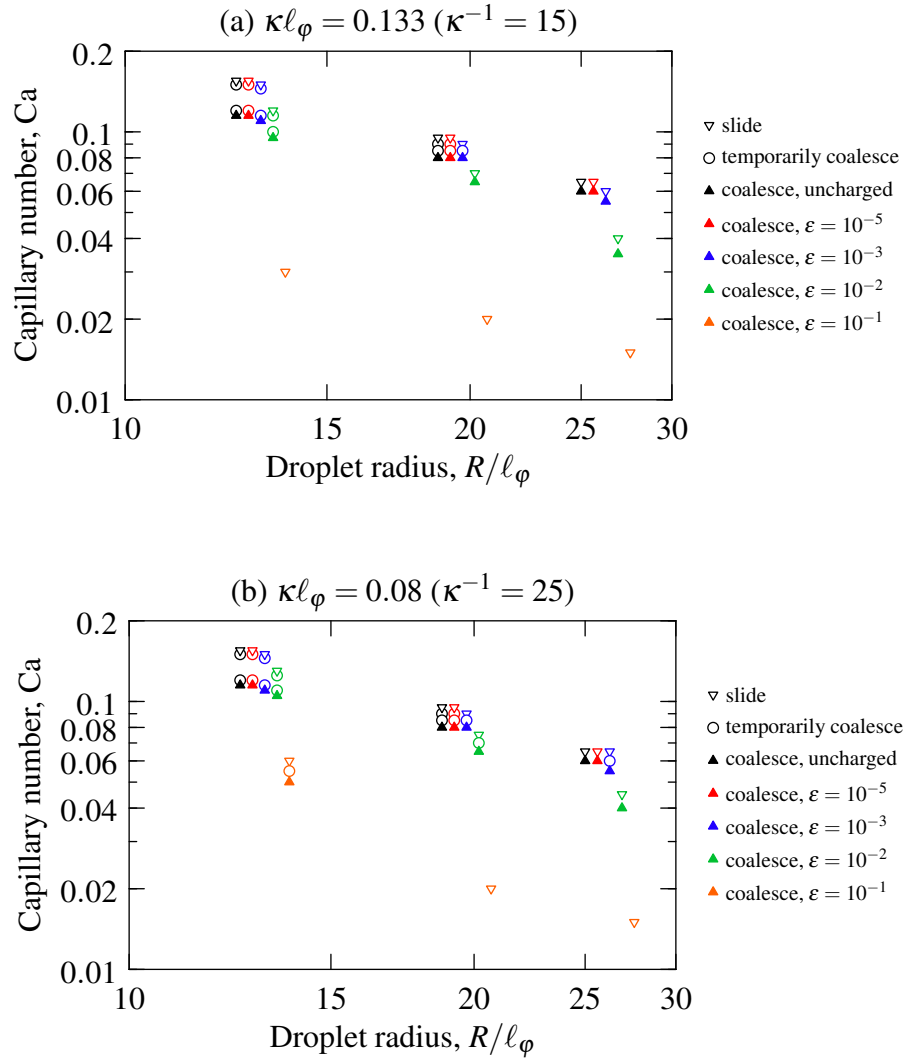
Figure 5.7: Outcomes of binary droplet collisions at varying capillary numbers Ca, droplet radii R relative to the characteristic interface thickness ℓ_φ, and several strengths of the electrostatic interactions (uncharged and κ^{-1} = (a) 15 and (b) 25 l.u. with $\varepsilon = 10^{-1}, 10^{-2}, 10^{-3}, 10^{-5}$ l.u.). In each cluster of data points with different ε, the radius is the same as in the uncharged case, but the symbols have been offset horizontally to separate them. Only the simulation results that are closest to a critical capillary number are shown: open triangles indicate the lowest capillary number at which sliding was observed, open circles indicate capillary numbers at which coalescence is temporary, and filled triangles indicate the highest capillary numbers at which the droplets coalesce.

the maximum shear rate for coalescence decreases and the relative magnitude of electric forces at near critical conditions increases. Presumably, sufficiently large droplets cannot coalesce because electric repulsion is too high compared to shear stress at the low shear rates required for coalescence. In the simulations, we resolve the Debye length (and interface thickness), and the droplets are not large enough to study the behaviour at this limit. In fact, considering the high critical capillary numbers at a high initial vertical offset between the drops (in comparison with experiments[28]), the droplets we simulate are quite small.
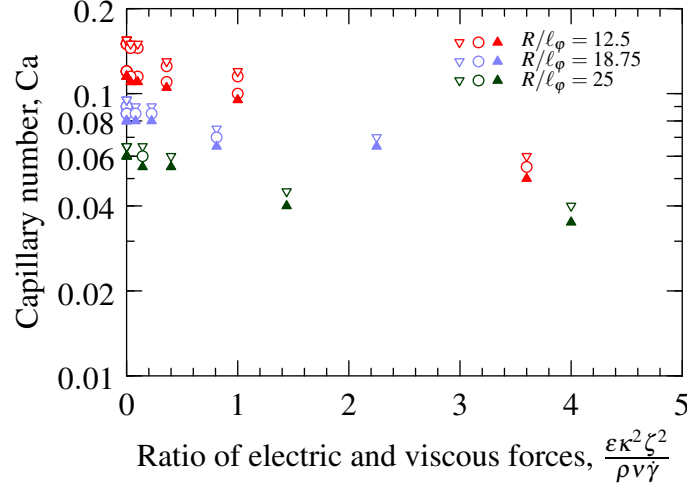
Figure 5.8: Effect of the ratio of electric and viscous forces on the critical capillary numbers for coalescence. The symbols have the same meaning as in Fig. 5.7 but are coloured by the droplet radius: $R/\ell_\varphi = 12.5$ in red, $R/\ell_\varphi = 18.75$ in blue, and $R/\ell_\varphi = 25$ in green.

To compare the simulations with an aqueous system, we first estimate the physical size of the droplets through the ratio of the droplet radius and minimum stable film thickness before coalescence, estimated to be $3\ell_\varphi = 6$ l.u. for simulations with uncharged interfaces[30]. Taking a physical critical film thickness on the order of 10 nm, the physical radius of the $R = 25$ l.u. droplets is estimated to be 42 nm, and 83 nm for the drops with $R = 50$ l.u., both in the range of microemulsions[59]. The Debye lengths are then 25 nm and 42 nm for $\kappa^{-1} = 15$ l.u. and 25, respectively, which are reasonable for dilute aqueous systems[1]. Using the larger drop radius and shorter Debye length with the permittivity, density, and viscosity of water, the condition for a noticeable change in critical capillary numbers becomes

$$\frac{\varepsilon \kappa^2 \zeta^2}{\rho \nu \dot{\gamma}} \approx 1 \Rightarrow \zeta \approx 360 \text{ mV} \tag{5.26}$$

which is higher than typical zeta potentials, e.g. up to $|\zeta| = 120$ mV for hexane in 1 mM KCl solution[6]. At these high zeta potentials the Debye-Hückel approximation becomes poor, and the effects of finite ion size need to be considered[1]. In comparison, the required

potential is 25 mV for a droplet with $R = 1.2$ μm at the same conditions.

For the points shown in Figs. 5.7 and 5.8, the difference between σ and σ_{net} is at most 20% for the three points with $\varepsilon = 0.1$, less than 5% for the points with $\varepsilon = 0.01$, and less than 1% for all other points. The change in the conditions for coalescence cannot therefore be attributed to changes in the effective interfacial tension of the drops and therefore their capillary numbers. The 30% error in the electrostatic forces noted in the benchmark of the steady pressure difference is not expected to have a significant impact on the interpretation of the results because the error is small compared to the range of the electric forces that span four orders of magnitude.

The colliding droplets in the simulations have constant surface potentials. Since surface charges are proportional to the local normal potential gradient, surface charges decrease as the proximity to another (equal potential) interface decreases. Such a decrease in charge on approaching interfaces would not occur with constant-charge interfaces, causing a stronger repulsion between the droplets. Simulations with constant surface charge and other charge regulation models[1, 50] are areas for future investigation.

5.4 Concluding remarks

Simulations of charged droplet collisions in shear were performed by coupling a phase field method for two-component flows with an iterative finite difference solver for the electrostatic potential in the EDL around the deforming drops. A benchmark study of transient electroosmotic flow in a square channel was used to assess the accuracy of the coupled solvers for single phase flow. A static benchmark of the pressure differences across charged and uncharged droplet interfaces was used to evaluate the accuracy of the forcing in the multiphase solver.

Collisions of droplets with constant surface potential and electric forces spanning four orders of magnitude were performed to determine the effect of surface charges on the critical conditions for coalescence. The main result is that critical capillary numbers for coalescence decrease with increasing strength of electric forces, and the extent of this decrease was determined. The change in critical capillary numbers begins once electric forces are comparable to viscous forces. The decrease in critical capillary numbers is greater for shorter Debye lengths. Since the simulations resolve the Debye length and the film between the droplets, the droplet radii are only several times larger than these length scales. Consequently, the effective physical radii of the droplets we simulate are between 10 and 100 nm, as found in microemulsions. For droplets of this size in the simulated conditions, electric repulsion is weak compared to shear forces. In common systems, which have larger

droplets and lower shear rates, electric repulsion would be more significant.

Several areas for future work are available towards the goals of developing accurate simulations of the electric phenomena that contribute to interfacial interactions in multi-phase flows and understanding their impact on larger scales of such flows. The reasons for the error in the calculation of the force on the charged interface need to be examined and corrected. The simulations may be developed further by solving the non-linear Poisson-Boltzmann equation, including external electric fields and modelling leaky dielectrics[41], solving Nernst-Planck advection-diffusion equations for ion concentrations, and implementing constant surface charge and charge regulation boundary conditions on fluid interfaces. To be able to simulate droplet sizes that are more relevant to typical droplet flows, the simulations methods can be adapted to use multiple GPUs in parallel, as has been done for simulations without charge[30]. Simulations with larger droplets and large domains could be used to study droplet interactions in a flowing emulsion. The simulation methods may also be adapted to study other electric phenomena in fluids, such as the Rayleigh instability, droplet electrophoresis, and electrowetting.

References

[1] Jacob H. Masliyah and Subir Bhattacharjee. *Electrokinetic and Colloid Transport Phenomena*. Wiley-Interscience, 2006.

[2] H.A. McTaggart. The electrification at liquid-gas surfaces. *Philos. Mag.*, 27:297–314, 1914.

[3] J.K. Beattie, A.M. Djerdjev, and G.G. Warr. The surface of neat water is basic. *Faraday Discuss.*, 141:31–39, 2009.

[4] J.C. Carruthers. The electrophoresis of certain hydrocarbons and their simple derivatives as a function of pH. *T. Faraday Soc.*, 34:300–307, 1938.

[5] W. Dickinson. The effect of pH upon the electrophoretic mobility of emulsions of certain hydrocarbons and aliphatic halides. *T. Faraday Soc.*, 37:140–148, 1941.

[6] J. Liu, Z. Zhou, and Z. Xu. Electrokinetic study of hexane droplets in surfactant solutions and process water of bitumen extraction systems. *Ind. Eng. Chem. Res.*, 41: 51–57, 2002.

[7] M. Mooney. Variations in the cataphoretic mobilities of oil drops in water. *Phys. Rev.*, 23:396–411, 1924.

[8] F. Booth. The cataphoresis of spherical fluid droplets in electrolytes. *J. Chem. Phys.*, 19:1331–1336, 1951.

[9] A.J. Taylor and F.W. Wood. The electrophoresis of hydrocarbon droplets in dilute solutions of electrolytes. *T. Faraday Soc.*, 53:523–529, 1957.

[10] S. Levine and R.N. O'Brien. A theory of electrophoresis of charged mercury drops in aqueous electrolyte solution. *J. Colloid Interf. Sci.*, 43:616–629, 1973.

[11] J.C. Baygents and D.A. Saville. Electrophoresis of drops and bubbles. *J. Chem. Soc. Faraday Trans.*, 87:1883–1898, 1991.

[12] B.V. Derjaguin and L. Landau. Theory of the stability of strongly charged lyophobic sols and of the adhesion of strongly charged particles in solution of electrolytes. *Acta Physicochim. (URSS)*, 14:633–662, 1941.

[13] E.J.W. Verwey and J.Th.G. Overbeek. *Theory of the Stability of Lyophobic Colloids*. Elsevier, 1948.

[14] J. Drelich, J. Long, and A. Yeung. Determining surface potential of the bitumen-water interface at nanoscale resolution using atomic force microscopy. *Can. J. Chem. Eng.*, 85:625–634, 2008.

[15] P. Esmaeili, F. Lin, and A. Yeung. Stability of emulsified heavy oil: The combined effects of deterministic DLVO forces and random surface charges. *Langmuir*, 28: 4948–4954, 2012.

[16] D.A. Saville. The effects of interfacial tension gradients on the motion of drops and bubbles. *Chem. Eng. J.*, 5:251–259, 1973.

[17] H. Liu and Y. Zhang. Phase-field modeling droplet dynamics with soluble surfactants. *J. Comput. Phys.*, 229:9166–9187, 2010.

[18] G. Tryggvason, B. Bunner, A. Esmaeeli, D. Juric, N. Al-Rawahi, W. Tauber, J. Han, S. Nas, and Y.-J. Jan. A front-tracking method for the computations of multiphase flow. *J. Comp. Phys.*, 169:708–759, 2001.

[19] S. Quan, J. Lou, and D.P. Schmidt. Modeling merging and breakup in the moving mesh interface tracking method for multiphase flow simulations. *J. Comp. Phys.*, 228:2660–2675, 2009.

[20] G. Tryggvason, R. Scardovelli, and S. Zaleski. *Direct Numerical Simulations of Gas-Liquid Multiphase Flows*. Cambridge University Press, 2011.

[21] C. Tsouris and L.L. Tavlarides. Breakage and coalescence models for drops in turbulent dispersions. *AIChE J.*, 40:395–406, 1994.

[22] P. Perlekar, L. Biferale, M. Sbragaglia, S. Srivastava, and F. Toschi. Droplet size distribution in homogeneous isotropic turbulence. *Phys. Fluids*, 24:065101, 2012.

[23] V. Cristini and Y.-C. Tan. Theory and numerical simulation of droplet dynamics in complex flows — a review. *Lab Chip*, 4:257–264, 2004.

[24] Y.T. Hu, D.J. Pine, and L.G. Leal. Drop deformation, breakup, and coalescence with compatibilizer. *Phys. Fluids*, 12:484–489, 2000.

[25] H. Yang, C.C. Park, Y.T. Hu, and L.G. Leal. The coalescence of two equal-sized drops in a two-dimensional linear flow. *Phys. Fluids*, 13:1087–1106, 2001.

[26] L.G. Leal. Flow induced coalescence of drops in a viscous fluid. *Phys. Fluids*, 16: 1833–1851, 2004.

[27] Y. Yoon, M. Borrell, C.C. Park, and L.G. Leal. Viscosity ratio effects on the coalescence of two equal-sized drops in a two-dimensional linear flow. *J. Fluid Mech.*, 525: 355–379, 2005.

[28] D. Chen, R. Cardinaels, and P. Moldenaers. Effect of confinement on droplet coalescence in shear flow. *Langmuir*, 25:12885–12893, 2009.

[29] P. De Bruyn, R. Cardinaels, and P. Moldenaers. The effect of geometrical confinement on coalescence efficiency of droplet pairs in shear flow. *J. Colloid Interf. Sci.*, 409: 183–192, 2013.

[30] O. Shardt, J.J. Derksen, and S.K. Mitra. Simulations of droplet coalescence in simple shear flow. *Langmuir*, 29:6201–6212, 2013.

[31] A.J. Briant and J.M. Yeomans. Lattice Boltzmann simulations of contact line motion. II. Binary fluids. *Phys. Rev. E*, 69:031603, 2004.

[32] T. Matsuyama, T. Abe, and H. Yamamoto. Lattice Boltzmann method study of rayleigh instability of a charged droplet. *Advanced Powder Technol.*, 18:93–104, 2007.

[33] Lord Rayleigh. On the equilibrium of liquid conducting masses charged with electricity. *Philos. Mag.*, 14:184–186, 1882.

[34] J. Wang, M. Wang, and Z. Li. Lattice Poisson-Boltzmann simulations of electroosmotic flows in microchannels. *J. Colloid Interf. Sci.*, 296:729–736, 2006.

[35] M. Wang and Q. Kang. Modeling electrokinetic flows in microchannels using coupled lattice Boltzmann methods. *J. Comput. Phys.*, 229:728–744, 2010.

[36] T.-Y. Lin and C.-L. Chen. Analysis of electroosmotic flow with periodic electric and pressure fields via the lattice-Poisson-Boltzmann method. *Appl. Math. Model.*, 37: 2816–2829, 2013.

[37] D. Hlushkou, D. Kandhai, and U. Tallarek. Coupled lattice-boltzmann and finite-difference simulation of electroosmosis in microfluidic channels. *Int. J. Numer. Meth. Fluids*, 46:507–532, 2004.

[38] M. Wang, N. Pan, J. Wang, and S. Chen. Lattice Poisson-Boltzmann simulations of electroosmotic flows in charged anisotropic porous media. *Communications in Computational Physics*, 2:1055–1070, 2007.

[39] J.M. López-Herrera, S. Popinet, and M.A. Herrada. A charge-conservative approach for simulating electrohydrodynamic two-phase flows using volume-of-fluid. *J. Comput. Phys.*, 230:1939–1955, 2011.

[40] K.E. Teigen and S.T. Munkejord. Influence of surfactant on drop deformation in an electric field. *Phys. Fluids*, 22:112104, 2010.

[41] Y. Lin, P. Skjetne, and A. Carlson. A phase field model for multiphase electro-hydrodynamic flow. *Int. J. Multiphase Flow*, 45:1–11, 2012.

[42] X. He, Q. Zou, L.-S. Luo, and M. Dembo. Analytic solutions of simple flows and analysis of nonslip boundary conditions for the lattice Boltzmann BGK model. *J. Stat. Phys.*, 87:115–136, 1997.

[43] C.M. Pooley and K. Furtado. Eliminating spurious velocities in the free-energy lattice Boltzmann method. *Phys. Rev. E*, 77:046702, 2008.

[44] S. Chen and G.D. Doolen. Lattice Boltzmann method for fluid flows. *Annu. Rev. Fluid Mech.*, 30:329–364, 1998.

[45] C.K. Aidun and J.R. Clausen. Lattice-Boltzmann method for complex flows. *Annu. Rev. Fluid Mech.*, 42:439–472, 2010.

[46] S. van der Graaf, T. Nisisako, C.G.P.H. Schroën, R.G.M. van der Sman, and R.M. Boom. Lattice Boltzmann simulations of droplet formation in a T-shaped microchannel. *Langmuir*, 22:4144–4152, 2006.

[47] A.E. Komrakova, O. Shardt, D. Eskin, and J.J. Derksen. Lattice Boltzmann simulations of drop deformation and breakup in shear flow. *Int. J. Multiphase Flow*, 59: 24–43, 2014.

[48] S. Wall. The history of electrokinetic phenomena. *Curr. Opin. Colloid In.*, 15:119–124, 2010.

[49] S.L. Carnie and D.Y.C. Chan. Interaction free energy between identical spherical colloidal particles: The linearized Poisson-Boltzmann theory. *J. Colloid Interf. Sci*, 155:297–312, 1993.

[50] S.L. Carnie, D.Y.C. Chan, and J. Stankovich. Computation of forces between spherical colloidal particles: Nonlinear Poisson-Boltzmann theory. *J. Colloid Interf. Sci*, 165:116–128, 1994.

[51] P.K. Das, S. Bhattacharjee, and W. Moussa. Electrostatic double layer force between two spherical particles in a straight cylindrical capillary: Finite element analysis. *Langmuir*, 19:4162–4172, 2003.

[52] T.M. Squires and M.Z. Bazant. Induced-charge electro-osmosis. *J. Fluid Mech.*, 509: 217–252, 2004.

[53] M. Dowle, R.M. Mantel, and D. Barkley. Fast simulations of waves in three-dimensional excitable media. *Int. J. Bifurcat. Chaos*, 7:2529–2545, 1997.

[54] P. Moin. *Fundamentals of Engineering Numerical Analysis*. Cambridge University Press, 2nd edition, 2010.

[55] E.M. Purcell and D.J. Morin. *Electricity and Magnetism*. Cambridge University Press, 3rd edition, 2013.

[56] D. Jacqmin. Calculation of two-phase Navier-Stokes flows using phase-field modeling. *J. Comput. Phys.*, 155:96–127, 1999.

[57] C.C. Chang and C.Y. Wang. Starting electroosmotic flow in an annulus and in a rectangular channel. *Electrophoresis*, 29:2970–2979, 2008.

[58] H. Hecht and J. Harting. Implementation of on-site velocity boundary conditions for D3Q19 lattice Boltzmann simulations. *J. Stat. Mech.*, 2010:P01018, 2010.

[59] Laurier L. Schramm. *Emulsions, Foams, and Suspensions*. Wiley-VCH, 2005.

Concluding remarks and outlook

6.1 Concluding remarks

The simulations presented in this thesis have examined the behaviour of droplets in several configurations. The studies have presented valuable information about these systems as well as the nature of the methods used to model them.

Simulations of Janus droplets were performed using the Shan-Chen LBM. The ratios of the interfacial tensions between the three fluids determine the equilibrium geometry of two interacting droplets suspended in the third fluid. The steady-state geometries of simulations at conditions that lead to the three possible equilibrium configurations were consistent with an interfacial tension balance at the three-fluid contact point (if one is present). The behaviour of adhering droplets in confined shear flow depends on their geometry. When two nearly-circular lobes are present, the compound droplet oscillates in the shear gradient direction, while droplets with two semi-circular lobes do not oscillate. The rotation rates of both droplet types vary with the orientation of the droplets in the flow; droplets with semi-circular halves rotate slightly slower on average. The internal flow in Janus droplets with semi-circular halves was analyzed by subtracting the flow field due to rigid rotation, which revealed the presence of vortices in this flow relative to rigid rotation. The number of vortices that are present depends on the orientation of the internal interface, and the variation in rotation rate was related to the structure of these vortices.

A free-energy LBM was used to investigate the conditions for coalescence of a pair of droplets in shear. The high resolution of these simulations allowed the critical capillary numbers for coalescence to be determined, and the influence of several variables on the critical conditions was investigated. These simulations were sufficiently resolved that interfaces merge due to the dynamics of the phase field. The most important result is that the critical capillary number decreases as the ratio of the droplet radius and interface thickness increases. This is analogous to the effect of the ratio of the droplet size and critical film thickness in physical systems. Through this dependence of the critical capillary number on

the size of physical and simulated droplets, the effective physical size of simulated droplets may be estimated. The high critical capillary numbers of the droplets in the simulations indicate that their effective physical sizes are small. The effects of the phase field mobility, the initial separation between the droplets in the shear gradient direction, and the confinement of the droplets (ratio of the droplet radius and the gap between the shear planes) on the critical capillary numbers for coalescence as a function of the droplet size were also determined. High mobility (or a low Péclet number, the ratio of advection and diffusion rates) and small initial separation promote coalescence and increase the critical capillary numbers. The effect of confinement is more complex, and the differences between collisions with increasing droplet size (constant confinement) and increasing domain size (constant droplet size; decreasing confinement) were shown.

The simulations of droplet collisions in Chapter 4, with twice the maximum ratio of the droplet size and interface thickness in Chapter 3, revealed details about the behaviour of adjacent interfaces during a collision. A lower initial separation between the droplets was used in Chapter 4 than in Chapter 3 to approach the conditions of experimental studies of polymer droplet coalescence in confined shear. The minimum distance between the droplet interfaces as a function of time during collisions at several near-critical capillary numbers was computed. The presence of two places with minimum film thickness was found, causing the entrapment of a droplet of the external fluid during coalescence. From the minimum film thickness during collisions without coalescence, the critical film thickness for these phase field simulations was determined. In the simulations with coalescence, a minimum film thinning rate was observed. The orientation of the film at the times of minimum thickness, minimum thinning rate, and coalescence was examined, and the behaviour in the limit as the critical capillary number is approached from sub- and supercritical values was discussed. The physical size of the simulated droplets was estimated in two ways: the ratio of the droplet size and critical film thickness, and by extrapolation to small sizes of an experimental scaling law for the dependence of critical capillary numbers on droplet size. Both methods provided a radius on the order of 1 μm.

Unlike the comparatively simple ternary system in Chapter 2 and the binary liquid system studied in Chapters 3 and 4, real liquid mixtures exhibit many complex phenomena at interfaces. One phenomenon that occurs frequently and has therefore received much scientific attention is the presence of electric charge on interfaces. Chapter 5 presented a coupling of the free-energy binary-liquid LBM with a finite difference solver for the linearized Poisson-Boltzmann model of electrostatic potential in an electrolyte adjacent to a charged surface. A benchmark study of electroosmotic flow in a square channel was used to assess the accuracy of the coupled solver. Collisions of droplets with constant surface

potential were then simulated. The effects of the strength of electrostatic interactions due to the Debye length and surface potential on the critical capillary numbers for coalescence were studied. The small size of the simulated droplets led to weak effects of charge on the critical capillary numbers for parameters that are representative of physical systems.

6.2 Outlook

The simulations described in this thesis have examined several aspects of droplet behaviour with an emphasis on droplets in shear flow. Some extensions of the presented work are straightforward: for example, the effects of variations in density and viscosity between the fluid phases could be considered, as well as the size ratio of the droplets that adhere to form a Janus droplet or collide in shear flow. Different initial conditions could also be studied, as well as different flow configurations such as extensional flow[1] or pressure-driven flow in a channel[2] instead of simple shear. Modifications to the lattice Boltzmann methods that were used may be needed to ensure stability and low spurious currents under these conditions. For some cases, such as high density ratios, potentially suitable methods are currently described in the literature[3, 4]. With sufficient computing resources, systems with many drops and their collective behaviour could be studied. Many options for parameter studies and extended models exist, however the simulations raise several fundamental questions about the droplet interactions that have been considered and the limitations of simulations as a method for studying them. A few of these questions are now examined.

Some of the simulation results suggest directions for experimental investigations. For Janus droplets, observations of internal flow patterns would be valuable for validation of the simulations. Considering the complex rotational motion of Janus droplets in shear and the dependence of the motion on the geometry of the droplet, measurements of the rheology of Janus emulsions with different droplet geometries and droplet volume fractions could reveal interesting phenomena about the collective motion of many Janus droplets. While collisions of polymer droplets, in which van der Waals forces between droplets are the primary non-hydrodynamic forces, have been studied experimentally[5, 6], analogous experiments with aqueous systems (with or without significant interfacial charge) have not been reported but would be useful. Experimental confirmation of the behaviour of the film at near critical capillary numbers would be valuable to evaluate the phase field simulation method. However, simple optical methods cannot be used, and new experimental methods are needed to measure moving films that are thinner than the wavelengths of visible light. Furthermore, the precision with which the capillary number must be controlled to observe these effects is another obstacle to overcome.

Despite the significant computational resources that were used, the physical radii of the simulated droplets are small, on the order of one micron. Though micron-sized droplets occur in some applications[7, 8], experiments on droplet collisions and coalescence have been performed with ten to one hundred times larger drops[1, 5, 6]. Simulations appear capable of describing the coalescence of micron-sized droplets, but experimental results at this length scale are unavailable. To bridge the gap between the capabilities of experiments and resolved simulations, two options are possible: smaller experiments and larger simulations. The world's largest cluster with GPUs, currently the Titan cluster at Oak Ridge National Laboratory (USA), has 18688 GPUs, 292 times more than the 64 used for the largest simulations in this thesis. Given that the volume of the simulated domain scales with the cube of the droplet radius, the GPUs on the world's largest cluster only have sufficient memory to simulate droplets that are 6.6 times larger than those simulated with 64 GPUs. With the scaling used in this thesis, the number of time steps to simulate the same physical time is proportional to the square of the radius, making the expected runtime of such a simulation on the order of one year (assuming perfectly efficient parallelization). Unless significant advances in computing capabilities are achieved, resolved simulations of ten to hundred micron droplets require new simulation strategies, such as locally refined grids near interacting interfaces[9–11].

In general, the simulations of droplet collisions raise questions about what level of detail is needed in the modelling of interfacial interactions to obtain useful predictions about real systems. Is, for example, the phase field method with a simple polynomial double well potential adequate, or are more realistic free-energy functionals necessary to match physical systems? What are the impacts of different choices for the free-energy[12–14] on the disjoining pressure[15] and the dynamics of film thinning? To what extent can the free energy functional be modified[16–18] to account for various interfacial phenomena? Would molecular dynamics simulations (of coalescence[19], for example) be useful to couple with or guide the development of new simulation models? The computational demands of simulations that capture the physics of additional interfacial interactions, such as the details of surface reactions, ion motion, surfactant adsorption, and the forces between surfactant molecules, would be even more significant than the already high requirements of the simulations in this thesis. Perhaps multiscale models could be developed to capture subgrid scale effects in simulations that do not resolve films. The challenge here should not be underestimated: interfacial interactions exhibit a rich variety of phenomena and some are highly sensitive to small changes, for example in the amount of surfactant on interfaces. Further development of the capabilities of simulations would provide useful insights about multiphase flows such as the rheology of stable concentrated emulsions. The steps that re-

main to be taken to answer the questions raised and work towards this goal of simulating concentrated emulsions suggest many possibilities for future theoretical, experimental, and simulation studies of coupled fluid and interfacial dynamics.

References

[1] L.G Leal. Flow induced coalescence of drops in a viscous fluid. *Phys. Fluids*, 16: 1833–1851, 2004.

[2] N. Bremond, A.R. Thiam, and J. Bibette. Decompressing emulsion droplets favors coalescence. *Phys. Rev. Lett.*, 100:024501, 2008.

[3] T. Inamuro, T. Ogata, S. Tajima, and N Konishi. A lattice Boltzmann method for incompressible two-phase flows with large density differences. *J. Comput. Phys.*, 198:628–644, 2004.

[4] T. Lee and C.-L. Lin. A stable discretization of the lattice Boltzmann equation for simulation of incompressible two-phase flows at high density ratio. *J. Comput. Phys.*, 206:16–47, 2005.

[5] D. Chen, R. Cardinaels, and P. Moldenaers. Effect of confinement on droplet coalescence in shear flow. *Langmuir*, 25:12885–12893, 2009.

[6] P. De Bruyn, R. Cardinaels, and P. Moldenaers. The effect of geometrical confinement on coalescence efficiency of droplet pairs in shear flow. *J. Colloid Interf. Sci.*, 409: 183–192, 2013.

[7] C. D. McAuliffe. Oil-in-water emulsions and their flow properties in porous media. *J. Petrol. Technol.*, 24:727–733, 1973.

[8] U. Sundararaj and C.W. Macosko. Drop breakup and coalescence in polymer blends: The effects of concentration and compatibilization. *Macromolecules*, 28:2647–2657, 1995.

[9] O. Filippova and D. Hänel. Grid refinement for lattice-BGK models. *J. Comput. Phys.*, 147:219–228, 1998.

[10] J. Tölke, S. Freudiger, and M. Krafczyk. An adaptive scheme using hierarchical grids for lattice Boltzmann multi-phase flow simulations. *Comput. Fluids*, 35:820–830, 2006.

[11] H.D. Ceniceros, R.L. Nós, and A.M. Roma. Three-dimensional, fully adaptive simulations of phase-field fluid models. *J. Comp. Phys.*, 229:6135–6155, 2010.

[12] J.W. Cahn and J.E. Hilliard. Free energy of a nonuniform system. I. Interfacial free energy. *J. Chem. Phys.*, 28:258–267, 1958.

[13] M.R. Swift, S.E. Orlandini, W.R. Osborn, and J.M. Yeomans. Lattice Boltzmann simulations of liquid-gas and binary fluid systems. *Phys. Rev. E*, 54:5041–5052, 1996.

[14] P.G. de Gennes. Dynamics of fluctuations and spinodal decomposition in polymer blends. *J. Chem. Phys.*, 72:4756–4763, 1980.

[15] P. Yue, J.J. Feng, C. Liu, and J. Shen. Diffuse-interface simulations of drop coalescence and retraction in viscoelastic fluids. *J. Non-Newtonian Fluid Mech.*, 129: 163–176, 2005.

[16] R.G.M. van der Sman and S. van der Graaf. Diffuse interface model of surfactant adsorption onto flat and droplet interfaces. *Rheol. Acta*, 46:3–11, 2006.

[17] P. Yue, J.J. Feng, C. Liu, and J. Shen. A diffuse-interface method for simulating two-phase flows of complex fluids. *J. Fluid Mech.*, 515:293–317, 2004.

[18] H. Liu and Y. Zhang. Phase-field modeling droplet dynamics with soluble surfactants. *J. Comput. Phys.*, 229:9166–9187, 2010.

[19] L. Zhao and P. Choi. Molecular dynamics simulation of the coalescence of nanometer-sized water droplets in n-heptane. *J. Chem. Phys.*, 120:1935–1942, 2004.

Convergence of film thickness

In this appendix, we analyze the distance between colliding droplets at the conditions of the simulations in Chapter 3[1]. In these simulations, Re $= 1$, $\ell_\varphi = 2$, Ca $= 0.1$, $\Delta X/(2R) = 1.26$, $\Delta Y/2R = 0.86$, and $2R/H = 0.39$. The key difference in parameters between the results in this appendix and the higher-resolution results in Chapter 4 is the vertical offset $\Delta Y/(2R) = 0.86$. With this vertical offset the droplets do not coalesce with Ca $= 0.1$ for $R/\ell_\varphi \geq 18.75$. We consider two Péclet numbers, 10 and 50, to demonstrate the role of the mobility on the evolution of the minimum film thickness.
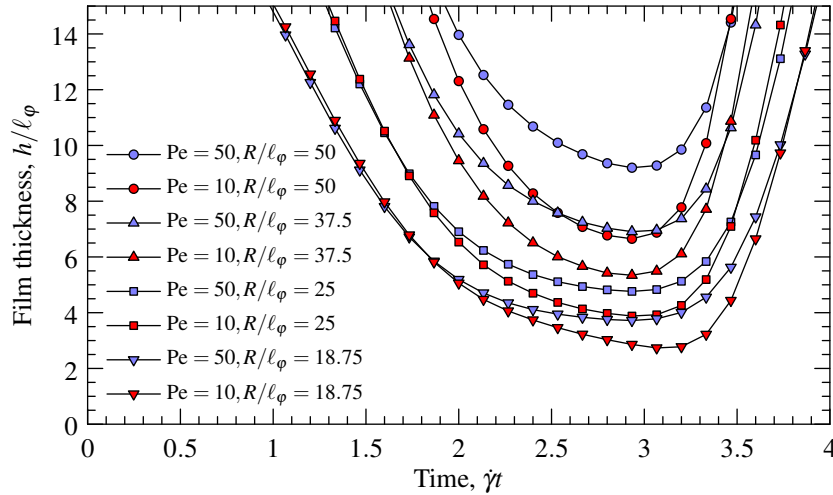

Figure A.1: Film thickness (normalized by interface thickness) as a function of time for several resolutions at non-coalescing conditions (Ca $= 0.1$, $\Delta Y/(2R) = 0.86$) and two Péclet numbers. For all cases, $\ell_\varphi = 2$.

Figures A.1 and A.2 show the minimum distance between the drops as a function time. Of all the cases, only the simulation with $R/\ell_\varphi = 18.75$ and Pe $= 10$ is near the critical conditions for coalescence(Chapter 3). In general, the critical Ca decreases with increasing R/ℓ_φ and Pe (increasing mobility M). The difference between the dynamics of h at near-critical conditions is highlighted in Fig. A.2, in which h/R evolves clearly differently from
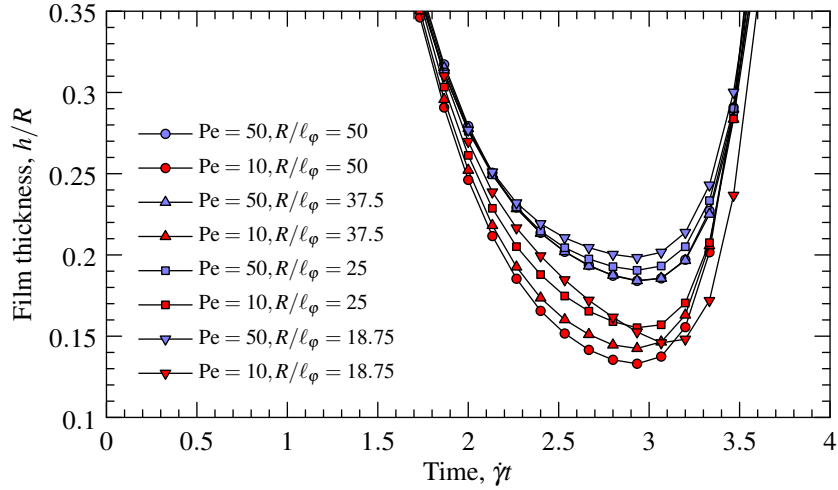
Figure A.2: Film thickness normalized by the droplet radius R at the same conditions as Fig. A.1.

the other cases. In this near-critical case, h has a longer period of thinning and a later minimum. In the other cases, convergence towards different limits is seen for the two Péclet numbers. With the higher mobility (lower Pe), the minimum thickness of the film is lower, consistent with the expectation that the late stages of thinning are determined by the mobility rather than fluid flow in the film. In Figure A.1 we see that the curves for the smallest radius cross at $\dot{\gamma}t = 1.7$ and $h/\ell_\varphi = 6$. Until this point, one may consider the interfaces to be non-interacting because the thickness of the film is independent of the mobility.

References

[1] O. Shardt, J.J. Derksen, and S.K. Mitra. Simulations of droplet coalescence in simple shear flow. *Langmuir*, 29:6201–6212, 2013.